Analyse des processus physiques régissant les évolutions récentes de la banquise Arctique

Sarah Gani

THÈSE DE DOCTORAT DE SORBONNE UNIVERSITE

Sciences de l'Environnement d'Ile de France

École doctorale 129

Réalisée au Laboratoire d'Océanographie et du Climat :

Expérimentations et Approches Numérique

Présentée par Sarah GANI

Analyse des processus physiques régissant les évolutions récentes de la banquise Arctique

Soutenance le 29/11/2021

Devant le jury composé de:

Mme Solène Turquety	LMD, SU, Paris	Présidente
M François Massonnet	ELIC, UCLouvain	Rapporteur
M Ghislain Picard	UGA, IGE, Grenoble	Rapporteur
Mme Sally Close	LOPS, UBO, Brest	Examinatrice
Mme Nathalie Sennéchael	LOCEAN, SU, Paris	Co-directrice
M Jérôme Sirven	LOCEAN, SU, Paris	Directeur

“ Tu vois, la mer monte, elle descend, qu’est ce qu’il y a de mieux ?
Et personne n’a de pouvoir sur elle. ”

Le père Jaouen

Remerciements

Merci, merci, merci, merci….

Je te remercie Jérôme. Pour la confiance que tu as su m'accorder, et ce, dès mon stage de fin d'études. Merci pour ta patience, ta pédagogie, ton élégante modestie, mais surtout ton incroyable gentillesse. J'ai énormément apprécié apprendre et découvrir ce monde fascinant qu'est l'Arctique et sa glace de mer. Enfin, j'espère de tout coeur que tu as bien fait de croire que "les fruits passeront la promesse des fleurs".

Merci Nathalie, pour toute l'aide que tu m'as apportée pendant cette thèse, le temps que tu m'as consacré et tes nombreux conseils.

Je tiens également à remercier les différents membres de mon Jury qui ont accepté d'évaluer ma thèse. Je remercie l'ensemble des personnes qui ont participé de près ou de loin à l'élaboration de cette thèse, par le biais de discussions stimulantes et bienveillantes.

De ces trois années, je retiendrai évidemment les nombreuses rencontres et les nouveaux et solides liens d'amitié. Merci aux filles du couloir pour les pauses déjeuner, les soirées jeux et votre soutien si important. Cécilia, on a commencé et terminé cette thèse ensemble et tu m'as été d'une grande aide, merci. Merci aux copains du labo, pour la rigolade, les vacances en Bretagne, les jeudis tant pis, les quais de seine, et tant d'autres. Sans vous, ma thèse n'aurait pas du tout eu la même saveur et ça aurait été bien dommage. Mention spéciale à Lucie, avec qui j'ai fait tant des kilomètres dans les rues de Paris…

Merci à la bande de Paris, pour tous ces moments de folie passés pendant ces trois années. Merci à la colove, de m'avoir hébergé à de nombreuses reprises. Ce sont tous ces moments à vos côtés qui m'ont permis de relâcher la pression, et de faire de ces années éprouvantes, des années fantastiques. Rendez-vous au prochain tour du cadran !

Merci également aux copains de Bretagne. Quand le manque de la mer et des dunes se faisait sentir, mes retours à Brest ont été d'indispensables bols d'air, et cela en grande partie grâce à vous. Et merci d'avoir toujours pris des nouvelles de l'avancée de ma " thèse sur les glaçons " !

Mes remerciements vont également à ma superbe famille. Mes parents Vévé et Nono, mes sœurs Marianne et Caroline, mon frère Mehdi, et ma grand-mère Gigi, qui m'encouragent et me font rire depuis toujours. Merci maman, ta douceur, ta positivité et tes conseils dans les moments où je ne pensais pas y arriver ont été essentiels.

Merci Amélie, a minha galinha. Pour tout ce que tu m'as apporté. Pour m'avoir soutenu et encouragé au jardin alpin et pour avoir été à mes côtés chacun des jours qui ont suivi.

Résumé

En Arctique, les conséquences du réchauffement climatique sont plus fortes que partout ailleurs sur le globe : ainsi, l'augmentation de la température de l'air depuis deux décennies y est plus de deux fois plus élevée que l'augmentation moyenne, selon le dernier rapport du GIEC. La banquise témoigne de ces changements de façon privilégiée. On observe une diminution importante de la couverture de glace de mer, associée à une perte de volume en toute saison. La glace de mer devient plus jeune, fragile et mobile. Cette évolution de la banquise a fait entrer l'Arctique dans un nouvel état où les interactions air/neige/glace/océan sont modifiées et difficiles à appréhender. Mieux comprendre et prévoir ces changements nécessite des observations et des modèles numériques performants pour simuler correctement les interactions entre la glace de mer et les autres composantes qui commandent le climat de l'Arctique.

Dans ce contexte de changement climatique, l'objectif de cette thèse est d'analyser des séries d'observations collectées principalement en hiver par des bouées dérivantes IAOOS -Ice Atmosphere Arctic Ocean Observing System- (équipées de SIMBAs -SAMS Ice Mass Balance for the Arctic-) pour comprendre quels processus déterminent l'évolution récente de la glace de mer en Arctique. En plus d'une analyse des observations "per se", des simulations numériques sont réalisées à partir du modèle unidimensionnel de glace et de neige LIM1D (Louvain-la-Neuve sea Ice Model).

La première étude porte sur l'analyse de deux séries de données collectées par des instruments SIMBA déployés en hiver au Nord du Svalbard pendant la campagne N-ICE2015. Cette analyse est associée à des simulations numériques, dont la qualité est évaluée en comparant les profils de température dans la neige et la glace observés et modélisés. Nous montrons qu'il est nécessaire de représenter le manteau neigeux par plusieurs couches (5 suffisaient dans ce cas) pour bien simuler les profils de température souvent non linéaires. Nous donnons une première estimation de la densité de la neige (240-390 kg/m^3), déduite des simulations optimales. Des études de sensibilité sont également menées afin d'estimer l'impact des forçages atmosphériques et océaniques sur le résultat des simulations

numériques. L'inondation de la neige et le processus de formation de glace de neige sont simulés et l'évolution de la salinité et de la fraction volumique des poches de saumure (grandeurs qui ne peuvent être mesurées en continu) est également calculée.

Dans une deuxième étude, quatre séries de données collectées pendant la campagne TransArc II sont analysées. Nous proposons une méthode permettant de déterminer la stratification de la neige, uniquement à partir des observations, ainsi que la conductivité et la densité de la neige dans les différentes couches qui ont été déterminées. Les simulations numériques réalisées avec le modèle LIM1D corroborent ces estimations de conductivité et de densité obtenues à partir des observations. Le déploiement des SIMBAs entraîne des perturbations du milieu (neige mouillée artificiellement introduite dans la zone de franc bord, trou de déploiement), que l'on peut étudier, et dont on a déterminé les caractéristiques et l'impact sur les mesures. En particulier, la cinétique de la prise en glace de l'eau de mer présente dans le trou de déploiement de l'instrument SIMBA a pu être complètement analysée. Une première estimation du flux latéral causé par cette perturbation dans la glace environnante a été calculée et sa contribution comparée à celle due aux flux verticaux.

Abstract

In the Arctic, the consequences of global warming are stronger than anywhere else on the planet : the increase in air temperature over the last two decades is more than twice the average increase, according to the latest IPCC report. The evolution of the ice pack is a prime example of these changes. We observe a significant decrease in sea ice cover, associated with a loss of volume in all seasons. The sea ice becomes younger, more breakable, and more mobile. These changes in sea ice have brought the Arctic into a new state where air/snow/ice/ocean interactions are altered and difficult to apprehend. More observations and efficient numerical models are required to better understand and predict these changes and to correctly simulate the interactions between sea ice and the other components that control the Arctic climate.

In this climate change context, the objective of this thesis is to analyze observations mainly collected in winter by IAOOS -Ice Atmosphere Arctic Ocean Observing System- drifting buoys (equipped with SIMBAs -SAMS Ice Mass Balance for the Arctic-), to understand which processes determine the recent Arctic sea ice evolution. We confront these analyses with numerical simulations made from the one-dimensional ice and snow model LIM1D (Louvain-la-Neuve sea Ice Model).

In a first study, we analyze two sets of data collected by SIMBA instruments deployed in the North of Svalbard during the N-ICE2015 campaign. By comparing the observed and modeled temperature profiles in snow and ice, we evaluate the quality of the simulations. We show that it is necessary to represent the snow cover by several layers (5 were sufficient in this case) to accurately simulate the often non-linear temperature profiles. We can present a first estimate of the snow density (240-390 kg/m^3) deduced from the optimal simulations. Sensitivity studies are also conducted to estimate the impact of atmospheric and oceanic forcings on the simulations. The snow flooding and snow-ice formation process is simulated and the evolution of salinity and brine volumic fraction (parameters that cannot be measured continuously) is computed.

In a second study, four sets of data collected during the TransArc II campaign are analyzed. We propose a method to determine the snow stratification from the observations alone, as well as the snow conductivity and density in the different layers that were determined. Numerical simulations performed with the LIM1D model corroborate these conductivity and density estimates obtained from observations. The deployment of SIMBAs leads to perturbations of the medium (wet snow artificially introduced in the freeboard zone, deployment hole), which can be studied, and whose characteristics are determined. In particular, the kinetics of the freezing of the seawater in the hole made during the deployment of the SIMBA instrument could be completely analyzed. A first estimate of the lateral flux caused by this disturbance in the surrounding ice has been made and its contribution compared to that due to vertical fluxes.

Table des matières

Introduction

L'Arctique compte parmi les régions les plus difficilement accessibles de la planète et de ce fait, parmi les plus fascinantes pour nombre d'exploratrices et d'explorateurs. La glace de mer a joué un rôle important, et souvent tragique, dans la conquête des régions polaires. Les récits de navigatrices et navigateurs tels que Roald Amundsen, Louise Boyd, Willem Barents, Vitus Bering, Ann Bancroft et bien d'autres continuent de susciter un vif intérêt plus d'un siècle après leurs explorations. En 1873, Nansen et son équipage quittent Bergen en Norvège, à bord du navire Fram, pour une expédition scientifique qui a pour objectif d'étudier l'Arctique en se faisant emprisonner par la glace de mer et en dérivant avec celle-ci, via le courant transpolaire. La communauté scientifique a ainsi pris conscience dès cette époque que l'étude des processus physiques et dynamiques de l'océan Arctique et de sa banquise permettrait de comprendre non seulement son évolution, mais aussi son rôle clé sur le climat passé et à venir de notre planète.

Septentrionalium Terrarum descriptio. Vision de l'Arctique par le mathématicien cartographe G. Mercator en 1595.

Sommaire

1. L'Arctique, une région en mutation

Le Groupe d'experts Intergouvernemental sur l'Evolution du Climat (GIEC) a publié le premier volet de son sixième rapport en Août 2021. Ce rapport présente de façon détaillée l'ensemble des connaissances scientifiques, techniques et socio-économiques acquises jusqu'à ce jour et portant sur les changements climatiques, leurs causes, ainsi que leurs répercussions potentielles.

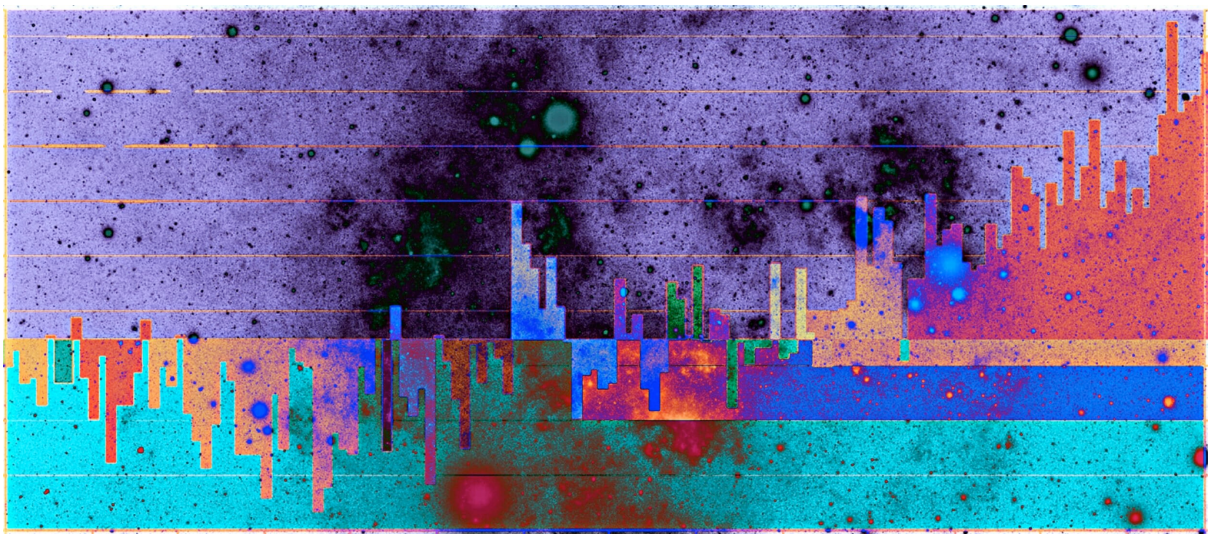

Figure 1. © 2021 ENVIRONMENTAL GRAPHITI. Global Temperatures 1880-2019. Alisa Singer

La température mondiale de surface est 1.09°C plus chaude sur la période 2011-2020 que sur la période 1850-1900, avec un réchauffement imputable en quasi totalité aux activités humaines (1.07°C) et notamment au rejet massif de gaz à effet de serre (Figure 1). Selon les modèles climatiques, la température moyenne à la surface du globe entre 2081 et 2100 sera

très probablement plus élevée de 1,0°C à 1,8°C que celle de la période 1850-1900 dans le scénario optimiste de très faible émissions de gaz à effet de serre (SSP1-1,9 pour *Shared Socioeconomic Pathways*), de 2,1°C à 3,5°C dans le scénario intermédiaire (SSP2-4,5) et de 3,3°C à 5,7°C dans le scénario le plus pessimiste (SSP5-8,5).

En région Arctique, l'augmentation de la température de l'air est plus de deux fois plus élevée que l'augmentation moyenne au cours des deux dernières décennies (*Notz et Stroeve, 2016 ; Richter-Menge et al., 2017*) : on parle d'amplification polaire (Figure 2). Ce phénomène est dû à plusieurs boucles de rétroactions positives (*Hall, 2004; Pithan et Mauritsen, 2014; Stuecker et al., 2018*).

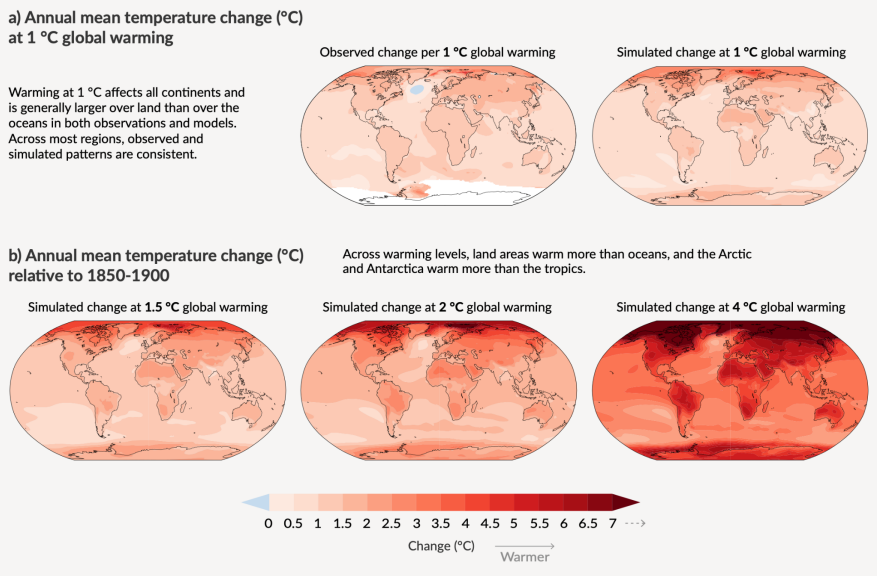

Figure 2. (a) Comparaison de la variation de la température moyenne annuelle de surface observée et simulée (°C). (b) Variation de la température moyenne annuelle de surface simulée (°C). *(IPCC, 2021)*

La boucle principale de rétroaction est associée à la diminution générale de l'albédo (rapport entre le rayonnement solaire réfléchi et le rayonnement incident par unité de surface). La terre reçoit l'énergie solaire sous forme de rayonnement électromagnétique de relativement courte longueur d'onde (UV, visible et proche infrarouge). En atteignant la surface terrestre, le rayonnement solaire incident est absorbé et réfléchi en fonction du terrain qu'il rencontre. Dotée d'un albédo élevé (~0.5-0.7) comparé à l'océan (~0.06), la

banquise arctique réfléchit une large part du rayonnement solaire incident. Même une fine couche de glace suffit à limiter l'absorption du rayonnement par l'océan. Si une couche de neige (dont l'albédo peut dépasser 0.9) est présente en surface, ce phénomène est encore accentué. Lorsque la glace fond, la quantité de rayonnement solaire réfléchi vers l'atmosphère est réduite, la proportion de chaleur absorbée par l'océan augmente, ce qui accentue davantage la fonte de banquise.

Notons de plus que la glace de mer est partiellement recouverte en été par des mares ou des lacs de fonte (*melt ponds,* Figure 4), c'est-à-dire par de la neige (ou de la glace) qui fond en surface et forme des mares ou des lacs. Ces mares de fonte possèdent un albédo d'environ 0.15-0.6 (*Skyllingstad et al., 2009*) et diminuent d'autant l'albédo de la banquise qu'elles sont plus nombreuses (*Perovich et al, 2003*).

On observe que l'étendue de la glace de mer Arctique diminue depuis au moins quatre décennies, quel que soit le mois de l'année. Entre les périodes 1979-1988 et 2010-2019, l'étendue totale de la glace de mer arctique a diminué de 40% en fin d'été, soit environ 14 % tous les 10 ans (*Meredith et al., 2019*). La diminution de la superficie de la glace de mer arctique est la plus forte en septembre (- 12,8 ± 2,3 % par décennie ; 1979-2018) et est sans précédent depuis au moins 1000 ans (Kinnard et al., 2011). Il est de plus extrêmement probable que le réchauffement prévu de l'Arctique entraîne une réduction continue de la masse des glaciers et de la neige sur les terres (*IPCC, 2021*).

Outre la réduction de son étendue, la banquise Arctique s'amincit et passe progressivement d'un régime pluriannuel à un régime annuel (*Comiso, 2012; Kwok and Rothrock, 2009; Maslanik et al., 2011*). La glace de mer est qualifiée de *annuelle* si elle est âgée de moins d'une année et *pluriannuelle* si elle résiste plusieurs années à la période de fonte. En mars 1985, la glace de mer qui avait survécu à au moins quatre étés représentait 33% de la banquise Arctique au maximum de l'hiver. En mars 2019, cette glace ne représentait plus qu'un peu plus de 1% (*Tschudi et al. 2019a,b*). D'après des études fondées sur des sorties de

modèles, l'Arctique pourrait se retrouver libre de glace de mer en été, et cela avant 2050 (*Boé et al., 2009; Stroeve et al., 2012; Massonnet et al., 2018; Notz et al., 2020; Bonan et al., 2021*). L'océan Arctique se retrouverait alors sans glace à la fin de l'été, puis gèlerait à nouveau l'hiver suivant.

Sous la banquise, l'océan Arctique présente une couche d'eau froide peu salée sur quelques dizaines de mètres de profondeur (ruissellement d'eaux douces d'origine continentale, grands fleuves, précipitations). Cette couche d'eau peu salée se trouve au-dessus d'eaux atlantiques ou pacifiques plus salées et plus chaudes. La croissance et la fonte de la banquise Arctique influencent l'état de la couche superficielle de l'océan. La formation de glace de mer s'accompagne d'un rejet massif de sel qui rend plus dense l'eau située juste sous la glace (voir section 2.2). À l'inverse, la fonte de la glace de mer provoque un flux d'eau douce qui diminue la densité de la couche supérieure de l'océan.

Les changements induits par le climat sur l'étendue et l'épaisseur saisonnières de la glace de mer modifient également la production primaire marine et donc les écosystèmes marins (*Lebrun., 2019*). On sait depuis plus de 150 ans que la glace constitue un habitat pour une grande variété d'organismes jouant un rôle important dans la chaîne alimentaire. Par exemple, la croissance du phytoplancton est largement influencée par la glace de mer (*Wassmann et Reigstad, 2011*). En effet, cette dernière régule la quantité de lumière disponible ainsi que le taux de nutriments dont le phytoplancton a besoin pour se développer.

Le climat terrestre est donc gouverné par une multitude d'interactions qui interviennent entre les différentes composantes du système climatique que sont l'atmosphère, l'hydrosphère, la cryosphère, la biosphère et la lithosphère. À l'avenir, l'Arctique devrait être profondément différent et le degré et la nature de cette transition dépendent fortement du rythme et de l'ampleur du changement climatique mondial. La glace de mer

joue un rôle climatique certain du fait des nombreuses rétroactions qu'elle induit à l'interface océan/atmosphère.

2. La glace de mer

2.1 Le cycle saisonnier de la banquise

L'étendue et l'épaisseur de la banquise sont gouvernées au premier ordre par la variabilité saisonnière de l'insolation solaire. Dans les hautes latitudes, cette variabilité est forte car l'inclinaison de la surface de la terre par rapport aux rayons solaires est importante. En hiver, la nuit polaire prive l'Arctique de tout rayonnement (entre 2 à 6 mois selon la latitude) tandis qu'en été, l'exposition aux rayons du soleil devient permanente.

En hiver, lorsque le rayonnement solaire est nul, l'étendue maximale de la banquise Arctique (la surface de l'océan couvert par au moins 15% de glace de mer) est atteinte en Mars (~14 millions de km^2). La banquise atteint son étendue minimum d'environ 6 millions de km^2 en Septembre (*Massonnet et al.*, 2018, Figure 3).

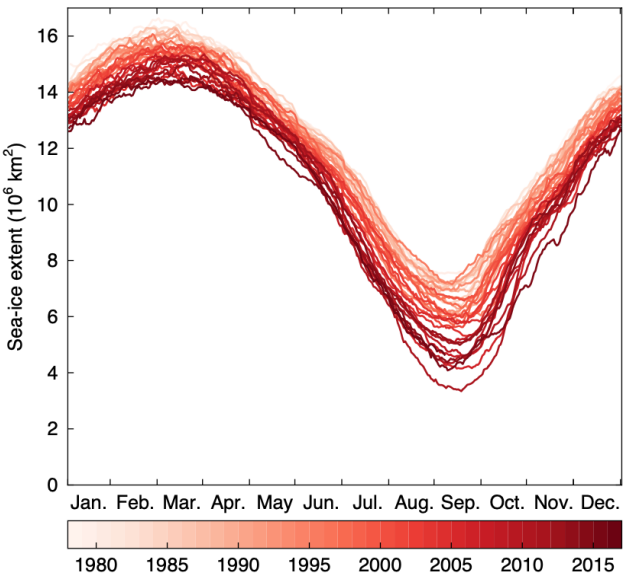

Figure 3. Cycle saisonnier de l'étendue de glace de mer Arctique (en million de km^2) en fonction de l'année (entre 1979 et 2017). (Par *Massonnet et al., 2018*).

2.2 Physique de la formation de la glace de mer

La glace de mer se forme dans les eaux libres au début de l'automne, par congélation de l'eau de mer en surface. Les mécanismes de formation de la glace de mer et ses propriétés sont très différents de ceux de la glace formée à partir d'eau pure en raison de la présence du sel. L'eau douce gèle à 0 °C, mais le point de congélation de l'eau de mer varie selon sa salinité. Pour chaque augmentation de 5 psu de la salinité, le point de congélation diminue de 0.27 °C. Ainsi, dans les régions polaires où la salinité de l'océan est d'environ 32 psu, l'eau commence à geler à -1.8°C. Des cristaux de glace (*le frasil*) se forment à la surface de l'eau, puis sous l'effet du vent et des vagues, vont se regrouper pour former des crêpes de glace (*pancake ice).* L'eau présente entre ces crêpes de glace va progressivement geler pour former une surface de glace plus ou moins homogène qui va s'épaissir par accrétion basale (Figure 4).

Figure 4. Morphologies diverses de la banquise (de gauche à droite et de haut en bas) : frasil (*frazil*), crêpes (*pancakes*), plaques (*floes*), mares de fonte (*melt pond*), fractures (*leads*), crête de compressions (http ://www.usna.edu)

La croissance de glace se fait à l'interface eau/glace et est conditionnée par les flux de chaleur océaniques et les pertes de chaleur vers l'atmosphère froide (*Nakawo and Sinha, 1977; Leppäranta, 1993*). Tant que la température de l'air reste inférieure à la température du point de congélation de l'eau de mer, il existe un flux de chaleur ascendant, de la glace vers l'atmosphère. Si ce flux de chaleur est supérieur à celui fourni par l'océan, le déséquilibre est compensé par la libération de chaleur latente, ce qui entraîne une augmentation de l'épaisseur de la glace.

La croissance de la glace de mer s'accompagne d'un rejet massif de sel dans l'eau de mer en surface. Lors de la formation de la glace, le sel qui n'a pas été rejeté se retrouve dans des inclusions d'eau liquide, appelées *poches de saumure,* dont la salinité peut être très élevée (≈40 à 200 psu, *Cox and Weeks., 1983*). Ces dernières sont en équilibre thermodynamique avec la glace qui les entoure et leur température est égale à la température de solidification du liquide. On rappelle que pour les liquides purs (par exemple l'eau pure), la température de solidification est constante à pression constante. Pour les solutions (qui contiennent un solvant et des ions de nature chimique différente dissous), la température de solidification (*liquidus temperature*) varie en fonction de la concentration en ions dissous à pression constante. Ici, plus la salinité des poches de saumure est élevée, plus la température à laquelle une phase solide peut se former est basse. Si la température locale change, l'équilibre des phases est maintenu par un changement de la salinité des poches de saumure. Par exemple, lorsque la température locale diminue, une partie de l'eau des poches de saumure va geler pour former de la glace quasi pure, ce qui va augmenter la salinité dans le fluide restant et rétablir l'équilibre des phases à la nouvelle température.

Il ne faut pas confondre la salinité des poches de saumure et la salinité moyenne de la glace (*bulk salinity*), qui dépend de la fraction volumique des poches de saumure et de leur salinité. La salinité moyenne de la glace diminue via des mécanismes de drainage du sel par gravité (*gravity drainage*), à travers les canaux qui relient les poches de saumure, ou bien par l'infiltration d'eau douce en été, provoqué par la fonte de la neige en surface (*flushing*).

L'impact de deux autres mécanismes de désalinisation (diffusion et expulsion) a également fait l'objet d'études (e.g. *Notz and Worster., 2009*) mais semble moins important. La glace de mer n'est donc pas un bloc rigide et imperméable, mais un milieu poreux (Figure 5). La coexistence liquide/solide accroît la complexité des propriétés thermodynamiques, optiques et mécaniques de la glace de mer, qui dépendent toutes de la fraction volumique des poches de saumure.

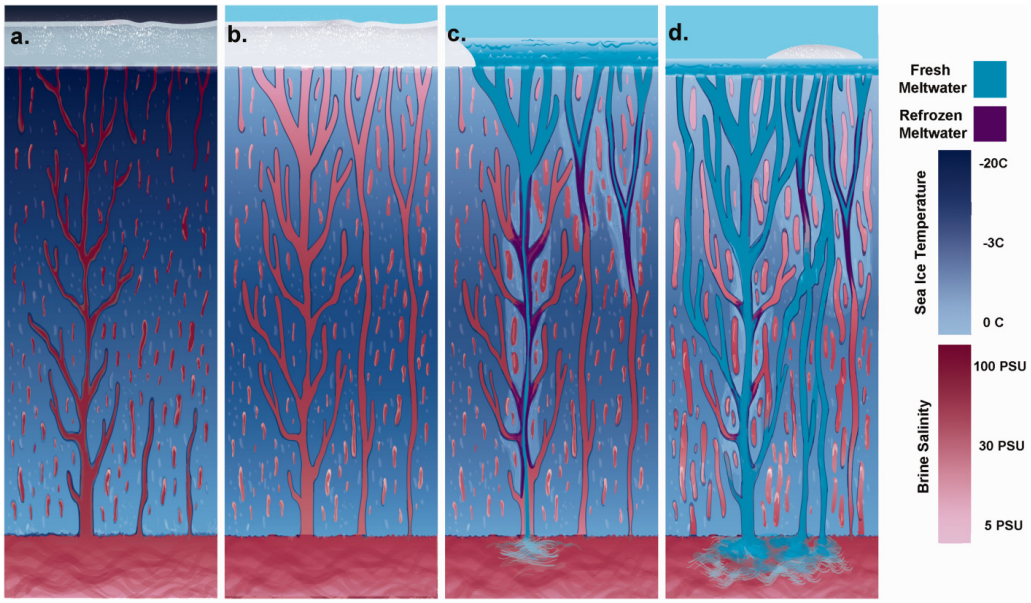

Figure 5. Illustration schématique du processus de percolation de l'eau dans la glace de mer hivernale via l'interconnexion des poches de saumure. Cette arborescence des canaux participe à la désalinisation de la glace de mer (De *Polashenski et al., 2017*).

2.3 Processus mécaniques dans la glace de mer

La morphologie de la glace de mer peut être très variée; lorsqu'elle est attachée au littoral, elle est plutôt homogène et lisse. En revanche, des plaques de glace (*floes*) de plusieurs kilomètres peuvent se déplacer et entrer en contact, formant ainsi des crêtes de compression (Figure 4). L'épaisseur de la banquise pluriannuelle peut dépasser 4 m et est souvent constituée d'un empilement de plaques de glace de mer provoqué par des mouvements de convergence. Une telle épaisseur est obtenue via des processus mécaniques et non thermodynamiques.

Lorsqu'une plaque de glace se brise, elle forme deux morceaux pouvant s'éloigner l'un de l'autre (Figure 4). L'espace entre les plaques s'appelle une fracture (*lead*). Les fractures jouent un rôle important dans le bilan thermique de l'Arctique en modifiant les échanges de chaleur entre l'océan et l'atmosphère. L'ensemble des plaques de glace dérivent sous l'action des courants océaniques et des vents.

3. Le manteau neigeux

La neige est un matériau poreux formé dans l'atmosphère et constitué d'air et de cristaux de glace (*Libbrecht, 2005*). L'agglomération des cristaux forme des flocons de neige qui précipitent au sol s'ils sont suffisamment lourds pour contrer les courants ascendants. Le diamètre des cristaux de glace varie de 0.1 à 2 mm environ (*Dominé et al., 2008*). Si la température au sol est inférieure à 0°C, les flocons s'accumulent et forment le manteau neigeux.

3.1 Le métamorphisme de la neige

Une fois déposés sur la glace de mer, la structure et l'organisation des cristaux de neige changent : c'est le métamorphisme de la neige (*Colbeck, 1982*). Cela affecte non seulement la cohésion (adhésion des cristaux de neige entre eux) du manteau neigeux (*Gallée et al., 2001*) mais aussi les propriétés physiques de la neige telles que la densité, la conductivité thermique (*Sturm et al., 1997*) ou l'albédo. Le métamorphisme dépend des conditions météorologiques telles que le vent, les précipitations et la température de l'air (*Colbeck, 1973, 1983; Merkouriadi et al., 2017b, Bokhorst et al., 2016 ; Dominé et al., 2016; Lecomte et al., 2011; Dominé et al., 2012; Gallet et al., 2017; Verin et al., 2019*). Il affecte la neige de manière différente selon la profondeur, son contact avec l'air ou avec la glace de mer. Le manteau neigeux - pouvant atteindre jusqu'à 1 m d'épaisseur (*Nicolaus et al., 2021*) - présente donc une forte hétérogénéité verticale.

3.2 La masse volumique

Différents paramètres physiques de la neige déterminent ses propriétés. La masse volumique de la neige sèche (notée ρ_s et exprimée en kg/m^3 dans ce manuscrit) représente la masse de cristaux de glace (et d'air emprisonné) par unité de volume de neige. Sa valeur dépend des conditions atmosphériques telles que la vitesse du vent, la température de l'air et l'humidité (*Pahaut, 1976; Liston et al., 2007*). Une température et un taux d'humidité élevé auront tendance à densifier la couche de neige (*Albert et al., 2004*). En moyenne, la masse volumique de la neige Arctique peut varier de 100 kg/m^3 si c'est de la neige fraîche et froide, à 600 kg/m^3 si c'est de la neige tassée, compactée par le vent, et/ou humide (*Dominé et al., 2008*). La mesure de la densité de la neige ne peut pas se faire par télédétection et sa mesure *in situ* comporte des incertitudes (~10%, *Conger and McClung, 2009*).

3.3 La conductivité thermique

La neige est un isolant thermique très efficace car elle est en partie constituée d'air. Plus la proportion d'air est importante, plus la densité est faible et plus la couche de neige est isolante. La conductivité thermique de la neige - qui est définie comme la capacité d'un matériau à conduire la chaleur - est donc très corrélée à sa densité (*Brandt and Warren, 1993*). Une densité élevée de la neige va donc être associée à une plus grande conductivité thermique (*Dominé et al., 2011*) puisque la conductivité de la glace est bien supérieure à celle de l'air (respectivement ~2.01 $W/m\ /K$ et ~ 0.02 $W/m\ /K$). Il existe de multiples relations (Figure 6) entre la densité de la neige et sa conductivité (e.g *Yen 1981; Sturm et al., 1997; Lecomte et al., 2013; Pertermann et al., 2017*), ce qui témoigne des larges incertitudes qui existent lors de la mesure de ces grandeurs.

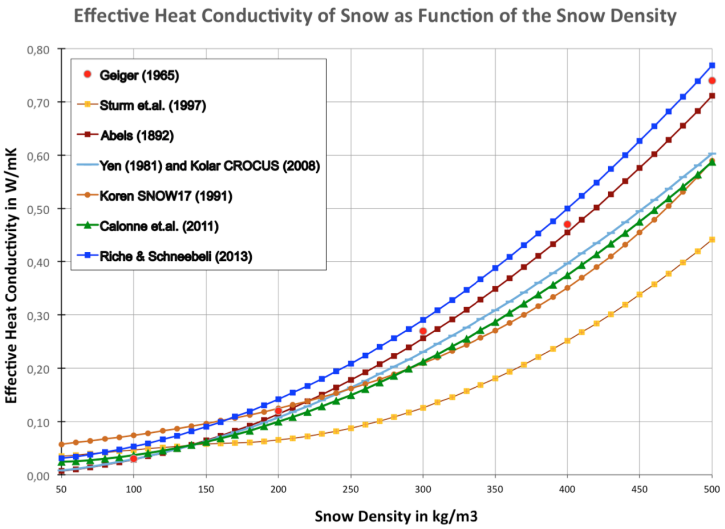

Figure 6. Comparaison de différentes formules pour la conductivité thermique équivalente de la neige. De *Pertermann et al., 2017*.

La couche de neige limite fortement le transfert de chaleur de la glace vers l'atmosphère et donc indirectement de l'océan vers l'atmosphère. En contrôlant le transfert de chaleur dans le manteau neigeux, la conductivité thermique de la neige joue un rôle prépondérant dans le bilan énergétique (*Riche and Schneebeli, 2013*).

Notons enfin que les échanges de chaleur dans le manteau neigeux se font par conduction dans les phases solide et gazeuse mais aussi par convection de la vapeur d'eau (*Yen, 1981; Colbeck, 1993*).

3.4 L'albédo

La neige a un pouvoir réfléchissant très important, avec un albédo bien supérieur à celui de l'océan et de la glace (~0.8). En réfléchissant une grande partie du rayonnement solaire entrant (*Perovich et al, 2002 ; Warren, 1982*), la couche de neige affecte l'évolution de la glace de mer par des processus qui peuvent être qualifiés de concurrentiels : au printemps et en été, l'albédo élevé de la couche de neige protège la surface de la glace de mer du rayonnement solaire (*Leu et al, 2010*) et retarde le début de sa fonte (*Petrich et al, 2012*). En automne et en hiver, le manteau neigeux de faible densité et d'albédo élevé joue un rôle

d'isolant et réduit la perte de chaleur de la glace vers l'atmosphère, ce qui ralentit la croissance de la glace de mer (*Perovich, 2003 ; Sturm et al., 2002a ; Sturm et al., 2002 ; Maykut et Untersteiner, 1971*).

Étant donné que la couche de neige régule la transmission de lumière à travers la glace, elle a également un impact sur la floraison des micro-algues au printemps, sous la banquise. Il a été démontré que l'épaisseur de neige présente en surface contribue à la répartition de la biomasse sous la glace (*Perovich et al., 1993; Mundy et al., 2005*).

4. Objet de la thèse et plan du manuscrit

L'évolution de la banquise Arctique témoigne du changement climatique global. On observe actuellement un régime nouveau, dont le fonctionnement précis nous échappe encore (*Vihma et al., 2014*). Les interfaces air/neige/glace/océan sont le lieu de multiples interactions physiques, chimiques et biologiques souvent difficiles à quantifier. L'étude de la glace de mer et du manteau neigeux est primordiale pour une compréhension globale du bilan énergétique en Arctique. Améliorer sa représentation dans les modèles permettrait de mieux comprendre l'évolution de l'Arctique et le rôle qu'il joue dans les rétroactions climatiques.

L'objectif de cette thèse s'inscrit dans ces problématiques. Nous avons étudié les processus thermodynamiques dans la neige et la glace de mer et les paramètres qui leur sont associés grâce à des observations in situ et des simulations numériques.

Le travail présenté dans ce mémoire a été réalisé en s'appuyant sur un ensemble de données obtenues à partir de plateformes instrumentées dérivant avec la banquise Arctique, et sur des simulations numériques effectuées avec un modèle de glace et de neige unidimensionnel (le modèle LIM1D, *Vancoppenolle et al.*, 2010) : ces deux points sont développés dans le chapitre 2.

Le chapitre 3 est un article publié dans *Journal of Geophysical Research e*n Décembre 2019 : Revisiting Winter Arctic Ice Mass Balance Observations With a 1-D Model: Sensitivity Studies, Snow Density Estimation, Flooding, and Snow Ice Formation.

Les chapitres 4 et 5 sont deux articles en voie d'être soumis conjointement à *Journal of Geophysical Research* : Estimating snow stratification, snow density, and sea ice lateral heat flux from temperature profiles provided by ice mass balance instruments. Part I : Analysis of Arctic observations. Part II : Numerical modeling assessment.

Observations et modélisation de la banquise Arctique

Sommaire

1. Les observations satellitaires et in situ

L'intérêt porté à la banquise Arctique n'a cessé de croître ces dernières décennies. Pour décrire les caractéristiques de la glace de mer et de la neige, comprendre leur évolution et leur impact futur sur le climat global et les écosystèmes, il est indispensable d'avoir des données fiables et de les étudier en détail.

Jusqu'aux années 1980, la seule façon d'étudier la banquise était de se rendre en Arctique et de réaliser des mesures in situ. Les déplacements sur la glace étaient longs, dangereux, et coûteux. De ce fait, les données avant ces années sont peu nombreuses. A partir de 1979, l'observation continue de l'Arctique par satellite devient possible.

1.1 Observations satellitaires

Depuis 1979, l'étendue de la glace de mer peut être déterminée (avec une précision de l'ordre de 10 km) à l'aide des satellites : les mesures de la concentration de glace de mer (la fraction locale de l'océan couverte de glace) sont déduites des observations du rayonnement micro-onde thermique émis par la surface de la Terre. L'étendue est habituellement définie comme la superficie de banquise couverte par au moins 15 % de glace (Figure 1).

Ces observations sont effectuées régulièrement, avec une couverture quasi complète de l'Arctique à l'échelle journalière. En été, les incertitudes liées à la mesure de la

concentration sont plus importantes en raison de la présence de mares de fonte, difficiles à distinguer de l'eau libre.

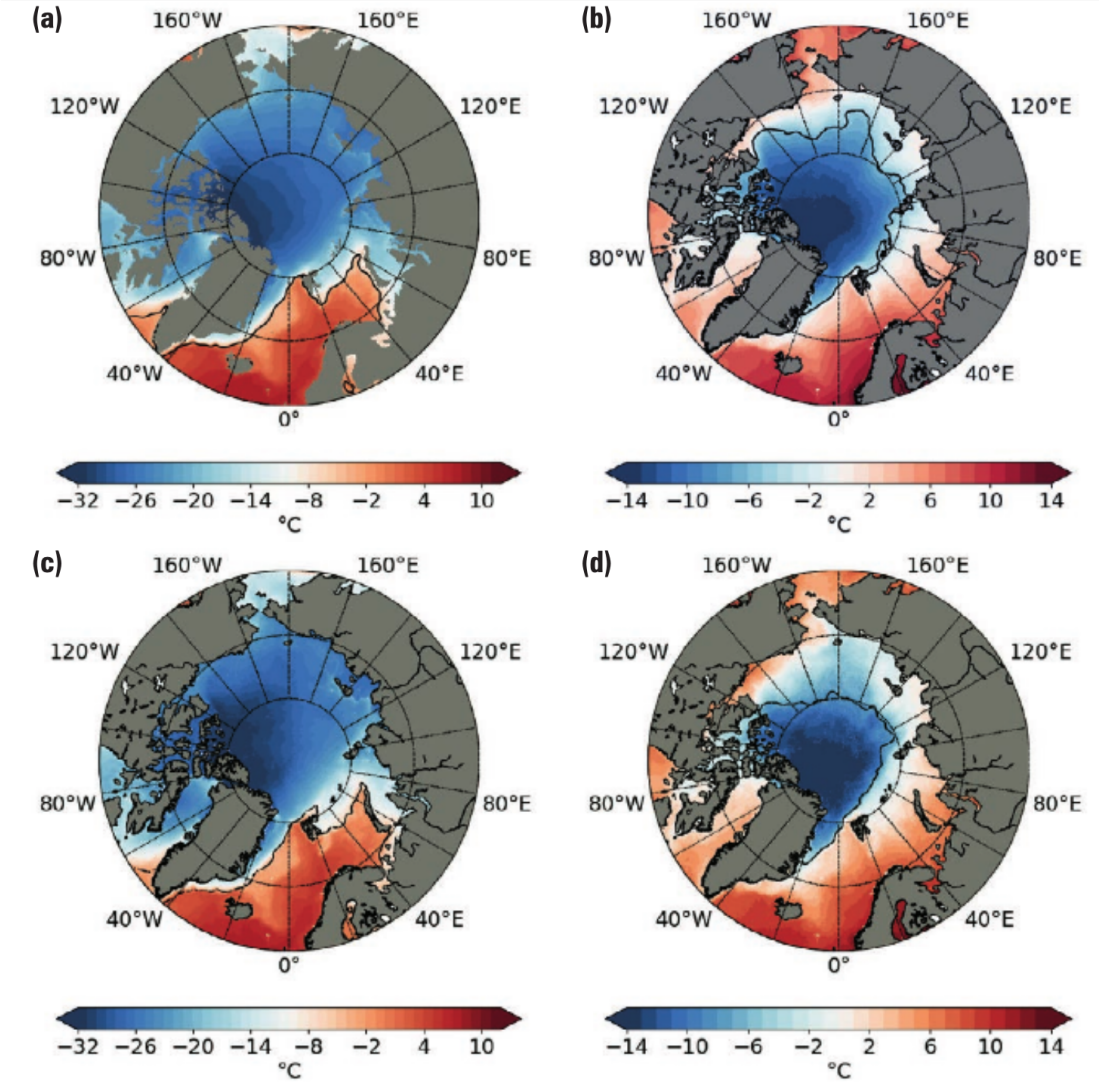

Figure 1. Température (°C) de surface observée en hiver (à gauche) et en été (à droite) par satellite, en moyenne pour les années 2007-2014 (en haut) et pour l'année 2012 (en bas), année durant laquelle l'étendue de glace en été a été la plus petite jamais mesurée (environ 4,1 millions de km^2). La ligne noire indique la limite entre l'océan libre de glace et la banquise, en définissant la banquise comme la surface couverte par au moins 15 % de glace. Source : EU Copernicus Marine Service Information. De *Msadek et al., 2020*.

L'épaisseur de la glace de mer peut également être déduite des observations satellitaires (altimétrie laser et radar). En appliquant l'équation d'équilibre hydrostatique, l'épaisseur de la banquise résulte de la valeur du franc bord (partie émergée de la banquise) et, si elle est présente, de l'épaisseur de la neige, mesurées par altimétrie (par exemple ERS-2, Envisat,

CryoSat-2, IceSat-2). Comme pour l'étendue de glace, ces mesures comportent des incertitudes, notamment en été lorsque la neige crée des mares ou lacs de fonte (*Msadek et al., 2020, Zygmuntowska et al., 2014*).

La neige biaise également la mesure de l'épaisseur de la glace de mer en compliquant l'estimation de la valeur du franc bord. Le manque d'information sur la densité de la couverture neigeuse augmente également les incertitudes lors du calcul de l'épaisseur de glace.

1.2 Observations in situ

Si l'imagerie satellitaire peut fournir des données très complètes en termes de couverture géographique, les données in situ restent indispensables. Les camps de terrain, les bouées dérivantes et les stations météorologiques automatisées produisent des données à des échelles et résolutions temporelles plus fines que les satellites. Ces observations permettent d'étudier des processus thermodynamiques mettant en jeu la glace de mer, la neige, l'atmosphère et l'océan. Elles sont également utilisées pour valider ou vérifier la précision des produits des satellites et des modèles.

Figure 2. Gauche/droite : le Tara/Polarstern pris dans la glace de mer Arctique lors de la campagne Tara/MOSAiC, © Francis Latreille, Fondation Tara /© Stefan Hendricks, Alfred Wegner Institute.

Au milieu des années 1970, le Arctic Ice Dynamics Joint Experiment (AIDJEX) a permis de faire progresser considérablement notre compréhension de la dynamique et de la rhéologie de la glace de mer grâce à des observations collectées pendant plus d'une année depuis quatre camps de glace habités. Une vingtaine d'années plus tard, le programme SHEBA (Surface Heat Budget of the Arctic Ocean, 1997-1998 ; *Perovich et al. 1999 ; Uttal et al. 2003*) s'est davantage concentré sur la thermodynamique de la glace de mer. Le bilan thermique de surface de la glace de mer a été étudié ainsi que les rétroactions glace-albédo pendant les saisons du printemps et de l'été.

Plus récemment, de nombreuses études ont été menées dans l'océan Arctique, en particulier pendant l'Année Polaire Internationale (API) 2007-2008. Sur les traces du Fram et plus de 100 ans après l'expédition menée par Nansen, la goélette Tara s'est laissée emprisonner dans la glace de mer et a dérivé avec le courant transpolaire Arctique pendant plus d'un an et demi, entre 2006 et 2008 (Figures 2, 3). La mission des vingts marins et scientifiques à son bord était d'étudier l'état de la glace, mais aussi celui de l'océan et de l'atmosphère aux abords du pôle Nord, ainsi que d'alerter l'opinion publique sur la fonte des glaces et le réchauffement climatique. Des projets tels que DAMOCLES (Developing Arctic Modeling and Observing Capabilities for Long-term Environmental Studies), ACCESS (Arctic Climate Change Economy and Society), ou INTAROS (Integrated Arctic Observation System) ont également combiné des études sur le terrain, des systèmes de surveillance intégrés et de la modélisation numérique afin d'examiner les conditions actuelles et futures de la couverture de glace Arctique.

Figure 3. Trajectoire du Tara et du Fram lors de leur dérive Arctique. Fondation Tara.

L'une des stations de dérive les plus récentes a eu lieu dans le cadre du projet norvégien N-ICE2015, qui comprenait quatre dérives distinctes au nord de Svalbard sur une période de six mois à bord du RV Lance (*Granskog et al. 2015*). Ce projet ciblait la nouvelle glace mince et les processus thermodynamiques et dynamiques associés.

Plus récemment, en septembre 2019, l'expédition Multidisciplinary drifting Observatory for the Study of Arctic Climate (MOSAiC) a envoyé le brise-glace de recherche allemand Polarstern dans l'Arctique pour passer une année piégé dans la glace de mer. Impliquant des centaines de chercheurs de 20 nations, MOSAiC visait à mieux comprendre les processus gouvernant l'évolution de la glace de mer et plus généralement celle du système climatique arctique.

Le programme IAPB (International Arctic Buoy Program), qui a pour objectif de maintenir un réseau de bouées dérivantes dans l'océan Arctique, permet de mieux comprendre le mouvement de la glace de mer et les processus physiques ayant lieu aux interfaces des différents milieux. Depuis 2012, dans le cadre du projet EquipEx IAOOS (pour "Ice, Atmosphere, Arctic Ocean Observing System"), des plateformes instrumentées ont été régulièrement déployées sur la banquise Arctique afin de développer et maintenir un réseau d'observation du système océan-glace-atmosphère (Figure 4). Ce réseau rend possible la surveillance et l'étude des processus couplés dans l'Océan Arctique.

1.3 SAMS Ice Mass Balance for the Arctic (SIMBA)

Les plateformes IAOOS dérivent avec la banquise et fonctionnent de façon autonome. Elles transmettent par satellite quasiment en temps réel des informations sur l'état de l'océan, de la glace de mer et de la basse atmosphère. Chaque plateforme est constituée d'un système de flottaison (la bouée proprement dite), de plusieurs instruments scientifiques intégrés et d'un cerveau central permettant de transmettre les données par iridum (Figure 4). Un micro Lidar (CIMEL), et une station météo fournissent des informations sur les conditions atmosphériques (pression, température de l'air,...). Dans l'océan, un profileur automatique mesure des profils verticaux de température, de salinité et de concentration en oxygène dissous jusqu'à 800 m de profondeur.

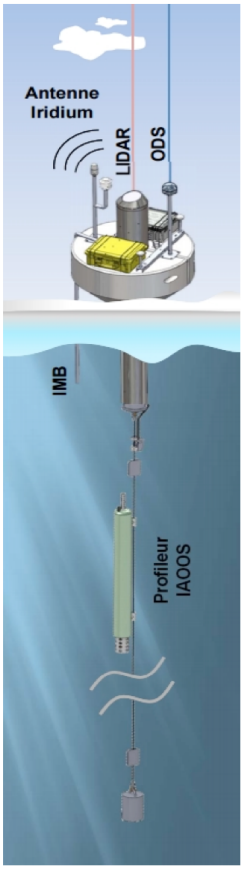

Figure 4. Schéma de la bouée IAOOS

Chaque plateforme accueille une SIMBA (SAMS Ice Mass Balance), instrument autonome en énergie et en transmission iridium, développé au SAMS (Scottish Association for Marine Sciences). Des données SIMBA ont été utilisées pour ce travail. L'instrument est constitué d'une chaîne de 5 m de long qui est déployée verticalement, si bien qu'elle traverse l'atmosphère, la neige, la glace et l'eau (Figure 5). Des thermistances fixées tous les 2 cm sur cette chaîne mesurent la température avec une précision de 0,1 °C (*Jackson et al., 2013*) dans chacun des milieux. Des résistances situées en regard des thermistances permettent de chauffer le milieu environnant ; des mesures de température réalisées pendant la phase de chauffe permettent de différencier un proxy de la diffusivité ou de la conductivité thermique des différents milieux. Les épaisseurs de neige et de glace le long de la trajectoire de la bouée peuvent être déterminées à partir de ces observations (*Jackson et al., 2013 ; Provost et al. 2017*). Il est démontré dans le chapitre 4 que les données fournies par les SIMBAs permettent aussi d'estimer la conductivité de la neige, ce qui est nouveau.

Figure 5. Photo de la plateforme IAOOS + SIMBA. Campagne TRANSARC II, RV/Polarstern, 2015.

2. La modélisation numérique

La glace de mer est une composante essentielle des modèles océaniques, météorologiques et climatiques. Ces modèles peuvent être utilisés pour des études climatiques à long terme, des prévisions opérationnelles à court terme (dans les 10 prochains jours) et des prévisions saisonnières. Une représentation réaliste de la glace de mer et de la neige, et des échanges qui se produisent aux interfaces avec l'atmosphère et l'océan est indispensable pour obtenir des prévisions météorologiques réalistes et des projections climatiques raisonnables. Malheureusement cette représentation est encore très imparfaite. Améliorer les modèles de neige et de glace est donc une nécessité.

2.1 La modélisation de la neige et de la glace de mer

Nous avons vu dans le premier chapitre que deux types de processus affectent l'évolution de la glace de mer : (1) les processus thermodynamiques (agissant principalement verticalement et étant en première approximation à une dimension, 1D) qui imposent les taux d'ablation et d'accrétion de la glace de mer et (2) les processus mécaniques (faisant nécessairement intervenir les dimensions horizontales et dépendant des forçages mécaniques atmosphériques et océaniques) qui commandent la dérive, la déformation et le transport de la glace.

Dans les premiers modèles de climat, la glace de mer n'évoluait qu'en fonction des processus thermodynamiques. En 1971, *Maykut et Untersteiner* proposèrent un modèle unidimensionnel de glace de mer, calculant l'évolution du profil de température dans la glace et son épaisseur. Les variations verticales de salinité, du volume des poches de saumure et de conductivité étaient prises en compte dans ce modèle. Une version très simplifiée (niveaux verticaux réduits et utilisation de constantes au lieu de variables) de ce modèle (*Semtner, 1976; Parkinson et Washington, 1979*) est encore souvent utilisée dans les modèles climatiques.

À de grandes échelles spatiales (supérieure à 100 km), des scientifiques participant à l'expérience Arctic Ice Dynamics Joint Experiment (AIDJEX) ont suggéré que la glace de mer pouvait être assimilée à un milieu isotrope continu (*Coon et al. 1974*). Utilisant ces résultats, *Hibler* proposa en 1979 un modèle de glace de mer couplé dynamique/thermodynamique avec une rhéologie visco-plastique. Cette rhéologie a été par la suite modifiée (rhéologie élasto-visco-plastique de *Hunke et Dukowicz, 1997*) et ce type de modèle est encore majoritairement utilisé dans la plupart des modèles climatiques.

Les hypothèses d'isotropie et de continuité ont été récemment remises en question (*Coon et al., 2007 ; Rampal et al., 2008*), et des modèles anisotropes (*Hibler et Schulson, 2000*) ou discontinus (*Schreyer et al., 2006*) ont été développés. Ils ne sont pas encore utilisés dans les modèles développés pour les études climatiques. De même, les processus thermodynamiques à petite échelle qui jouent un rôle important dans le système atmosphère/neige/glace de mer/océan de l'Arctique, en particulier aux interfaces, ne sont toujours pas bien représentés dans ces modèles (*Vihma et al., 2014*).

Les modèles unidimensionnels de glace de mer ne considèrent que les processus thermodynamiques ; les processus mécaniques (en particulier la rhéologie) ne peuvent pas être représentés puisque le calcul des grandeurs ne se fait que sur la verticale. Par contre, ces modèles peuvent avoir des paramétrisations plus complexes que celles utilisées pour

les études climatiques (on l'a déjà vu pour le modèle fondateur de *Maykut et Untersteiner, 1971*). Ils peuvent donc contribuer à faire évoluer les modèles 3D dont la thermodynamique est plus simple. En effet, ce sont des outils efficaces pour développer et tester les paramétrisations des processus physiques et biogéochimiques au sein de la glace de mer et de la neige (*Vancoppenolle et Tedesco, 2017*). Ils aident à l'interprétation des observations de terrain, et fournissent des informations sur les paramètres qui ne peuvent pas être mesurés en continu tels que la salinité et le volume de poches de saumure.

L'une des difficultés majeures rencontrée par les modélisateurs est de représenter correctement l'évolution du profil de salinité, qui dépend de la température. En 1988, *Cox et Weeks* ont introduit une paramétrisation empirique couplée température-salinité dans un modèle thermodynamique de glace de mer. En 1999, *Bitz et Lipscomb* développèrent un modèle plus physique, et ainsi purent tenir compte du profil de température et de salinité non-linéaire dans le calcul de l'épaisseur de glace. Dans ce manuscrit, l'utilisation d'un modèle unidimensionnel de glace (LIM1D) inspiré du modèle de *Bitz et Lipscomb (1999)* permet de confronter efficacement les observations provenant des bouées dérivantes SIMBA à des simulations numériques (*Vancoppenolle et al., 2010*). Cette synergie modèle 1D/observations s'avère fructueuse comme on le verra dans les chapitres 3 et 5 principalement.

La thermodynamique de la glace de mer représentée dans le modèle LIM1D est décrite ci-dessous.

2.2 Échanges de chaleur dans la neige et la glace de mer

La glace de mer étant située entre l'océan et l'atmosphère, son taux de croissance ou de fonte dépend des flux de chaleur aux interfaces, c'est-à-dire de l'équilibre entre les flux atmosphériques, océaniques et les flux conductifs internes.

- **Conduction de la chaleur dans la neige ou dans la glace**

L'équation qui gouverne l'évolution du profil de température est de la même forme dans la neige et dans la glace. C'est l'équation de diffusion de la chaleur où l'on néglige les effets dus à la variabilité spatiale horizontale :

$$\rho C_p \partial_t T = \partial_z (k \partial_z T) + I_0 \kappa e^{-\kappa z} \qquad (1)$$

Dans cette équation ρ est la densité, C_p la chaleur spécifique, k la conductivité, I_0 la radiation transmise dans le milieu considéré, et κ le coefficient d'extinction provenant de la Loi de Beer-Lambert. Tous ces coefficients ont des valeurs numériques différentes dans la neige et dans la glace ; on mettra en indice la lettre "s" (pour *snow*) lorsqu'il s'agit de neige.

- **Flux à l'interface air/neige ou air/glace**

A l'interface air/neige (ou air/glace), les termes participant au bilan thermique d'origine radiative (échanges par rayonnement) sont (Figure 6) :

– le flux associé au rayonnement solaire incident (shortwave) F_{dsw}

– le flux de rayonnement infrarouge incident (longwave) F_{dlw}

– le flux de rayonnement infrarouge émis par la surface F_{ulw}

Les indices *dsw*, *ulw* et *dlw* font respectivement référence à "downward shortwave radiation", "upward longwave radiation" et "downward longwave radiation". En considérant que tout ce que le système reçoit est compté positivement et tout ce qu'il perd est compté négativement, le flux net radiatif résultant est donné par la relation

$$F_{net} = (1 - \alpha) F_{dsw} - I_0 + F_{dlw} - F_{ulw} \qquad (2)$$

où α représente l'albédo. Le terme I_0 apparaît dans l'équation (1) et représente la fraction de rayonnement solaire transmise à la neige ou à la glace si celle-ci est absente (de l'ordre de 17% en l'absence de neige).

En considérant la neige ou la glace de mer comme un corps noir, le rayonnement infrarouge émis par la surface est donné par la Loi de Stefan :

$$F_{ulw} = \sigma T_{surf}^{4}$$

où σ désigne la constante de Stefan-Boltzmann ($5.67 \times 10^{-8} W.m^{-2}.K^{-4}$) et T_{surf} la température de la surface.

Type de rayonnement	F_{dsw}	$(1-\alpha)F_{dsw}$	F_{dlw}	F_{ulw}	$F_{dlw}-F_{ulw}$	F_{tot}
Janvier	0	0	168	201	-33	-33
Février	0	0	166	193	-27	-27
Mars	39	6	166	195	-29	-23
Avril	162	31	191	231	-41	-10
Mai	282	56	243	280	-37	19
Juin	303	66	289	320	-31	35
Juillet	222	95	309	322	-14	81
Août	143	44	301	316	-15	29
Septembre	60	14	266	278	-12	2
Octobre	8	2	224	235	-12	-10
Novembre	0	0	183	206	-23	-23
Décembre	0	0	174	201	-27	-27
Annuel	101	26	223	248	-25	1

Tableau 1. Cycle saisonnier des flux radiatifs [W m−2] au centre de l'Arctique (De *Maykut, 1986*). Noter que F_{net}=F_{tot}-I_0

À l'interface air/neige on impose la continuité entre le flux conductif F_c dans la neige et l'ensemble des flux thermiques dans l'air :

$$F_c = F_{net} + F_l + F_s \quad (3)$$

Le flux de chaleur latente F_l et le flux de chaleur sensible F_s (d'origine turbulente) sont comptés positivement s'ils sont reçus par la neige. Si la neige est absente, la relation est la même mais à l'interface air/glace.

L'équation (3) est modifiée lorsque de la neige ou de la glace fond en surface : un terme supplémentaire dépendant de la chaleur latente de fusion de la glace est ajouté de la même façon qu'à l'interface glace-océan. Notons que la fonte est principalement due au rayonnement solaire durant l'été.

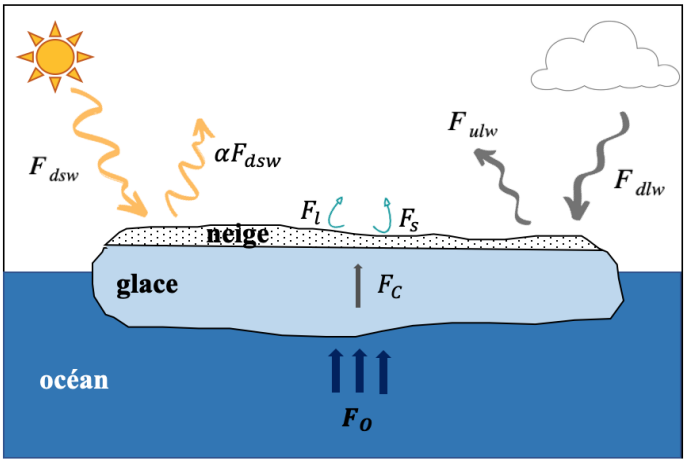

Figure 6. Bilan énergétique. Schéma inspiré du schéma donné dans Feys et Lietaer, 2005.

- **Interface neige/glace**

On impose la continuité du flux de chaleur sensible à l'interface neige/glace. Par conséquent, on peut écrire :

$$J_0 = -k_i\left(\frac{\partial T}{\partial z}\right)_{si} = -k_s\left(\frac{\partial T_s}{\partial z}\right)_{si} \qquad (4)$$

où l'indice *si* désigne l'interface neige/glace.

- **Flux à l'interface glace-océan**

A la base de la glace de mer, le bilan thermique comprend trois termes:

– le flux de chaleur océanique F_o

– le flux associé à la conduction de chaleur à l'intérieur de la glace F_c

– un terme résultant de la compétition entre ces deux flux et rendant compte des changements de phase se produisant à l'interface océan-glace.

Mathématiquement, l'équilibre entre ces termes à l'interface océan-glace se traduit par la relation suivante :

$$F_c - F_o = \rho L\left[\frac{dH}{dt}\right]_o \qquad (5)$$

où ρ est la densité de la glace de mer ($917\ kg/m^3$), L la chaleur latente de fusion de la glace de mer ($333.5 \times 10^3 J/kg$), F_c le flux conductif par unité d'air dans la glace, F_o le flux de chaleur océanique par unité d'air et H l'épaisseur de la glace de mer. L'indice "o" fait référence à l'interface glace-océan. Le flux conductif F_c dans la glace à la base de la glace est donné par la relation

$$F_c = -k\left(\frac{\partial T}{\partial z}\right)_o \qquad (6)$$

Lorsque l'un des flux domine sur l'autre, le système considéré (ici la glace de mer) va perdre ou gagner de l'énergie, ce qui se traduit par l'absorption ou la libération de chaleur latente et donc la formation ou l'ablation de glace.

2.3 Salinité dans la glace de mer

Comme vu précédemment, la glace de mer est un mélange de solide et de liquide. Cette coexistence liquide/solide augmente la complexité de la représentation de la glace de mer dans les modèles, dont les propriétés thermodynamiques, optiques, électriques et mécaniques dépendent toutes de la fraction volumique occupée par les poches de saumure, (fraction liquide).

- **Equilibre thermodynamique local**

Dans le modèle LIM1D, on suppose l'équilibre thermodynamique entre les poches de saumure et la glace environnante ; la température de congélation T_f de l'eau salée est donc liée à la salinité σ des poches de saumure. Pour simplifier, on choisit une relation linéaire entre ces deux grandeurs :

$$T_f = -\ \mu\sigma$$

où μ est une constante égale à 0.054 °C/‰. Autrement dit, une augmentation de salinité de 1 psu entraîne une diminution du point de congélation de l'eau de mer de 0.054 °C. Les inclusions sont à la température de congélation, en équilibre thermodynamique avec la glace environnante $T = T_f$. Les inclusions adaptent leur salinité σ à la température locale de la glace.

On suppose que l'intégralité du sel est dissout dans les inclusions liquides ou encore que la glace (sans les poches de saumure) est considérée comme pure (non salée). Dans ces conditions la relation reliant la salinité des poches de saumure à la *bulk salinity* est :

$$S = \sigma e$$

Lorsque la température diminue, la taille des inclusions diminue pour une salinité moyenne fixe. La salinité des inclusions augmente lorsque la température locale diminue. Lorsque la fraction des poches de saumure occupe un volume supérieur à 5% du volume total de glace, ces dernières sont connectées entre elles via des canaux et la saumure peut circuler dans la glace. Le modèle étant unidimensionnel, ces mouvements entre les poches de saumure interconnectées sont exclusivement verticaux (ce qui contredit les observations) et devront être paramétrés.

- **Conservation du sel dans la glace**

L'équation qui traduit la conservation du sel dans la glace de mer est complexe dans le cas général. Dans un modèle 1D on l'écrit sous la forme simplifiée suivante (voir par exemple *Vancoppenolle et al., 2010*) :

$$\frac{\partial}{\partial t}[S] = -e\upsilon_z \frac{\partial \sigma}{\partial z} + \frac{\partial}{\partial z}\left[eD_\sigma \frac{\partial \sigma}{\partial z}\right] \quad (7)$$

Cette équation nous dit que la salinité moyenne peut évoluer par advection du sel inclus dans les poches de saumure ou par diffusion suivant la verticale. Les coefficients υ_z (qui modélise la vitesse du fluide à travers les poches de saumure) et D_σ (qui permet de modéliser la diffusivité du sel dans l'eau) sont paramétrés dans le modèle.

Des conditions aux limites doivent être prescrites pour pouvoir intégrer ces équations. À la base de la glace on suppose que la salinité S_b est donnée par la relation suivante : $S_b = \nu_b S_w$ où S_w est la salinité de l'océan et ν_b un coefficient égal à 0.65 dans cette version du modèle. Au sommet de la glace, le flux de sel est supposé nul. Cependant lorsqu'il y a formation de glace de neige, on spécifie la salinité de la glace de neige grâce à la relation $S_{si} = \nu_{si}\left[\frac{\rho_i - \rho_s}{\rho_i}\right]S_w$ où ν_{si} est un coefficient égal à 1 dans la version standard du modèle.

Notons que l'on peut diagnostiquer les flux de sel à la base de la glace. Dans le cas le plus simple, le flux est égal à $F^s = F^s_{b,+} + F^s_{bd}$ où :

$F^s_{b,+} = -\frac{\rho_i}{1000}(1-\nu_b)S_w \frac{\partial h_{i,b+}}{\partial t}$ est le flux dû à la croissance basale de la glace et $F^s_{bd} = -\frac{\rho_i}{1000}\left[eD_\sigma \frac{\partial \sigma}{\partial z}\right]^{z=h}$ celui dû au drainage.

- **Paramétrisation de v_z**

Ce terme n'intervient que lorsqu'il y a de la fonte de neige ou de glace en surface et que la fraction volumique minimale de poches de saumure dépasse une valeur seuil de 5%. Nous n'avons jamais été dans cette situation mais nous donnons cependant son expression.

$$ev_z = Q = \phi \frac{\rho_x}{\rho_w} \frac{dh_x}{dt} \Big|_{su}$$

où ϕ est fixé à 0.3 (fraction d'eau autorisée à percoler dans la glace).

- **Paramétrisation de D_σ (et des effets convectifs halins)**

Dans un fluide au repos, le sel se diffuse de proche en proche sans mouvement apparent de matière. Ce processus est bien représenté par le dernier terme dans l'équation (7) avec D_σ constant et égal à la diffusivité du sel dans l'eau.

Dans le cas de la glace de mer, lorsque la fraction volumique des poches de saumure est importante (la glace est donc très poreuse) et que des différences de densité apparaissent dans la saumure prisonnière de la glace, cette saumure se met en mouvement : cela induit des changements de salinité bien plus importants que ceux provenant de la simple diffusion. Pour modéliser ce processus de convection dû principalement au sel, on introduit le nombre de Rayleigh (adimensionnel) : il mesure les effets de la gravité (qui vont mettre en mouvement le fluide) par rapport à ceux de la viscosité (qui vont freiner ces mouvements). *Notz et Worster* [2008] proposent de l'écrire pour le milieu poreux que constitue la glace de mer :

$$R_a = \frac{g(h_i - z)\rho_w \beta_w (\sigma(z) - S_w)\Pi(e_{min})}{\kappa_i \eta}$$

où g est l'accélération de la pesanteur, $\rho_w \beta_w (\sigma(z) - S_w)$ représente la différence entre la densité des brines au niveau z considéré et la densité de l'eau de mer à l'interface

glace-océan. La perméabilité effective de la glace $\Pi(e)$ dépend de la fraction volumique des poches de saumure et elle caractérise de façon quantitative la porosité du milieu. En suivant *Notz and Worster* [2008], la perméabilité est fixée à $10^{-17}\left[10^{3}e\right]^{3.1}$. Enfin e_{min} est la fraction volumique minimale de poches entre la profondeur z et l'interface glace océan.

Lorsque le nombre de Rayleigh atteint environ 10, la convection dans la glace se déclenche et devient dominante (*Vancoppenolle et al., 2010*). En toute rigueur, il faudrait la représenter par un terme d'advection dans l'équation (7). En pratique on la représente par le terme de diffusion en choisissant pour D_{σ} l'expression suivante :

$$D_{\sigma}(R_a) = I_w\left[\chi(R_a)D_{\sigma}^{tur} + (1 - \chi(R_a))\, D_{\sigma}^{mol}\right] \text{ où } \quad \chi(R_a) = \frac{tanh\left[(R_a - R_{ac})\right]+1}{2}$$

Le nombre de Rayleigh critique R_{ac} intervient dans l'expression de χ. Cette formulation en tanh permet de passer de façon continue d'une situation diffusive moléculaire à une situation diffusive "convective".

Notons qu'il existe des modèles bidimensionnels (*Petrich, 2006; Oertling et Watts, 2004*) qui calculent effectivement les vitesses des fluides dans la glace et représente ce phénomène de façon plus physique. Ces modèles sont coûteux en temps de calcul.

2.4 Résolution numérique avec le modèle LIM1D

Le modèle unidimensionnel LIM1D représente un grand nombre de processus physiques et biogéochimiques dans la glace et la neige. Dans la section qui suit, la partie biogéochimique n'est pas décrite car, bien qu'elle soit incluse dans le modèle, elle n'a pas été exploitée dans cette thèse.

- **Grandeurs fondamentales.**

On définit un axe vertical z, orienté vers le haut, dont l'origine est fixé au sommet de la glace ou à l'interface neige/glace s'il y a de la neige. Nous avons montré dans les sections 2.2 et 2.3 que l'état thermodynamique de la glace de mer pouvait être caractérisé par l'épaisseur totale de glace $h_i(t)$, par une cote verticale $z \leq 0$, par la température $T(t,z)$, par la salinité moyenne $S(t,z)$ (la "*bulk salinity*" qu'il faut bien distinguer de la salinité des poches de saumure $\sigma(t,z)$), et enfin par la fraction volumique des poches de saumure $e(t,z)$. Comme vu précédemment, il existe une relation qui lie ces deux dernières grandeurs. S'il y a de la neige, l'état thermodynamique de cette dernière est caractérisée par l'épaisseur de neige $h_s(t)$ et la température $T(t,z)$ pour $z \geq 0$. Ce sont ces grandeurs qui sont calculées de façon approchée par le modèle, après discrétisation.

- **Discrétisation des grandeurs et des équations**

Le nombre de couches dans la neige, N_s, et dans la glace, N_i est tout d'abord défini, comme sur la figure 7. La température, la salinité et la fraction volumique connues à un instant t_i au milieu de chacune de ces couches, ainsi que la température aux interfaces air/neige et neige/glace sont fixées. Alors, à l'aide des équations de la section 2.2 convenablement discrétisées, on peut en déduire les mêmes grandeurs aux mêmes points à un instant $t_i + \Delta t$.

La méthode suivie pour la température est une méthode implicite nécessitant plusieurs itérations pour que la condition à la limite soit satisfaite (en effet c'est une condition mixte de Neumann avec un terme non linéaire dû à la loi de Stefan en σT^4). La condition de Dirichlet à la base de la glace ($T = T_{oc}$) ne pose par contre aucun problème. On discrétise le laplacien puis on inverse une matrice tridiagonale. La discrétisation choisie permet de conserver l'enthalpie. Dans cette étape, l'épaisseur de neige ou de glace ne changent pas.

La technique est identique pour le sel mais nul besoin de faire des itérations puisque les conditions aux limites sont linéaires (flux de sel nul en surface (Neuman) et sel prescrit au fond (Dirichlet).

Noter que dans sa version de base, LIM1D modélise la neige par une unique couche de neige de densité et de conductivité constante. Afin de représenter la stratification de la couverture neigeuse, nous avons introduit plusieurs couches de neige de conductivité et de densité possiblement différentes (Chapitre 3 et 5).

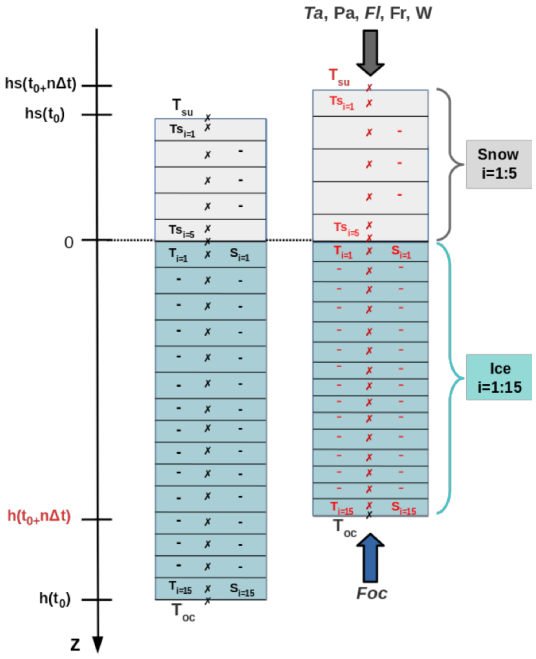

Figure 7. Schématisation du modèle LIM1D avec 5 couches de neige et 15 couches de glace.

Calcul de $h_i(t + \Delta t)$, conservation de l'enthalpie et du sel.

Le résultat du calcul précédent permet de satisfaire la condition à la limite en surface (dans les expériences présentées au chapitre 3 et 5, la neige et la glace ne fondait pas) mais ne permet pas de satisfaire la condition à la limite à la base de la glace. Le déséquilibre dans les flux à la base de la glace permet de calculer une nouvelle valeur pour $h_i = h_i(t + \Delta t)$. La nouvelle épaisseur de neige est, elle, prescrite. L'algorithme utilisé recalcule alors les profils de température dans la neige et dans la glace pour ces nouvelles épaisseurs de sorte

que l'enthalpie totale du système soit conservée. Les profils de salinité dans la glace sont calculés de manière à ce que le sel total soit également conservé (qui n'est pas expulsé). Cette redistribution est linéaire.

Pour que l'algorithme fonctionne, il faut l'initialiser convenablement et prescrire tout au long de l'intégration les grandeurs indépendantes des processus liés à la neige ou à la glace.

- **Initialisation du modèle**

Afin d'obtenir l'évolution temporelle de l'épaisseur de la glace et son profil de température et de salinité, il est nécessaire de déterminer les conditions initiales des variables indiquées dans le Tableau 2.

Variable	**Notation**	**Unité**
Epaisseur initiale de neige	h_s	m
Epaisseur initiale de glace	h_i	m
Température de surface à l'interface air/neige	T_{surf}	K
Profil de température dans la neige	T_s	K
Profil de température dans la glace	T_i	K
Profil de salinité dans la glace	S_i	psu

Tableau 2. Conditions initiales du modèle à définir.

Parmi ces conditions initiales, l'épaisseur de neige et de glace, la température de surface et les profils de température dans la neige et dans la glace sont bien connues à partir des observations SIMBA. Le profil de salinité est quant à lui, estimé.

- **Forçage du modèle**

Le tableau 3 fait la liste des grandeurs prescrites dans le modèle tout au long de l'intégration. La vitesse du vent, la température de l'air, la pression atmosphérique et l'humidité interviennent dans les calculs des flux de chaleur sensible et latent. Comme expliqué dans le chapitre 2.1, l'albédo, le flux océanique, le flux short wave et le flux longwave interviennent dans le bilan thermique de la glace. Quant au franc bord, il intervient lorsqu'il y a formation de glace de neige.

Variable	**Notation**	**Unité**
Vitesse du vent	W	m/s
Température de l'air	T_{air}	K
Pression atmosphérique	P_a	Pa
Humidité spécifique de l'air	q_{air}	kg/kg
Albédo	α	/
Flux océanique	F_{oc}	W/m^2
Flux shortwave	FS	W/m^2
Flux longwave	FL	W/m^2
Précipitations neigeuses	S_{fall}	$kg/m^2/s$
Salinité de l'océan	S_{oc}	psu
Franc bord	Fb	m

Tableau 3. Ensemble de variables imposées dans le modèle

Noter qu'une version du modèle avec les nouvelles paramétrisations sera mise à disposition.

Analyse d'observations hivernales de température et modélisation avec le modèle LIM1D

Sommaire

3.1 Résumé

Les processus physiques à petite échelle jouent un rôle important dans le système Arctique couplé atmosphère/neige/glace/océan. Ces processus sont complexes à représenter dans les modèles climatiques, en particulier ceux ayant lieu aux interfaces entre les différents milieux *(Vihma et al., 2014)*. Les modèles unidimensionnels de glace de mer et de neige sont des outils efficaces pour les analyser avec précision, pour développer et tester des paramétrisations et enfin pour interpréter des observations.

Navire RV-LANCE dans la glace de mer Arctique pendant la campagne N-ICE2015.

Dans cette première étude, la glace de mer hivernale de la zone située au nord du Svalbard est étudiée en utilisant des données SIMBA déployées lors de l'expédition N-ICE2015. Les observations sont confrontées aux simulations numériques obtenues à partir du modèle unidimensionnel de glace et de neige LIM1D. La qualité des simulations numériques a été évaluée en comparant les profils de température modélisés à ceux observés. Afin de représenter correctement le profil de température dans la neige, qui n'est pas toujours linéaire, il est nécessaire de représenter la neige par plusieurs couches (ici 5 couches suffisent). Une estimation de la densité de la neige (240-390 kg/m^3) a été obtenue par l'optimisation des simulations par rapport aux données.

Des expériences de sensibilité ont montré que les incertitudes sur la température de l'air et le flux radiatif "longwave" sont les principaux obstacles à l'amélioration des simulations quand la conductivité de la neige était correctement estimée. Le flux océanique est crucial pour représenter correctement la fonte basale et un mauvais profil initial de salinité dans la glace peut affecter la simulation des profils de température à long terme (pendant plusieurs mois). Le processus d'inondation et de formation de glace de neige est nouvellement observé en Arctique et peut être simulé de façon assez réaliste. L'évolution de la salinité et de la fraction volumique des poches de saumure (inaccessibles aux observations continues) peut également être déduite de ces simulations.

JGR Oceans

RESEARCH ARTICLE
10.1029/2019JC015431

Key Points:
- We revisited winter ice mass balance observations, using 1-D simulations of snow and ice temperature profiles
- We combined observations and 1-D modelling to adjust the snow density profiles, which are crucial for simulating sea ice evolution
- The simulations provided accurate temperature profiles and an estimation of ice salinity and brine fraction evolution during flooding

Correspondence to:
S. Gani,
sarah.gani@locean-ipsl.upmc.fr

Citation:
Gani, S., Sirven, J., Sennéchael, N., & Provost, C. (2019). Revisiting winter arctic ice mass balance observations with a 1-D model: Sensitivity studies, snow density estimation, flooding, and snow ice formation.. *Journal of Geophysical Research: Oceans*, *124*, 9295–9316. https://doi.org/10.1029/2019JC015431

Received 28 JUN 2019
Accepted 23 NOV 2019
Accepted article online 30 NOV 2019
Published online 17 DEC 2019

Revisiting Winter Arctic Ice Mass Balance Observations With a 1-D Model: Sensitivity Studies, Snow Density Estimation, Flooding, and Snow Ice Formation

Sarah Gani[1], Jérôme Sirven[1], Nathalie Sennéchael[1], and Christine Provost[1]

[1]IPSL/LOCEAN/UPMC/CNRS/IRD/MNHN, Sorbonne Université, Paris, France

Abstract We used a state-of-the art one-dimensional snow and ice model (the LIM1D model), to simulate data collected in winter 2015 north of Svalbard with ice mass balance instruments. The quality of the simulations was assessed by comparing simulated temperature profiles and sea ice thicknesses with the data: The root-mean-square difference between observed and modeled temperature was 1.06 °C in snow and 0.19 °C in ice, and the root-mean-square difference between simulated and observed ice thickness was 2.0 cm (snow depth was prescribed). The long-wave heat flux from the ERA-I reanalysis was adequate to perform winter numerical simulations; in contrast, the ERA-I air temperature induced large errors in the snow and ice temperature. Snow density had a direct impact on heat transfers and, thus, on the simulation. The joint use of the data and the simulations permitted the adjustment of the snow density profiles with a light (240 kg/m^3) snow deposited on top of a denser (370 kg/m^3) snow. The ice flooding, which occurred after a storm-induced breakup of floes loaded with snow, was simulated by prescribing the observed lower limit of the snow. The simulations provided insights on the evolution of sea ice bulk salinity, brine fraction, and the amount of snow ice formed during the flooding event.

Plain Language Summary A state-of-the-art snow and ice model (the model LIM1D) was used to simulate observations collected in winter 2015 north of Svalbard. The model estimated sea ice bulk salinity and brine fraction, which cannot be measured continuously. Combining observations and 1-D modeling allowed adjustments of the snow density (and conductivity) profiles, which have a critical impact on the simulation.

1. Introduction

During the past few decades, the Arctic sea ice regime has undergone large changes resulting in a smaller, thinner, and faster-moving ice cover (Lindsay & Schweiger, 2015; Spreen et al., 2011). The key role of sea ice in the global climate system motivated the development of thermodynamic and dynamic models to understand and forecast its evolution. Despite advances in numerical modeling, the reliability of present-day climate prediction models is limited in the Arctic and projected rates of sea ice decline remain uncertain (Overland & Wang, 2013). Several studies have investigated the sensitivity of sea ice thickness and area to model parameters and oceanic and atmospheric forcing. Sea ice thickness and extent were found to be most sensitive to ice density, albedo, and emissivity in summer and to the snow density, atmospheric and oceanic forcing in winter (Kim et al., 2006; Urrego-Blanco et al., 2016).

Small-scale physical processes that play an important role in the Arctic atmosphere/snow/sea ice/ocean system, in particular at the interfaces, are still not well represented in climate models (Vihma et al., 2014). One-dimensional sea ice models can help improve this situation. They provide efficient tools for developing and testing parameterizations of physical and biogeochemical processes within sea ice and snow and for interpreting field observations (Vancoppenolle & Tedesco, 2017). One-dimensional models may help to interpret the data collected with ice mass balance instruments and provide complementary information on parameters that cannot be measured continuously. Huwald et al. (2005) developed a multilayer sigma-coordinate thermodynamic sea ice model and compared simulations to the observational data from the Surface Heat Budget of the Arctic Ocean experiment (Persson et al., 2002). When the initial ice thickness was correctly prescribed, their model reproduced the observed ice thickness and temperature profiles in snow and ice with differences not exceeding 3 °C. They underlined the sensitivity of the ice thickness to the ocean heat flux and to the snow cover in winter. Using the LIM1D model, Lecomte et al. (2011) tested a new snow

thermodynamic scheme at point Barrow (Alaska) and at Ice Station POLarstern in the western Weddell Sea. They emphasized the need for several snow layers (between three and six) for a precise estimation of the temperature inside the snow. Duarte et al. (2017) simulated the spring ice mass balance data from the N-ICE2015 expedition with the Los Alamos sea ice model (CICE) and reproduced the ice temperature with a root-mean-square difference (RMSD) of 0.47 °C. Dupont et al. (2015) compared sea ice representation through different numerical approaches and concluded that the Bitz and Lipscomb (1999) finite difference approach, the sigma-coordinate model of Huwald et al. (2005), and its variant based on finite elements all converge to the same solution.

In this study, we combine high-resolution winter Arctic observations with the snow and ice model LIM1D (Vancoppenolle et al., 2008). The observations were collected during the Norwegian young sea ICE expedition (N-ICE2015), which provided an observing platform for atmosphere, snow, sea ice, and ocean from January to end of June 2015, north of Svalbard (Granskog et al., 2016). The winter observations from Sea Ice Mass Balance instruments (SIMBA) showed abundant snowfalls and intense basal sea ice melt. They also provided the first documentation of significant flooding and snow ice formation in the Arctic ice pack (Provost et al., 2017; Figure 1).

The main aim of this study is to revisit these high-resolution winter Artic data series with a modeling point of view, to improve our understanding of the physical processes within sea ice and snow. We simulated snow and sea ice temperature profiles over two SIMBA drifts. A few sensitivity studies guided our choice of atmospheric and oceanic forcing, snow conductivity parameterization, and initial ice salinity. The joint use of the simulated and observed temperature profiles allowed adjustments of the snow density profiles. Once a good agreement between observed and simulated temperature profiles was reached, we analyzed salinity and brine volume fraction (physical properties that cannot be measured continuously). In particular, flooding events were simulated and salinity and brine fraction were used to investigate the process of snow ice formation.

The paper is organized as follows. Section 2 describes the model, the observations, and the forcing terms. A reference run and sensitivity studies are presented in section 3. In section 4, snow density profiles are adjusted combining data and simulations. The processes of flooding and subsequent snow ice formation are analyzed in section 5. Finally, section 6 summarizes the results and provides perspectives.

2. Model and Observations

2.1. The LIM1D Model

The LIM1D model described in Vancoppenolle et al. (2008, 2010); Vancoppenolle and Tedesco (2017) is based on the enthalpy conserving scheme proposed by Bitz and Lipscomb (1999). We summarize its main characteristics, emphasizing aspects that are pertinent for this study.

In its simplest configuration, the model computes at each time step t and depth z the following fundamental quantities:

snow temperature $T_s(z,t)$,

ice temperature $T(z,t)$ and bulk salinity $S(z,t)$,

sea ice thickness $h(t)$.

The model solves the heat equation in snow and sea ice and a supplementary advective-diffusive equation for the salt in sea ice (Vancoppenolle et al., 2010). The heat equation reads:

$$\rho_i c \frac{\partial T}{\partial t} = \frac{\partial}{\partial z}\left(k \frac{\partial T}{\partial z}\right) + Q_{sw} \tag{1}$$

where $c = 2{,}060$ J/kg/K is the ice specific heat, ρ_i is the ice density ($\rho_i = 917$ kg/m^3), k is the ice conductivity (W/m/K), and Q_{sw} is the absorption of solar radiation.

The equation for salinity conservation in sea ice is

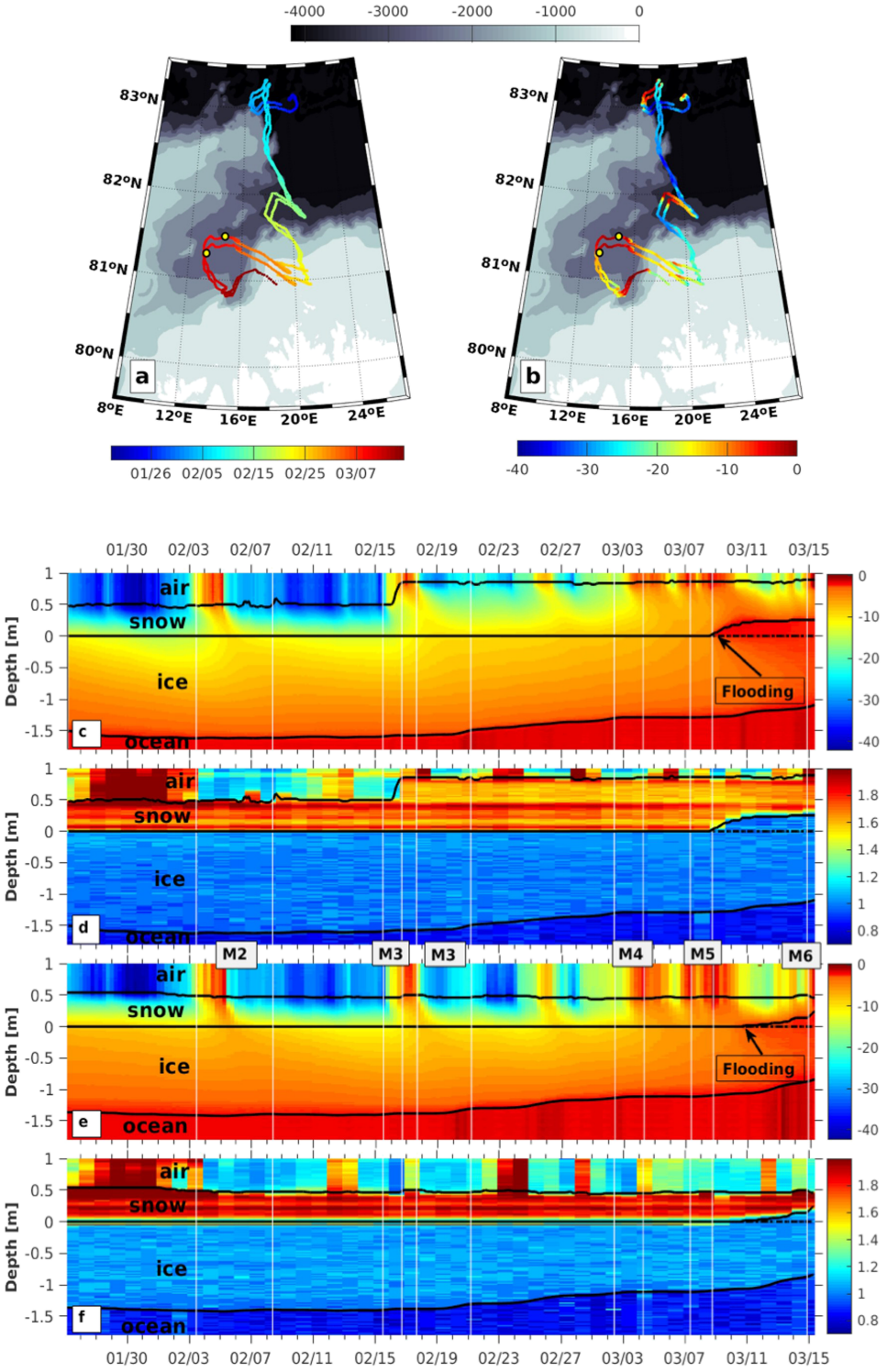

Figure 1. (a) Time and (b) air temperature along the SIMBA_a and SIMBA_h drift trajectories (°C). The background is bathymetry (m). Yellow circles indicate the onset of the flooding events. (c) Temperature (°C) as a function of time for SIMBA_h. (d) Thermal diffusivity proxy* (no units) as a function of time for SIMBA_h. (e) Same as (c) for SIMBA_a. (f) Same as (d) for SIMBA_a. Vertical resolution is 2 cm. Black lines correspond to the air/snow interface, the lower limit of the snow layer and ice/ocean interface. Temperature color scale is nonlinear in order to highlight temperature changes in the ocean. Storms are labeled M2, M3, … , M6 as described in Cohen et al. (2017). * The heating mode produces a heat pulse and the temperature response to the heat pulse depends on the medium and provides the diffusivity proxy (Jackson et al., 2013).

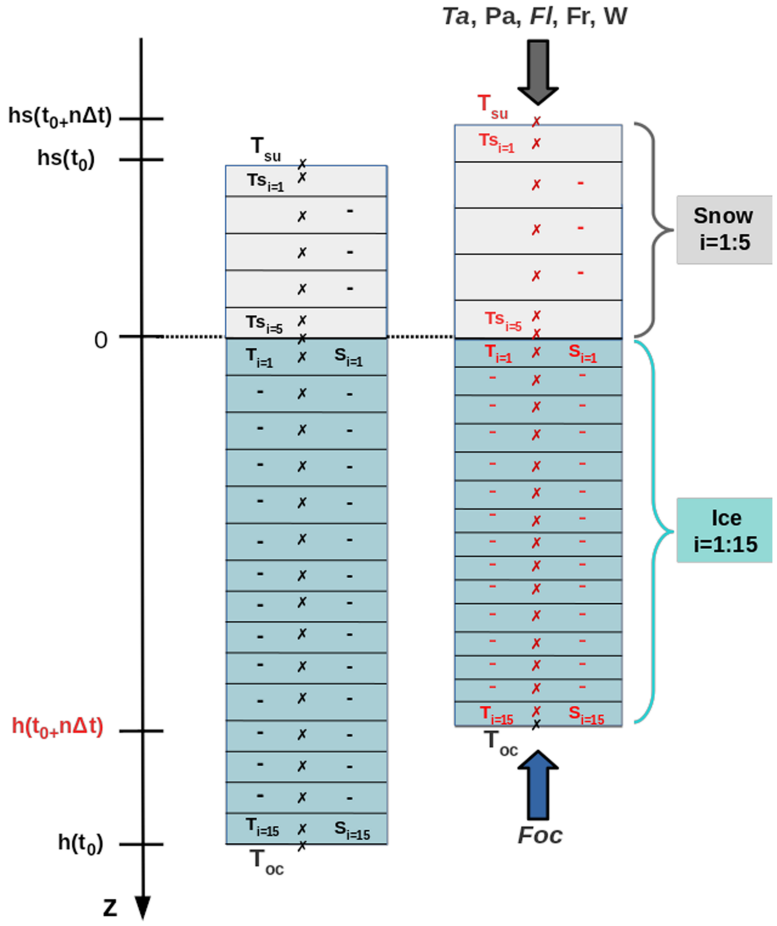

Figure 2. Schematics of LIM1D model. Five snow layers of equal thickness (gray) and 15 sea ice layers of equal thickness (blue) evolve over time. Initial condition (t_0) and prescribed values are in black, and calculated values at each time step (t) are in red. h_s: snow thickness, h_i: ice thickness, T_A: air temperature, P_A: sea level pressure, F_L: long-wave flux, F_R: short-wave flux, W: wind, T_S: snow temperature T_i: ice temperature, T_{OC}: ocean temperature, F_{OC}: ocean flux, S_i: ice salinity. The time step of the model is 1 hr.

$$\frac{\partial S}{\partial t} = -\nu_z \frac{\partial S}{\partial z} + \frac{\partial}{\partial z}\left[D_\sigma \frac{\partial S}{\partial Z}\right] \tag{2}$$

with ν_z being the vertical velocity of the fluid within the brine network (m/s) and D_σ the salt diffusivity in water (m^2/s).

The system is divided into a fixed number of layers in the ice and snow, as indicated in Figure 2. At each time step, enthalpy and salinity are redistributed to follow the thickness changes in such a way that the enthalpy and the salt content are conserved. Other physical quantities (such as the brine volume fraction $e(z,t)$ in the sea ice and the brine salinity $\sigma(z,t)$) are derived from the fundamental ones. The initial values $h(t_0)$, $T(z, t_0)$, $S(z, t_0)$, and $T_s(z, t_0)$ are prescribed. Various quantities are necessary to force the model.

Atmospheric heat fluxes are required at each time step of the integration. Incoming short-wave radiation F_r and incoming long-wave radiation F_L are introduced in the model through the following boundary condition, applied at the upper boundary of the snow, $z = h_S(t)$:

$$-k_s \frac{\partial T}{\partial z} = (1-\alpha)F_r - I_0 + F_L + \epsilon_L \sigma_S T_{surf}^4 + F_S + F_{La} \tag{3}$$

where α is the surface albedo ($\alpha = 0{,}85$), I_0 is the incoming short-wave radiation that penetrates through the

snow ($I_0 = 0.22(1-\alpha)F_R$), ε_L is the emissivity ($\varepsilon_L = 0.95$), σ_S is the Stefan constant ($\sigma_S = 5.67.\ 10^{-8}$ W/m^2/K^4), k_S is the snow conductivity (W/m/K), and F_{La} is the latent heat flux (W/m^2).

The surface temperature of the snow $T_{\mathrm{surf}}(t)$ (equation (3)) is computed by the model. It differs from the air temperature $T_a(t)$, which is prescribed and permits to compute the sensible heat flux F_S (W/m^2):

$$F_s(t) = C_p \rho_a\, u_a C_H (T_{\mathrm{surf}}(t) - T_a(t)) \tag{4}$$

where u_a is the wind velocity (m/s), ρ_a the air density ($\rho_a = 1.275$ kg/m^3), C_p the air specific heat ($C_p = 1{,}005$ J/kg/K), and C_H the bulk transfer coefficient for sensible heat at neutral stability ($C_H = 1.75 \times 10^{-3}$). The coefficient C_H depends on the surface roughness parameter and on the wind speed (Andreas, 1987). The use of this constant value has been a common strategy since (Maykut, 1978).

The latent heat flux F_{La} (equation (3)) is proportional to the difference $q_s - q_a$, where q_s is the surface humidity and q_a the prescribed air humidity (kg/kg). F_{La} is small in comparison with the other fluxes.

At each time step of the integration, the evolution of the sea ice thickness is computed by satisfying the boundary condition at the lower boundary of the sea ice $z = h_i(t)$:

$$-\mathrm{k}\left.\frac{\partial T}{\partial z}\right|_i - \rho_i L \frac{\mathrm{dh}}{\mathrm{dt}} = F_{\mathrm{OC}} \tag{5}$$

where F_{OC} is the ocean heat flux and L the latent heat of fusion of ice ($L = 333.5 \times 10^3$ J/kg). The temperature at the base of the sea ice $T(h(t), t)$ is also prescribed. This is equivalent to prescribing the ocean salinity $S_{\mathrm{OC}}(t)$ via the approximate liquidus relation $T(h(t), t) = -\mu \mathrm{S}_{\mathrm{OC}}(t)$, where μ is a constant ($\mu = 0.054$ ° C/‰).

We decided to prescribe the upper limit of the snow (this is here equivalent to prescribing the local snowfall) instead of the ERA-I precipitation; the observed snow thickness depends upon the location of the SIMBA on the floe (local accumulation, wind, and snow deposition; Provost et al., 2017). We also prescribed the lower limit of the snow. Using the Archimedes' principle, the 1-D model computes the position of the local waterline (or equivalently the height between the snow base and the waterline: the freeboard). In the experiments, the simulated waterline was above the snow ice interface, which induced an intrusion of seawater into the snow layer. The local position of the waterline depends on the global characteristics of the floe (the size of the floe, the snow cover and ice thickness, and the ice rheology). Prescribing the lower limit of the snow (at $z = 0$) prevents the seawater intrusion; before the flooding, the lower limit of snow was the snow/ice interface and after, the snow/slush interface.

The density of the snow ρ_s can be adjusted. The snow conductivity is given by Abel's relation $k_s = 2.846 \times 10^{-6} \rho_s^2$.

In the ice, the salinity of brine pockets $\sigma(z,t)$ is computed from the temperature of sea ice using the liquidus relation $T(z,t) = -\mu\sigma(z,t)$. The brine fraction $e(z,t)$ represents the amount of liquid water in the ice and depends on the bulk salinity $S(z, t)$ and the local ice temperature $T(z, t)$:

$$e(z,t) = \frac{S(\mathrm{z},\mathrm{t})}{\sigma(\mathrm{z},\mathrm{t})} = -\mu \frac{S(\mathrm{z},\mathrm{t})}{T(\mathrm{z},\mathrm{t})} \tag{6}$$

The ice conductivity $k(z,t)$ and specific heat $cz,t)$ have a complex expression deduced from empirical measurements (Pringle et al., 2007):

$$k(z,t) = 2.11 + 0.09 \frac{S(\mathrm{z},\mathrm{t})}{T(\mathrm{z},\mathrm{t})} - 0.011\ \mathrm{T}(z,t) \tag{7}$$

and

$$c(\mathrm{z},\mathrm{t}) = 2062 + L\mu \frac{\mathrm{S}(\mathrm{z},\mathrm{t})}{T(\mathrm{z},\mathrm{t})^2} \tag{8}$$

where the temperature $T(z, t)$ is in degrees Celsius (°C).

These relations control the impact of salinity on the evolution of the temperature profile in the ice.

The continuity of the heat fluxes between ice and snow is imposed:

$$-k_s \frac{\partial T}{\partial z}\bigg|_s = -k \frac{\partial T}{\partial z}\bigg|_i \tag{9}$$

The heat equation (1) provides a first estimation of the temperature profile at $t_{i+1} = t_i + \delta t$ from their values at t_i ($\delta t = 1h$)using the boundary condition (equation (3)) and the prescribed value $T(h(t), t) = T_{oc}$. Because the term $\epsilon_L \sigma_S T_{surf}^4$ is nonlinear, an iterative implicit method is used. Then the equation for salinity is solved (Vancoppenolle et al., 2010). The ice thickness is computed from equation (5). The temperature and salinity profiles are then modified in such a way that the enthalpy of the system composed of new snow, old snow, and sea ice is conserved. All numerical experiments shown here were performed with 15 layers of sea ice and 5 layers of snow (Figure 2).

2.2. Observations

The Research Vessel Lance (RV Lance) drifted with the Arctic ice pack from January to end of June 2015, north of Svalbard (Granskog et al., 2016). Throughout winter 2015, the Arctic vortex was strong with large amount of northward air volume transport over the Greenland Sea. Six synoptic events (storms) characterized by strong winds occurred and brought warm air from the south and heavy precipitation (Graham et al., 2016; Hudson & Cohen, 2016). Precipitation rates based on ERA-Interim reanalysis (Dee et al., 2011) showed that winter 2015 faced exceptionally abundant snowfalls; the one of February 2015 was the second largest in the ERA-Interim reanalysis record (1979–2015) for the N-ICE2015 region (Merkouriadi et al., 2017).

Seven SIMBAs recorded repeated profiles of temperature and thermal diffusivity proxy (Provost et al., 2017). We focused on the two longest SIMBA time series called SIMBA_a and SIMBA_h (Figure 1). The SIMBA data showed limited sea ice growth until mid-February and intense basal sea ice melt when the ice floe drifted over the warm Atlantic waters on the continental slope north of Svalbard. The ocean-to-ice fluxes peaked at 300 W/m^2 and induced a 0.50 m loss of ice in one month (Figures 1c–1f). The SIMBAs also provided the first documentation of significant flooding and snow ice formation in the Arctic ice pack. Flooding was a consequence of negative freeboard conditions due to a heavy snow load relative to the ice thickness and a storm-induced breakup of the floes. From isotope analysis of 29 ice cores collected during the N-ICE 2015 expedition, Granskog et al. (2017) estimated that snow ice contributed to 7.5–9.7% of the sea ice mass balance on average.

2.3. Model Forcing

2.3.1. Atmospheric Forcing

The long-wave flux F_L, the short-wave flux F_r, and the air temperature T_a are available from the global reanalysis ERA-Interim (ERA-I), with a 6 hr time resolution (Figure 3, red curves in panels a–c; Dee et al., 2011). Because of the polar night, F_S was null until March; then it slowly increased with a strong diurnal daily cycle, without exceeding 45 W/m^2 (Figure 3b).

The long-wave fluxes F_L and F_r are also available from direct measurements made on the RV-Lance with a 30 min time resolution (Hudson & Cohen, 2016; Figure 3a, black curve). Measurements from the ship could only be used before 20 February, when the ship was forced to relocate northward after a massive floe breakup. During the drift, F_L varied between 120 and 300 W/m^2 and exhibited variations largely correlated with the air temperature (Figures 3a and 3c). Air temperature is also available with a 1 hr resolution from the IAOOS7 (Ice Atmosphere Ocean Observing System) buoy on which SIMBA_h was installed (Koenig et al., 2016; Figure 3c, blue curve). The air temperature ranged from −42 to 0 °C and exhibited sudden peaks associated with the storms, in addition to a gradual warming trend throughout the observation period. ERA-I air temperature is larger than the observed one during cold winter conditions (by 8 °C) and smaller during warm periods (by −5 °C; Cohen et al., 2017).

The wind speed at 10 m is available from ERA-I with a 6 hr resolution. It varied between 2 and 21 m/s (Figure 3d), and the large wind speeds correspond to the storm events described in Cohen et al. (2017). The largest values were correlated to the increase of temperature and long-wave flux (Figures 3a, 3b, and 3d).

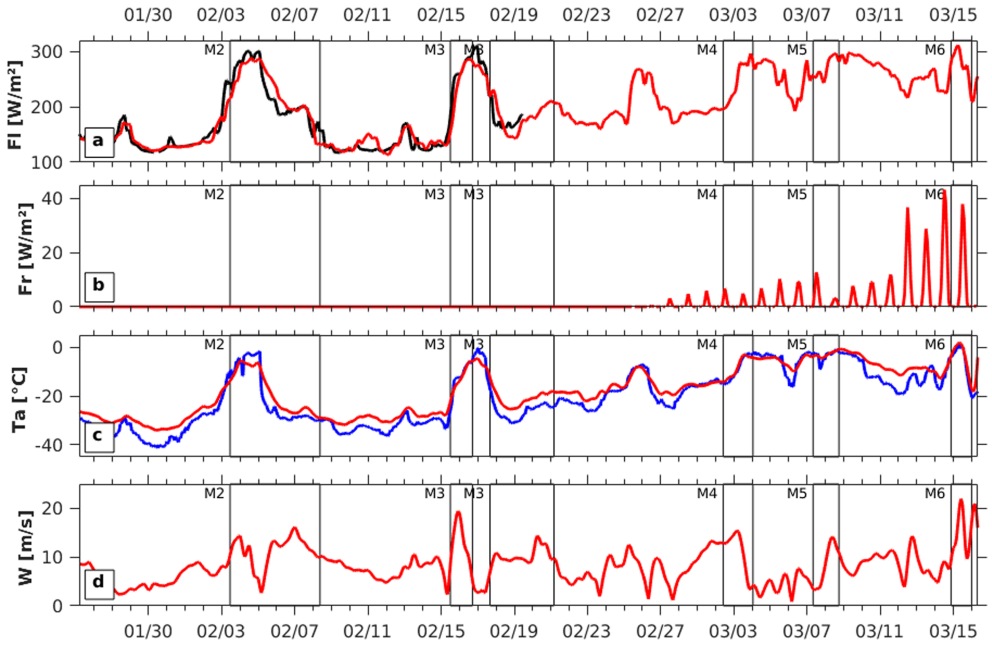

Figure 3. Time series of the atmospheric forcings: (a) long-wave flux from ERA_I (red) and RV_LANCE (black), (b) short-wave flux from ERA_I, and (c) air temperature (blue: from the IAOOS central unit; red: from ERA_I). (d) Wind speed from ERA_I. Storms are labeled M2, … , M6 as described in Cohen et al. (2017).

All the data series (ERA-I, RV-Lance) have been interpolated to fit the 1 hr time step of the model.

2.3.2. Forcing Deduced From SIMBA Snow and Ice Observations

SIMBA_a and SIMBA_h recorded different values of snow and ice thickness (Figure 4a). At the SIMBA_h site, the snow thickness remained nearly constant (around 55 cm) then increased by about 40 cm at the beginning of storm M3 and did not evolve much until 8 March (blue curve, Figure 4a). At SIMBA_a site, the snow thickness remained constant the first 6 days and lost 10 cm at the beginning of the M2 storm. Then, it remained mostly constant (around 45 cm) until 9 March, when a flooding began (red curve, Figure 4a).

The lower limit of the snow (referenced to its initial value $z = 0$) remained unchanged until the seawater invaded the snow (storm M5) and reached a maximum value of 34 cm at SIMBA_h site (24 cm at SIMBA_a). As previously indicated, the lower limit of snow was used to trigger and control the flooding event.

The ocean temperature Toc ranged between −2 and −0.7 °C for SIMBA_a and −1.9 and −1.2 °C for SIMBA_h (Figure 4c). A systematic difference of 0.1 °C is visible in Figure 4. A comparison with the five other SIMBAs in the vicinity (Provost et al., 2017; shorter time series, not shown) outlined a cold bias in SIMBA_a temperature, which has been corrected. Before 19 February, the ocean temperature was more or less constant and close to the ocean freezing temperature, for both buoys. After 19 February, the two buoys drifted over warmer water above the continental slope north of Svalbard. The ocean heat flux F_{OC} computed from the melting rate of sea ice and the sensible heat flux (Provost et al., 2017) for SIMBA_a and SIMBA_h varied between −100 and 300 W/m^2 and followed the ocean temperature variations (Figure 4d).

3. Reference Run and Sensitivity Studies for SIMBA_h

3.1. Reference Run

The reference run was initialized with snow thickness, sea ice thickness, and temperature profile observed on 26 January (Figure 5a, left). The initial bulk salinity profile was taken from an ice core collected close to the buoy SIMBA_h (83.5°N, 18.9°E) on 26 January (Granskog et al., 2017; Figure 5c, left). We chose the classic values of 2062 J/kg/K for the snow specific heat and 917 kg/m^3 for the pure ice density. According to the

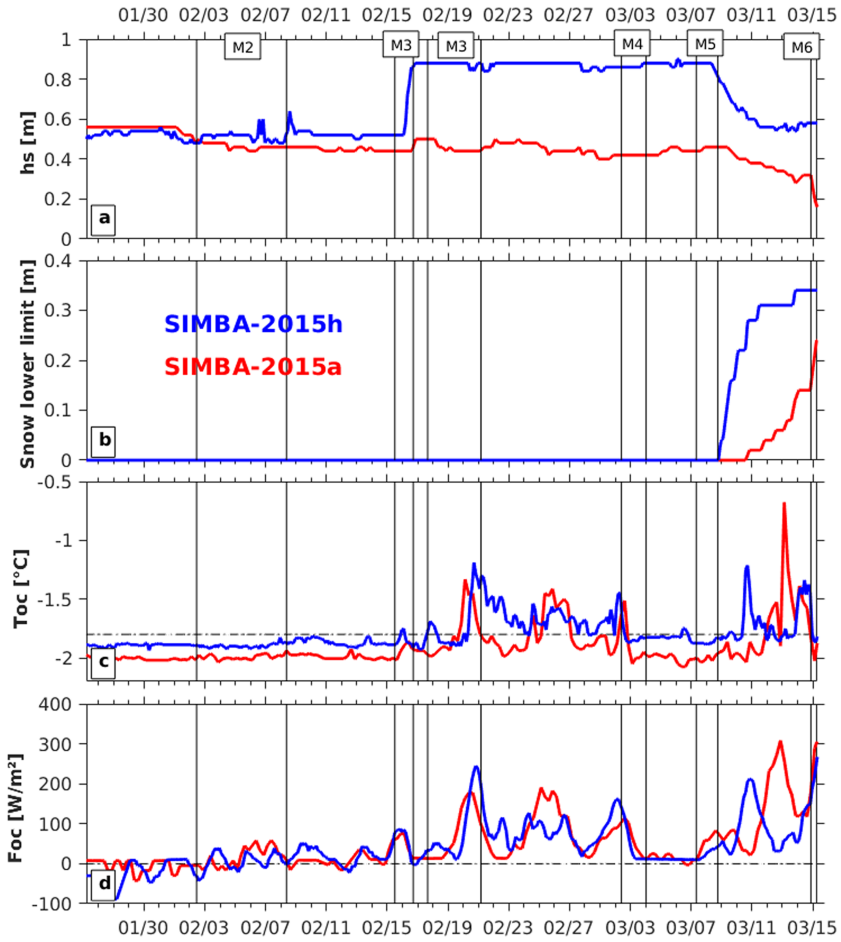

Figure 4. Time series derived from SIMBA observations (Provost et al., 2017; blue curve for SIMBA_h and red curve for SIMBA_a): (a) snow thickness, (b) lower limit of the snow layer on the SIMBA chain, (c) ocean temperature, and (d) ocean heat flux. Storms are labeled M2, … , M6 as described in Cohen et al. (2017).

observations, the snow density was 390 kg/m^3 (Merkouriadi et al., 2017). The associated conductivity was 0.43 W/m/K. The reference run was forced with ERA-I long-wave and short-wave flux and the IAOOS7 air temperature (Table 1).

Until the flooding event, the simulated ice thickness never differed from the observations by more than 2 cm (not shown), the observed thickness uncertainty. This result shows the consistency of the ocean heat fluxes computed by Provost et al. (2017).

The simulated temperature profiles were close to the observations (Figures 5a and 5b) with a RMSD between the observed and simulated temperature of 1.06 °C in the snow and 0.19 °C in the ice (Table 2). The storms induced an increase of the snow surface temperature, which then diffused through snow and ice. The lower boundary of the snow was prescribed to trigger the flooding event of 8 March. The snow located under this limit was filled with seawater at the freezing temperature, leading to a rapid increase of the temperature at the snow/ice interface (from −5.9 to −1.9 °C in less than 5 hr). The flooding impinged on the surrounding ice down to 0.60 m depth with an ice temperature increase of about 2 °C.

Temperature differences with the observations never exceeded ±3 °C in the snow and were maximum close to the snow/air interface (Figure 5b), suggesting atmospheric fluxes as possible source of error. The temperature difference between simulation and observation in the sea ice never exceeded ±1.2 °C (0 to 0.5 °C during most of the run, Figure 5b). The temperature of the slush layer associated with the flooding was also well represented. The temperature difference between model and observation was lower than 0.4 °C in the slush layer and surrounding ice.

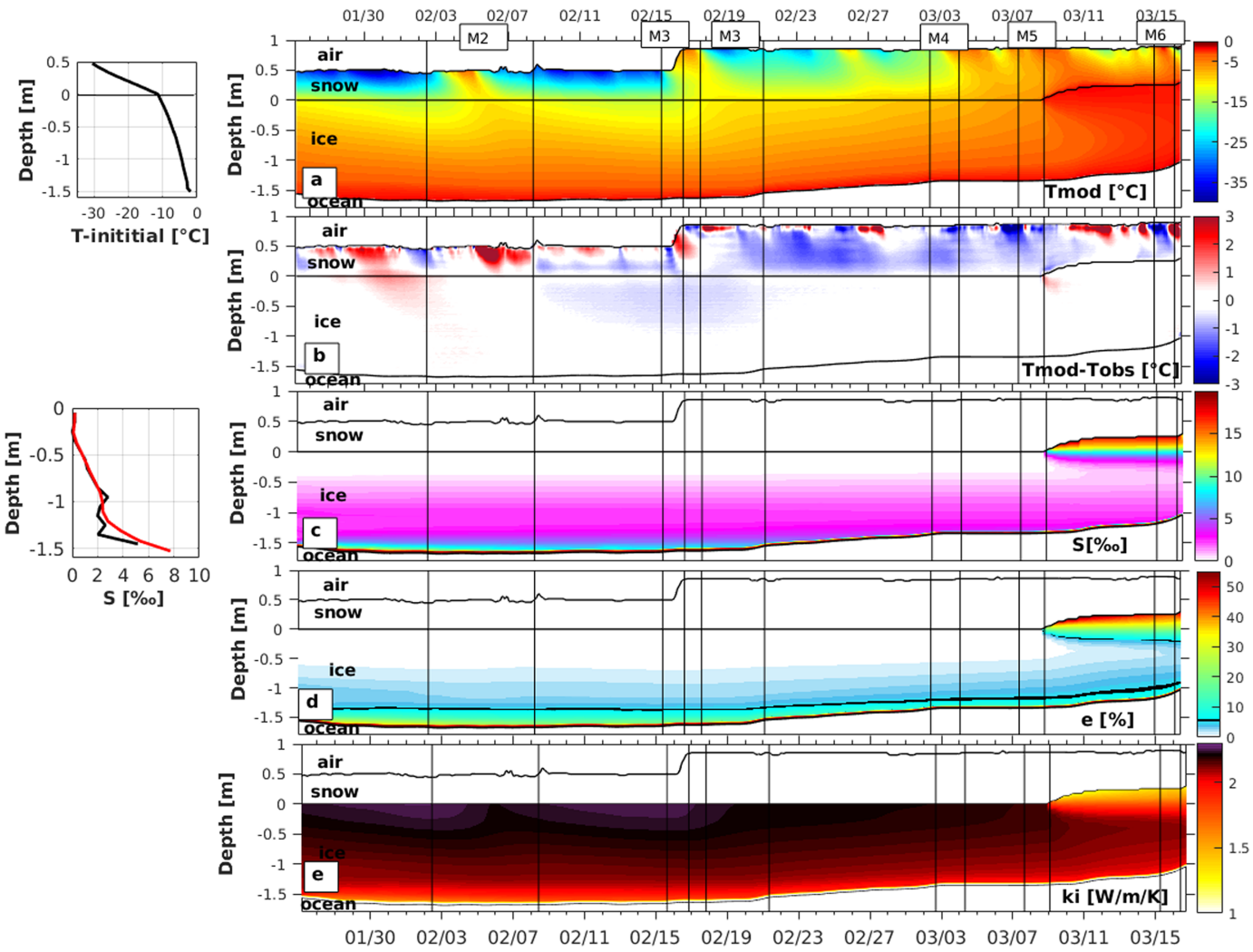

Figure 5. Reference run for SIMBA_h. (a) Left: initial observed temperature profile in snow and ice. Right: simulated temperature as a function of time in snow and ice. (b) Temperature differences between simulation and observations. Model outputs are interpolated to the vertical resolution of the data (2 cm). (c) Left: initial observed ice salinity profile (black) from Granskog et al. (2017) and simulated salinity profile on 26 January (red). Right: simulated ice salinity as a function of time. (d) Simulated ice brine fraction as a function of time. The black isoline corresponds to the 5% brine fraction. (e) Time series of the simulated ice conductivity. On all the panels, black lines correspond to the air/snow interface, the lower limit of the snow layer and ice/ocean interface. Storms are labeled M2, M3, ... , M6 as described in Cohen et al. (2017).

The simulated salinity profiles rapidly became smoother than the observed initial profile (Figure 5c, left). The bulk salinity remained close to 0‰ at the snow/ice interface and increased with depth to 2.5‰ at 1.0 m depth (Figure 5c). In the lowermost 5–10 cm, the bulk salinity increased to reach the prescribed value at the ice/ocean interface. When flooding began, salinity of the immersed snow layer drastically increased: the salinity of the slush layer reached 19‰ (Figure 5c).

Table 1
Forcing and Initial Conditions for the Reference Run (First Column) and the Different Simulations for the Sensitivity Studies (the Modified Characteristics With Respect to the Reference Run Is Indicated)

	Reference run	Run A	Run B	Run C	Run D	Run E
Oceanic flux	Provost et al. (2017)	Smoothed noisy constant				
Long-wave flux	ERA-I		R/V Lance			
Air temperature	IAOOS buoy			ERA-I		
Initial ice salinity profile	Granskog et al. (2017)				5‰	
Snow conductivity	Abel's					Sturm et al. (1997)

Table 2
Root-Mean-Square Difference Between the Observed and Simulated Temperature in Snow and Ice for the Reference Run and the Runs Corresponding to the Sensitivity Studies (°C)

RMSD (°C) SIMBA_2015h	Reference run	Run B	Run C	Run D	Run E
Snow layer					
Entire run	1.06	/	2.00	1.17	1.58
Part 1 (until 19 February)	1.01	0.92	1.61	1.17	1.36
Ice layer					
Entire run	0.19	/	0.26	0.35	0.84
Part 1 (until 19 February)	0.23	0.24	0.33	0.31	0.77

Note. The statistical significance of the difference between each sensitivity study and the reference run was assessed using a Fisher test on the RMSD. They all passed the test at the 95% CL.

The brine fraction is the relative volume of salty water in the ice. For a brine fraction larger than 5%, sea ice is considered as permeable and brine pockets are interconnected (Golden et al., 1998). With a brine fraction between 50% and 60%, ice becomes mobile, forming a cohesive slush; with a brine fraction over 60%, ice has no more cohesion and becomes a loose slush (Jutras et al., 2016). Most of the simulated ice layer had a brine fraction smaller than 5% (Figure 5d). Brine fraction increased near the ice base (over 10 cm) and reached 97% at the ice/ocean interface (for salinity = 34‰, $T = -1.84$ °C). The cohesive slush was approximatively 1 cm thick, and the last 3 cm above the open ocean were made of loose slush. The brine fraction at 0.5 m depth increased from 0% to 5% at the end of the simulation (Figure 5d). The brine fraction in the ice, near the snow/ice interface, was close to zero before 8 March and reached a maximum of 20% after the infiltration of salty seawater in the snow layer. The flooding and the resulting snow ice formation are studied in section 5.

The ice thermal conductivity is controlled by salinity and temperature (equation (7)). When the temperature at the snow/ice interface increased, the ice conductivity decreased (Figure 5e). On 4 February, the air temperature suddenly rose up to −2 °C, leading to a decrease of the ice conductivity, from 2.4 to 2.1 W/m/K at the snow-ice interface (Figure 5e). The salinity at the snow ice interface ($z = 0$) drastically increased when flooding occurred, leading to a decrease of the conductivity from 2.1 to 1.6 W/m/K.

3.2. Sensitivity Studies

We performed simulations to evaluate how changes in the external forcing, initial salinity profile, and snow conductivity may affect the simulated snow and sea ice temperature profiles. Table 1 summarizes the different simulations, and Table 2 provides the RMSD between the observed and simulated temperatures in snow and ice.

3.2.1. Oceanic Flux

Usually, when the ocean heat flux is not available, a constant value is used to force sea ice models. Here, the ocean heat flux computed by Provost et al. (2017) is available with a 3 hr time resolution. This provided the opportunity to evaluate the impact of the time resolution of the oceanic heat flux on the simulation.

We used three different ocean heat fluxes: constant, smoothed, and noise-added fluxes (Figure 6a). The smoothing was obtained with a 10-day running mean. The added white noise had an amplitude of 112 W/m^2, which is twice the oceanic flux estimate uncertainty (Provost et al., 2017). The three heat fluxes had the same mean value as the reference ocean flux (48 W/m^2). The RMSD with the reference oceanic flux is 32 W/m^2 for the smoothed flux and 56 W/m^2 for the constant and the noise added fluxes.

The final ice thickness was the same in all simulations as all ocean fluxes had the same mean over the time period (Figure 6b). The constant flux led to a continuous basal melt, and the ice thickness difference with the reference run reached 30 cm on 19 February (blue curve in Figure 6b). The largest impact on the ice thickness of the smoothed flux occurred during the intense basal melt (6 cm on 15 March), while the impact of the noise added flux never exceeded 2 cm (the vertical precision of the observed ice thickness; Figure 6b). The impact of the ocean heat flux time resolution on ice temperature can only be estimated for the smoothed and noise-added fluxes and never exceeded 0.2 °C (not shown).

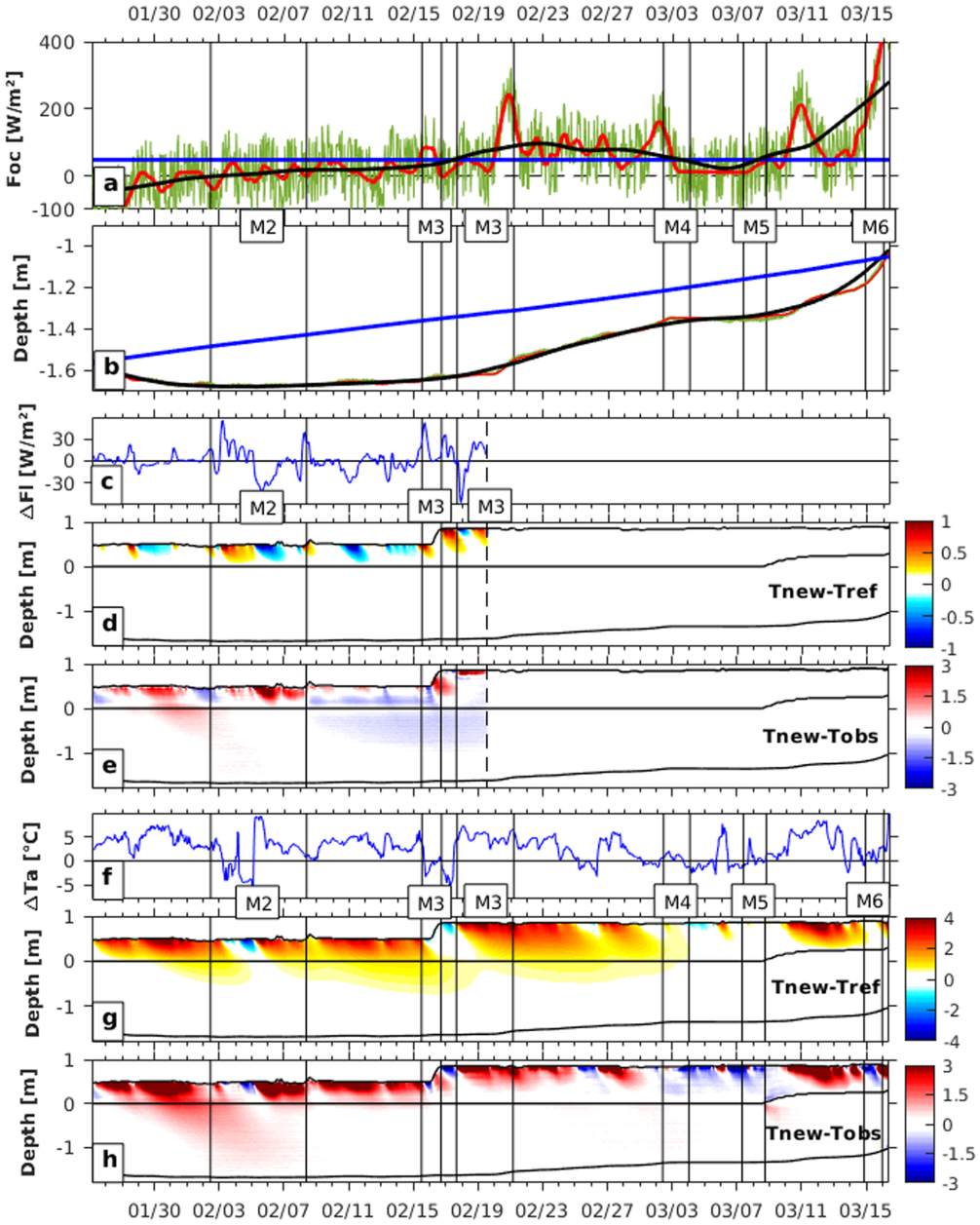

Figure 6. (a) Reference ocean heat flux (red), smoothed ocean heat flux (black), noise-added ocean heat flux (green), and constant ocean heat flux (blue). (b) Simulated ice thickness obtained with the reference (red), smoothed (black), noise added (green), and constant (blue) ocean heat flux (green). (c) Difference between RV Lance (available until 02/20) and ERA-I long-wave fluxes. (d) Temperature difference (°C) between the simulation forced with the long-wave flux from RV Lance and the reference simulation (ERA-I). (e) Temperature difference (°C) between simulation (using RV-LANCE long-wave flux) and observations. (f) Difference between ERA-I and IAOOS air temperature. (g) Temperature difference (°C) between the simulation forced with ERA_I air temperature and the reference simulation (IAOOS). (h) Temperature difference (°C) between simulation (using ERA_I air temperature) and observations. Storms are labeled M2, M3, … , M6 as described in Cohen et al. (2017).

In this particular winter case (slow ice growth followed by an intense basal ice melt), the simulated ice thickness and temperature were not very sensitive to the short timescale variations of the ocean heat flux. However, smoothing over 10 days prevented a precise representation of its variations (mostly during intense basal melt).

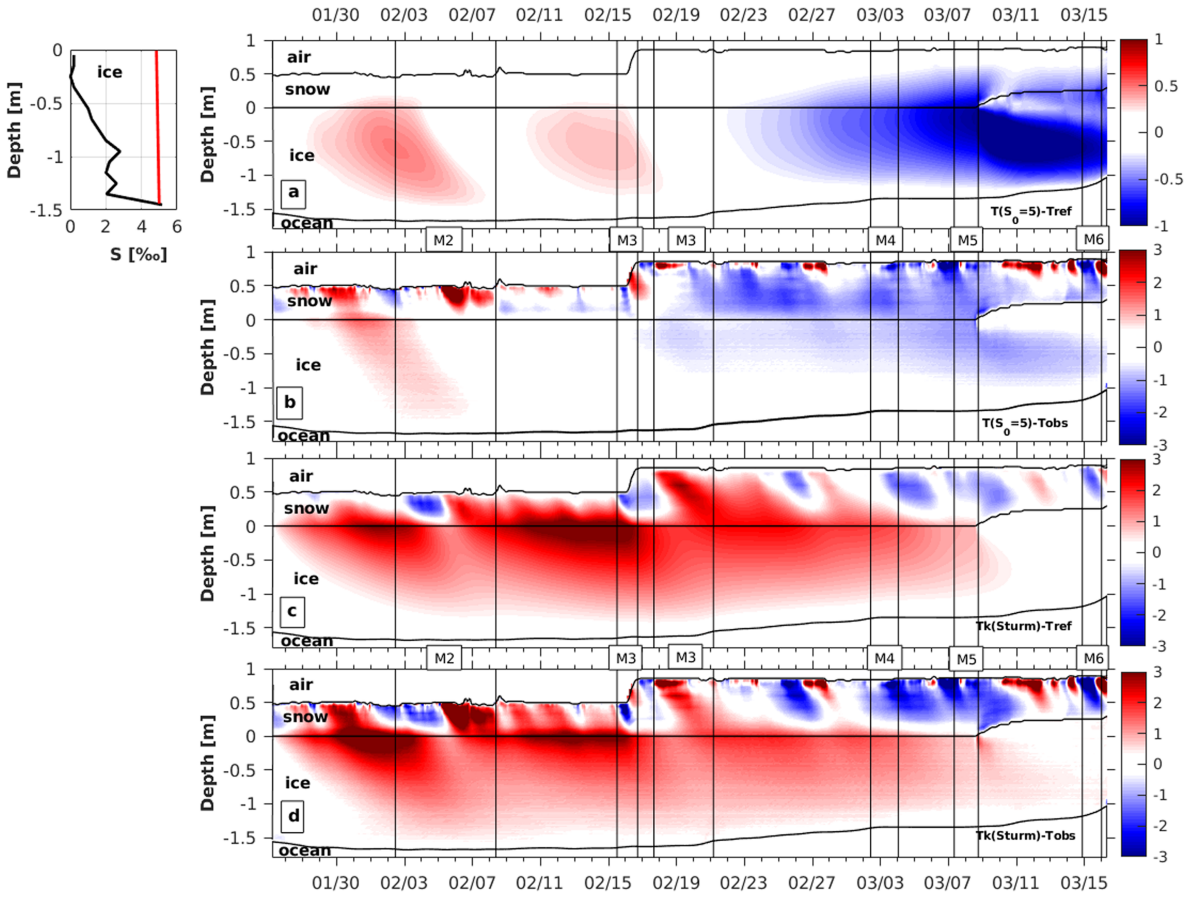

Figure 7. (a) Left: observed initial ice salinity used for the reference run (black; Granskog et al., 2017) and uniform initial salinity of 5‰. Right: temperature difference between the simulation with a uniform initial salinity of 5‰ and the reference simulation. (b) Temperature difference (°C) between simulation (initial salinity of 5‰) and observations. (c) Temperature difference between the simulation with a snow conductivity deduced from Sturm et al. (1997) and the reference one (°C). (d) Temperature difference between simulation (using Sturm et al., 1997, conductivity) and observations. Storms are labeled M2, M3, ... , M6 as described in Cohen et al. (2017).

3.2.2. ERA-I and RV-Lance Incoming Long-Wave Radiation

We compared the reference simulation (obtained using the ERA-I long-wave heat flux) to a simulation forced by the long-wave heat flux measured on the RV-Lance. The comparison only covered the first 25 days of the simulation since the RV-Lance had to relocated after 19 February. ERA-I and RV-Lance long-wave flux both have a mean value of 170 W/m^2 and a standard deviation of 50 W/m^2. The RMSD between the two series is 12 W/m^2.

Temperature differences between the two simulations varied between ±1 °C at the snow/air interface and, as expected, were strongly correlated with the flux differences (Figures 6c and 6d). Using the observed fluxes from RV-Lance slightly improved the run (Figure 6e): The RMSD between the observed and simulated snow temperature was smaller (0.92 °C) than in the reference run (1.01 °C) (Table 2). Even if using the RV-Lance long-wave flux improved the simulation, the impact remained small in the snow layer and negligible in the ice: The thick isolating snow cover (~50 cm) prevented the emergence of temperature variations in the ice. This comparison suggests that the use of ERA-I long-wave flux is reasonable in this case (thick snow cover).

3.2.3. ERA-I and IAOOS Air Temperature

We performed a simulation using ERA-I air temperature at 2 m. ERA-I air temperature was too large during cold period (up to 10 °C) and too small during warm period (up to 5 °C; Figure 6f), leading to a RMSD of 3.3 °C with the observed air temperature (Graham et al., 2016). The RMSD between the observed and simulated temperature increased to 2.0 °C for the snow and 0.26 °C for the ice (Figure 6h and Table 2). As expected, the temperature differences between the reference run and the ERA-I air temperature run were maximum at the

air/snow interface (4 °C) and decreased with depth: They did not exceed 1 °C at the snow/ice interface and 0.5 °C, approximately 50 cm below (Figure 6g).

The impact of the ERA-I air temperature was significant in the ice, even with 50 cm snow cover. It could be more important with less snow. The results show the importance of using accurate observation of the air temperature to force the model. Degrading the time resolution (12 hr moving average) of the air temperature did not modify significantly the simulation (not shown).

3.2.4. Uniform Versus Observed Initial Salinity Profile

We performed a simulation using a uniform initial ice salinity of 5‰ (Figure 7a, left). This is the common value of salinity used in sea ice models when the observed one is not available (Schmidt et al., 2004; Zhang & Rothrock, 2001). The simulation was altered, with a RMSD between the observed and simulated temperature of 1.17 °C for the snow and 0.35 °C for the ice (Figure 7b and Table 2, Run D). A larger salinity is expected to have a direct impact on the temperature, by reducing the sea ice thermal conductivity (equation (7)).

During the first period (before 19 February), the new simulation was warmer than the reference (up to 0.5 °C), as the smaller conductivity inhibited the penetration of the cold air temperature (Figure 7a). The effect of the uniform salinity on the ice temperature was reduced during storms, since the air temperature increased (M2 and M3, Figure 7a).

During the second period, the thick snow cover (≈80 cm) better insulated the sea ice from the air temperature and the uniform salinity profile had an opposite effect on the ice temperature (and snow). The temperature differences between simulation and observation were maximum when flooding occurred; the simulated ice temperature was colder than observations, by about 1 °C down to 80 cm.

3.2.5. Snow Conductivity

We used the parameterization of snow conductivity proposed by Sturm et al. (1997):

$$k\mathrm{S2} = 0.138 - 1.01\,\rho S + 3.223\,\rho S2 \text{ valid in the range } 156 < \rho S < 600\ \mathrm{kg/m^3}$$

which leads to significantly different snow conductivity: For a snow density of 390 kg/m^3, conductivity reduces from 0.43 W/m/k if computed with Abel's formula (used in the reference run) to 0.23 W/m/k.

During cold periods, as expected, the snow with the small conductivity was warmer than in the reference run: Temperature differences with the reference run increased with depth and reached a maximum at the snow-ice interface (around 3 °C; Figure 7c). The impact of the small snow conductivity was still observed 1 m below the snow-ice interface (about 1 °C). During warm episodes (e.g., 3, 16, and 26 February and 7 and 15 March), the snow (with the small conductivity) was colder than in the reference run by almost 2 °C, as the small conductivity inhibited heat penetration (Figure 7c). Just before flooding, the temperature difference at the snow ice interface was 0.5 °C. The heat flux during flooding was due to the intrusion of seawater, limiting the impact of the change in snow conductivity.

The use of Sturm et al. (1997) parameterization of snow conductivity deteriorated the simulation in snow and ice (Figure 7d and Table 2, Run E): The RMSD between the observed and simulated temperature was 1.58 °C for the snow and 0.84 °C for the ice. Using Sturm et al. (1997) equation without deteriorating the simulation would have implied to assume a snow density of 500 kg/m^3, which was not consistent with the measurements made during the N-ICE2015 campaign (Merkouriadi et al., 2017).

3.2.6. Summary of Sensitivity Studies

These sensitivity studies illustrate the effects of changes in the external forcing, the initial salinity profile, and snow conductivity on the simulated snow and sea ice: (i) A smooth ocean heat flux prevented a precise representation of the sea ice thickness variations; (ii) using ERA-I long-wave flux was reasonable since the observed RV-Lance flux improved the RMSD by only 0.09 °C (in the snow), which is the sensor resolution of the SIMBA; (iii) the ERA-I air temperature has an important bias, and the observed temperature was required to accurately simulate the snow and ice temperature; (iv) the initial ice salinity had a significant and persistent impact on the winter ice temperature, (v) the snow properties strongly impinge on the quality of the simulation and a precise estimation of the snow density is necessary.

For SIMBA_h, a constant snow density of 390 kg/m^3 was sufficient to provide a good agreement between the observed and simulated snow and ice temperature evolution.

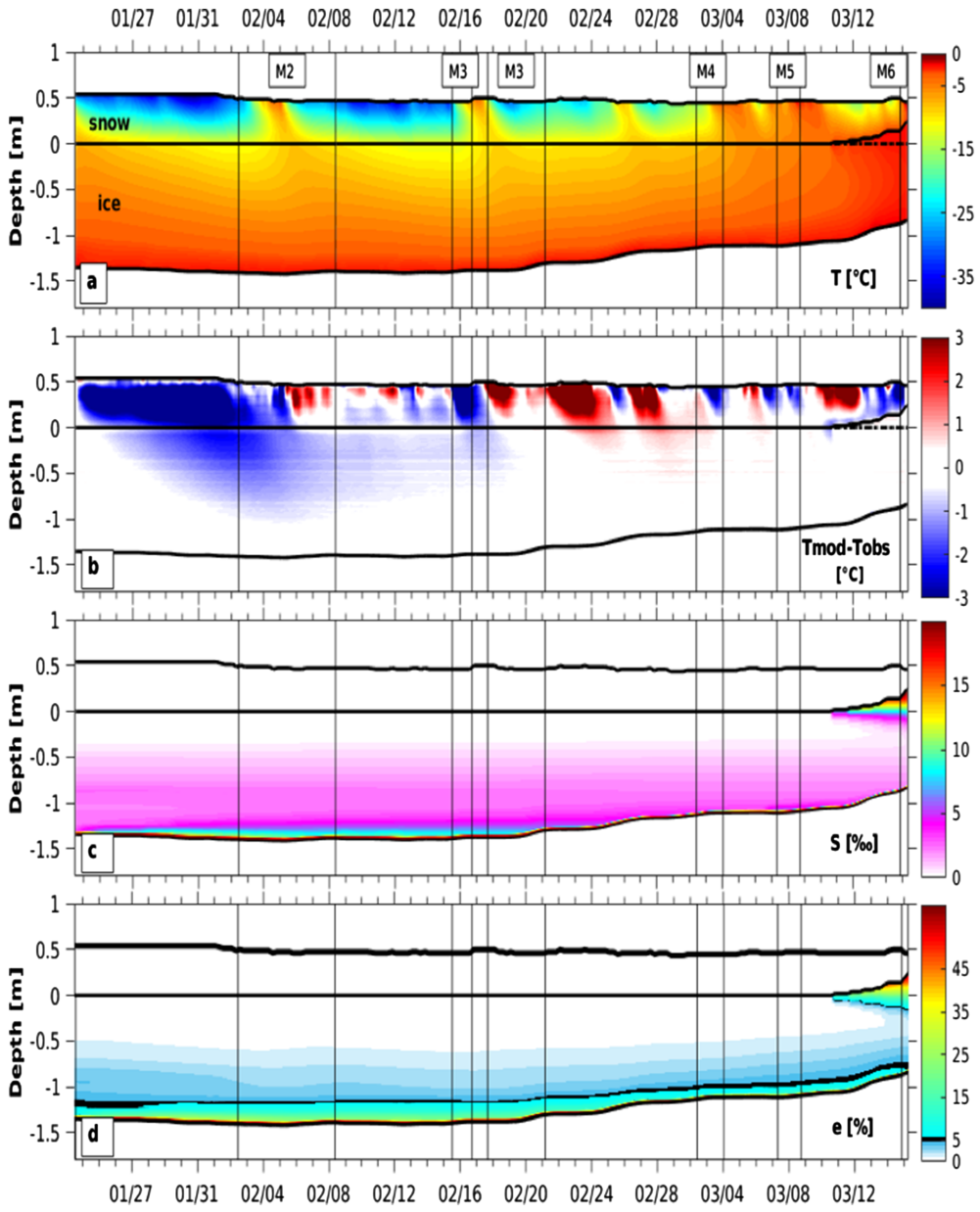

Figure 8. Reference run for SIMBA_a. (a) Simulated temperature as a function of time in snow and ice. (b) Temperature differences between simulation and observations. Model outputs are interpolated to the vertical resolution of the data (2 cm). (c) Simulated ice salinity as a function of time. (d) Simulated ice brine fraction as a function of time. The black isoline corresponds to the 5% brine fraction. On all the panels, black lines correspond to the air/snow interface, the lower limit of the snow layer, and ice/ocean interface. Storms are labeled M2, M3, ... , M6 as described in Cohen et al. (2017).

4. Simulation Along SIMBA_a Drift

A first simulation of SIMBA_a time series was performed, using the same forcing terms and parameters as for SIMBA_h (in particular, the same snow density of 390 kg/m^3) and led to a simulation with a RMSD between the observed and simulated temperature of 2.50 °C in the snow and 0.45 °C in the ice.

4.1. Snow Density Adjustment

The two SIMBA buoys featured distinct diffusivity proxy values in the snow with larger values at the SIMBA_a site (1.8 on average) than at SIMBA_h (1.7) (Figures 1d and 1f). As a larger value of the diffusivity proxy is associated with a smaller conductivity and consequently a smaller density, this difference in proxy suggests that the snow density at SIMBA_a was smaller than at SIMBA_h.

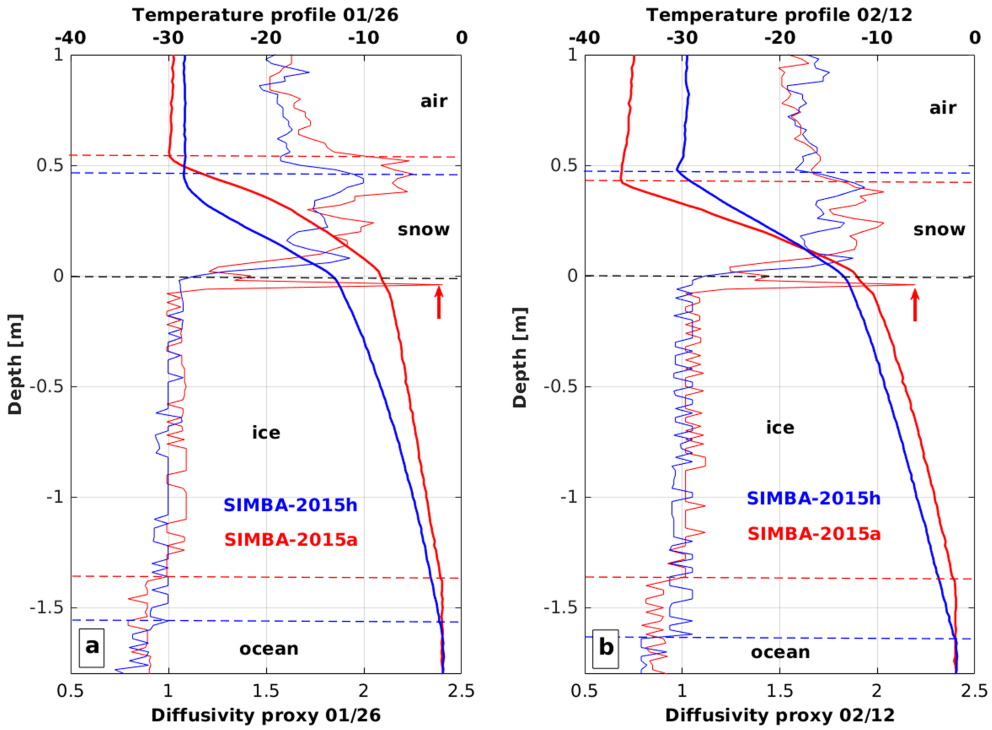

Figure 9. Observed diffusivity proxy (thin) and temperature profiles (bold) for SIMBA_h (blue) and SIMBA_a (red) on (a) 26 January and (b) 12 February. The air/snow and ice/ocean interface are represented by dashed lines. Zero is the snow/ice interface. The red arrow points at the anomalous layer (see appendix A).

A simulation with a snow density of 370 kg/m^3 (a conductivity of 0.39 W/K/m) reduced the RMSD between the observed and simulated temperature profiles to 2.49 °C in the snow and 0.40 °C in the ice (Figures 8a and 8b). The simulated snow temperature was still 2 to 5 °C colder than the observations during the first ten days (Figure 8b). A closer look at SIMBA_a diffusivity proxy profiles (Figure 9a) showed the existence of two layers of snow with well-differentiated diffusivity proxy values: 2.2 on average in the upper 20 cm of snow and 1.8 in the lower 30 cm. These differences in diffusivity proxy led to a change of slope in the observed snow temperature profile (Figure 9a). The simulated temperature profiles have a constant slope if conductivity and density are the same in the five snow layers (Figure 10b).

We adjusted the snow density of the upper two layers to 240 kg/m^3 (corresponding to a snow conductivity of 0.16 W/m/K) until 1 February, to account for the presence of a lighter snow layer that was later blown away at the beginning of storm M2 (Figure 1f). In the lower three layers, we kept a density value of 370 kg/m^3 (snow conductivity: 0.39 W/m/K). The simulated snow temperature profiles were much closer to the observations (Figure 10b) with the RMSD dropping from 2.49 to 2.14 °C (Figure 10c).

4.2. Simulated Sea Ice

Adjusting the snow density (upper two layers at 240 kg/m^3 and lower three layers at 370 kg/m^3) improved the simulated ice temperature before 1 February, with a RMSD between observed and simulated ice temperature dropping from 0.40 to 0.35 °C (Figure 10c). Large temperature differences with the measurement located a few centimeters (5 cm) below the snow/ice interface (Figure 10c) occurred in a thin anomalous layer (about 2 cm) with a diffusivity proxy around 2.4, a value much larger than in the ice (1.1; Figures 9 and 1f). This anomalous layer, which persisted until the flooding event (on 10 March), had an insulating effect, partly limiting heat diffusion through the ice (Figures 1f and 9), which led to a thicker simulated ice (Figure 10c). This spurious layer was probably an artifact of the SIMBA_a deployment protocol as explained in the appendix.

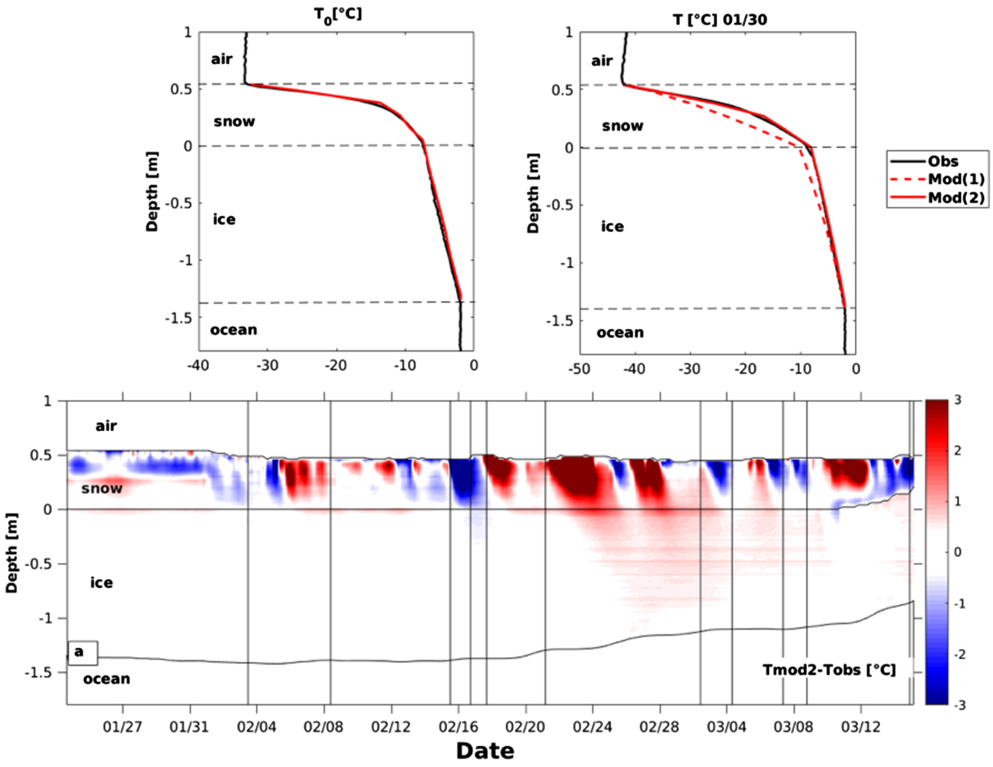

Figure 10. (a) Observed (black) and simulated (red) initial temperature profile for SIMBA_a. (b) Observed (black) and simulated temperature profile (mod1: constant snow density is 370 kg/m^3; mod2: the snow density of the first two layers is 240 kg/m^3 until 1 February). Dashed black lines represent the air/snow, snow/ice, and ice/ocean interfaces. (c) Temperature differences between simulation (mod2) and observations. Model outputs are interpolated to the vertical resolution of the data (2 cm).

5. Flooding and Snow Ice Formation

At the end of the record, the heavily snow-loaded floes lost buoyancy due to basal melt. Storm M5 induced the breakup of the floes, and the snow/ice interface sank below the sea level on 8 March for SIMBA_h and 10 March for SIMBA_a (Figure 11). The immersed snow layer was flooded with seawater (around −1.8 °C), inducing a rapid increase of temperature, salinity, and brine fraction (Figures 5 and 8). The mixture of snow and salt water formed a slush layer warmer than the surrounding snow and ice and slowly solidified into snow ice (Provost et al., 2017).

5.1. Simulated Temperature in the Slush and Ice During Flooding

Flooding was more gradual at SIMBA_a than at SIMBA_h. A 20 cm thick slush layer was formed in 2 days at SIMBA_h (30 cm at the end of the record, after 7 days) and an only 8 cm thick layer was formed at SIMBA_a (21 cm at the end of the record, after 6 days).

The flooding led to an increase in the observed temperature at the snow/ice interface ($z = 0$) from −5.8 to about −2.4 °C in a few hours for SIMBA_h (Figure 11d) and from −5 to −2.8 °C in two days for SIMBA_a (Figure 11a). The slush layer was slightly colder at SIMBA_a, due to both the more gradual inflow of seawater and the thinner snow layer, which provided less thermal insulation from the cold atmosphere. The heat release associated with the flooding led to a temperature increase of about 3 °C down to 0.50 m in the ice (Figures 11a and 11d).

The simulated temperature in slush and ice was in good agreement with the observations (Figures 11b and 11e). Once the flooding began, the temperature at the snow/ice interface increased from −5.9 to −1.9 °C for SIMBA_h (Figures 11e and 12i; from −4.1 to −2.5 °C for SIMBA_a, Figure 11b). In the two cases, the temperature differences between simulations and observations never exceeded 0.4 °C in the slush layer and underlying ice (Figures 11c and 11f).

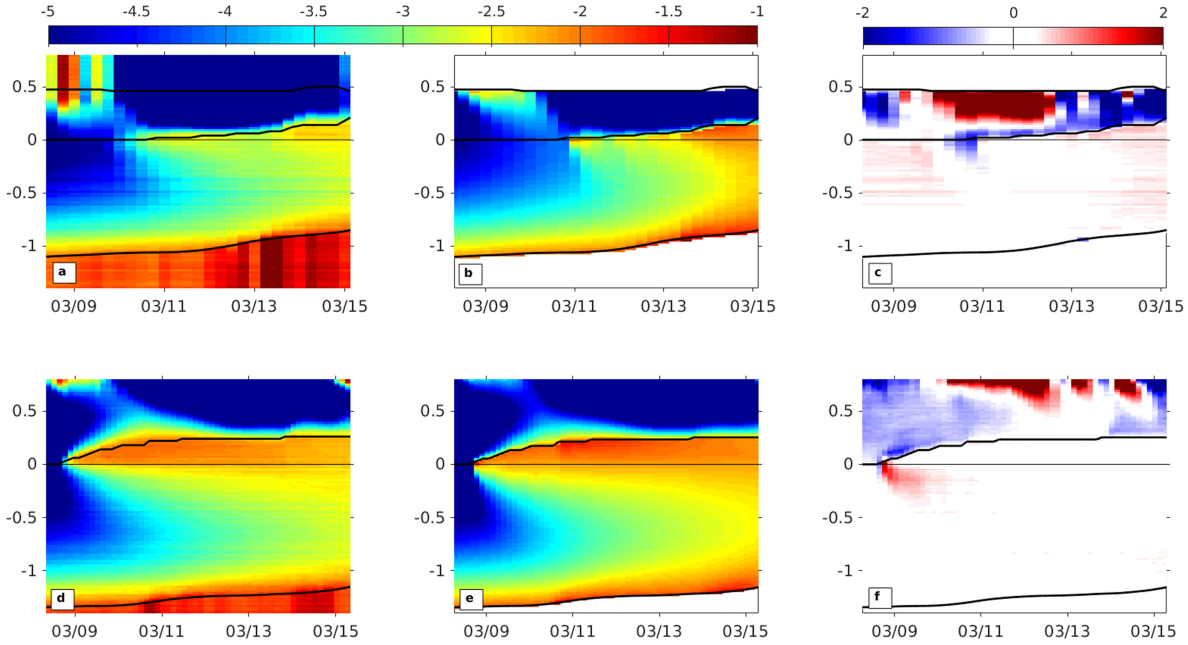

Figure 11. (a) Close-up of observed temperature during the period of flooding for SIMBA_a. (b) Close-up of simulated temperature during the period of flooding for SIMBA_a. Outputs have been interpolated to the vertical resolution of the data (2 cm). (c) Temperature differences between simulation and observations for SIMBA_a. (d) Same as (a) for SIMBA_h. (e) Same as (b) for SIMBA_h. (f) Same as (c) for SIMBA_h. Black lines correspond to the air/snow interface, the lower limit of the snow layer, and ice/ocean interface.

5.2. Impact of Flooding on Simulated Salinity and Brine Fraction

When seawater invaded the space previously occupied by air in the snow, the simulated salinity increased from 0 to a maximum of 19‰ (Figures 12a and 12d). We now focus on the simulated evolution of salinity, solid fraction, and temperature at SIMBA_h.

Flooding occurred in six steps as the snow/ice interface progressively sank (Figure 12d). At each step, salinity and temperature were maximum at the top of the slush, where additional water ($T > -2$ °C) flooded the overlying snow (Figures 12g and 12i). The solid fraction in the snow was 42% ($\Phi_i = \frac{\rho_{\text{snow}}}{\rho_{\text{ice}}} = 390/917$) before flooding and increased up to 80% at the base of the slush and 55% at the top at the end of the simulation (Figures 12e and 12h). Salinity increased from 0‰ to 8‰ at the base of the slush layer and 17‰ at the top, at the end of the simulation (Figures 12d and 12g).

Below the initial snow/ice interface $z = 0$, the upper ice warming (Figure 12i) led to an increase of porosity down to 40 cm. The solid fraction dropped from 100% to less than 95% in the upper 20 cm (Figure 12h), leading an increase of salinity from 0‰ to 3‰ (Figure 12g).

5.3. Snow Ice Formation

Provost et al. (2017) estimated the amount of solidified slush (snow ice) at the end of the record. Assuming that the mass fractions of snow and water in snow ice were 2/3 and 1/3, they found a corresponding snow ice thickness of 8 cm for SIMBA_h and 6 cm for SIMBA_a.

The simulated solid fraction provides the amount of formed snow ice. The initial solid fraction in the slush layer was 42% for SIMBA_h (40% for SIMBA_a). At the end of the simulation, the average of the solid fraction over the slush layer was 60% for SIMBA_h (58% for SIMBA_2015a). The corresponding thickness of the ice fraction in the flooded snow ($h(t)$, gray) and the total ice fraction in the slush layer ($H(t)$, blue) were computed using the following relations (Figures 12c and 12f)

$$h(t) = \Phi_i * h_s(t) \text{ and } H(t) = \frac{S_f(t)}{100} * h_s(t)$$

where $h_s(t)$ is the thickness of the flooded snow and $S_f(t)$ is the average solid fraction of the slush layer

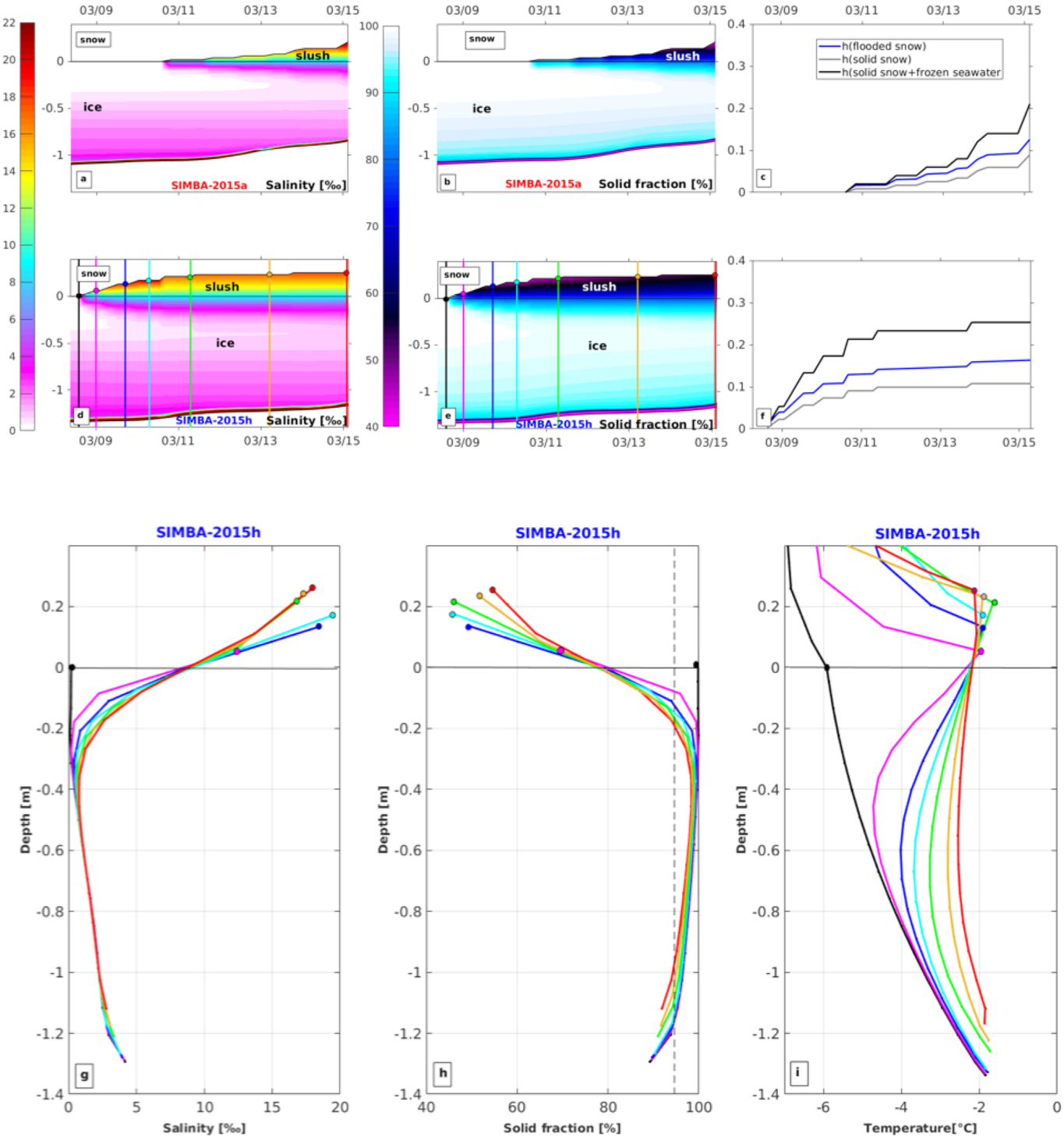

Figure 12. (a) Close-up of simulated ice and slush salinity during the period of flooding for SIMBA_a. (b) Close-up of simulated ice and slush solid fraction during the period of flooding for SIMBA_a. (c) Thickness of the flooded snow (black), the solid snow (gray), and the solid snow added to the frozen seawater (blue). (d) Same as (a) for SIMBA_h. (e) Same as (b) for SIMBA_h. The black dot corresponds to the snow/ice interface and colored dots to the snow/slush interface at each step of flooding. (f) Same as (c) for SIMBA_h. (g) Simulated salinity profile at each step of flooding for SIMBA_h. (h) Simulated solid fraction profile at each step of flooding for SIMBA_h (i) Simulated temperature profile at each step of flooding. In panels g, h, and i the initial profile just before flooding is in black, and the color code for the subsequent profiles is the same as in panel d.

(Figure 12h). The estimated amount of formed snow ice, $h_{si}(t) = H(t) - h(t)$, is 5.5 cm at SIMBA_2015h (4 cm at SIMBA_2015a; Figures 12c and 12f). These values are in good agreement with the values obtained by Provost et al. (2017).

6. Summary and Perspectives

We revisited the winter SIMBA data provided by the N-ICE2015 campaign, north of Svalbard, using the one-dimensional model LIM1D (Vancoppenolle et al., 2010).

Using five layers of snow instead of one was essential to represent the nonlinear temperature profiles in the snow, in particular during storms when the temperature vertical gradients changed sign. A better representation of the snow temperature profile significantly improves the temperature at the snow ice interface. A multilayer snow system also provided the opportunity to adjust the snow density, since a constant value was not always sufficient to provide a good agreement between the observed and simulated snow and ice temperature profiles.

The reference experiment (SIMBA_h, Figures 5a and 5b) was in good agreement with the observations; the RMSD between observed and simulated temperature profiles was 1.06 °C for the snow and 0.19 °C for the ice. Several sensitivity experiments emphasized the following points: (i) Simulated ice thickness and temperature profiles were not very sensitive to the short timescale (<10 days) variations of the ocean flux; (ii) ERA-I long-wave fluxes were reasonable; (iii) the observed air temperature was necessary because of the warm bias in ERA-I temperature; (iv) a constant initial ice salinity profile of 5‰ (that is typically used in models) introduced an error which was maximum during intense basal melt.

A constant snow density layer is a commonly used simplification. However, snow density varies and is strongly affected by weather conditions (snowfall, wind, and air temperature; e.g., Merkouriadi et al., 2017, Lecomte et al., 2011). Using a constant snow density (390 kg/m^3) led to a satisfactory simulation of SIMBA_h temperature profiles evolution and to poor results for SIMBA_a. Even if the two buoys remained within a distance of 20 km, the snow thicknesses and characteristics recorded by the SIMBAs differ significantly. The introduction of a lighter snow in the lower hree3 layers (370 kg/m^3) and an even lighter snow in the upper two layers (240 kg/m^3 until this lighter snow layer was blown away at the beginning of storm M2) greatly improved the simulation at SIMBA-a. The observed and simulated temperature profiles were jointly used to estimate the snow density (and conductivity). This is a preliminary work, and, in parallel, laboratory studies are ongoing to determine if a (quantitative) relationship between the observed diffusivity proxy and the snow density can be established.

By specifying the observed lower limit of the snow, the flooding episode was simulated and the formation of snow ice quantified. Since the agreement between the observed and simulated temperature profiles was good during the flooding period (temperature difference does not exceed 0.4 °C), the salinity and brine volume computed in the numerical experiment were reliable. The amount of snow ice formed was investigated through the simulated solid fraction. During the flooding event, the simulation led to the formation of approximately 5.5 cm for SIMBA_h (4,0 cm for SIMBA_a). These values are in good agreement with the estimation made by Provost et al. (2017) of 8 cm for SIMBA_h (6 cm for SIMBA_a).

Revisiting winter Arctic ice mass balance observations with a 1-D model validated the interpretations made from the observations (interfaces and ocean heat flux) and provided additional information about the snow (density) and ice (salinity and brine volume). This was useful to more accurately interpret the physical processes at stake in the air/snow/ice/ocean coupled system, such as flooding and snow ice formation. Simulations also pointed out to artefacts due to deployment protocol (see appendix A).

Appendix: Impact of the Deployment Protocol on SIMBA Observations A

Modeling of SIMBA_a temperature evolution revealed an anomalous value of the diffusivity proxy below the ice-snow interface corresponding to a thin layer with a large insulating effect that impacted temperature evolution (section 4.2). To understand the origin of this thin anomalous layer, we examined the very first stages of refreezing after deployment.

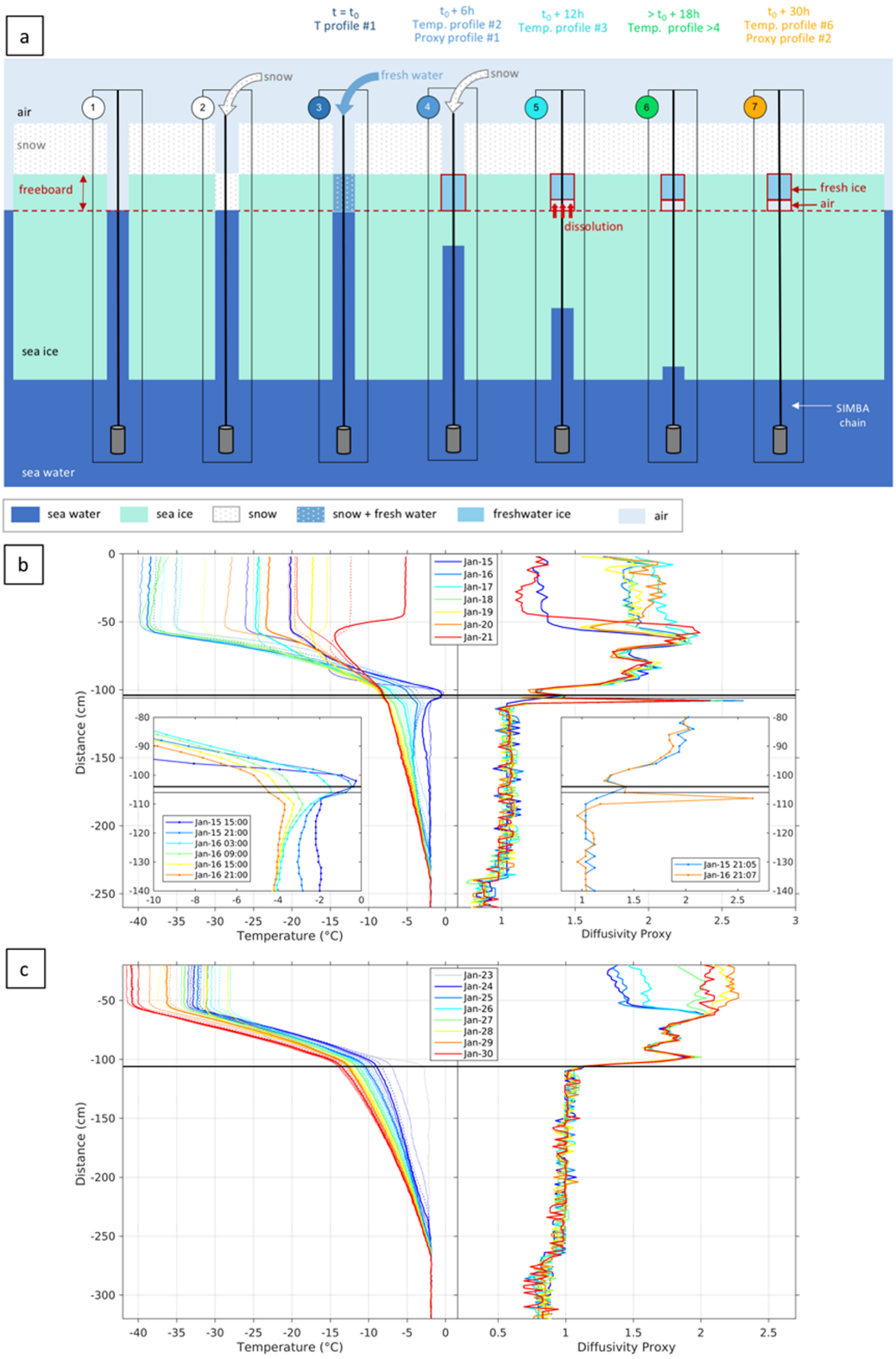

Figure A1. (a) Schematics of the deployment protocol for SIMBA_a. (b) Left: First temperature profiles for SIMBA_a (subsampled once a day) during the first week after deployment; insert: close-up of all the temperature profiles near the ice-snow interface (every 6 hr) on the first two days (every 6 hr). Right: First diffusivity proxy profiles for SIMBA_a (during the first week, once a day); insert close up on the proxy profiles near the snow-ice interface during the first two days. (c) Left: First temperature profiles for SIMBA_h (subsampled once a day) during the first week. Right: first diffusivity proxy profiles for SIMBA-h (every 24 hr).

SIMBA-a was deployed on 15 January 2015 during polar night. Air temperature was around −26 °C (Figure 1b). The SIMBA chain was installed at the center of a 5 cm diameter hole through the snow and ice (Figure 1, step 1). A weight maintained the line straight. Once the chain was in place, snow was put above the water to fill the hole up to the snow/ice interface (Figure 1a, step 2) and freshwater was poured over the snow up to the snow/ice interface (Figure 1a, step 3). The mixture of freshwater and snow rapidly solidified into freshwater ice, and snow was added to restore the original snow level (Figure 1a, step 4). The initial temperature profiles from 15 January show values close to 0 °C at a distance of 100 to 108 cm (from the top of the chain), corresponding to the added freshwater. The initial diffusivity profile (15 January) does not show any spurious spike (dark blue profile in Figure 1b). As seawater started to freeze gradually from the top (Figure 1b, light blue profiles), brines were rejected into the water column below and in the freshwater ice above (Figure 1a, step 5). The second diffusivity profile (16 January in orange) shows a spike with values typical of air at a distance of 108 cm. This spike is interpreted as follows: The salt rejected by refreezing seawater may have induced the partial dissolution of the freshwater ice above it, leading to an anomalous layer with air (Figure 1, step 6, 7). The spike in the proxy profile corresponding to this insulating layer, which limited the heat diffusion through the ice, persisted until the flooding event (on 10 March). This interpretation in terms of dissolution of the fresh ice above refreezing seawater results from the absence of a spike in the first proxy profile (6 hr after freshwater was poured) and the emergence and persistence of a huge spike after the second proxy profile (24 hr later; (Figure 1a, step 5).

The temperature profiles at the beginning of the time series provide information on how the different media refroze or behave around the chain (Figure 1b). The seawater in the hole gradually froze from the top to the bottom and was entirely frozen 2 days after the deployment. In 6 hr, 50 cm of seawater has frozen in the hole. The large values of the diffusivity proxy highlight the insulating layer, just below the snow ice interface (Figure 1b).

SIMBA_h was deployed on 23 January 2015. Air temperature was about −33 °C (Figure 1c). The deployment protocol was simpler: Snow was simply added on the refreezing seawater up to the floe snow surface. There was no attempt to restore the ice layer above the 2 cm initial freeboard. Therefore, the measured snow ice interface was at most 2 cm below the unperturbed one. The first temperature profiles showed that more than a meter of water in the hole was refrozen after only 3 hr (Figure 1c). Diffusivity proxy values simply dropped from ice values to snow values at the new snow/ice interface (−2 cm).

Acknowledgments
We thank the crew of RV Lance and scientists who participated to the N-ICE 2015 campaign. We acknowledge support from the ANR EQUIPEX IAOOS project, through ANR-10-EQPX-32-01 grant. Parameters from the ERA-Interim reanalysis were obtained from ECMWF. We thank Clément Rousset and Martin Vancoppenolle for helping us with the model LIM1D and constructive discussions. We thank two anonymous reviewers for their comments that helped improve the manuscript. We thank Elisabeth Boles for English proofreading of the manuscript. Sarah Gani benefits from a PhD scholarship from Sorbonne Université, Paris (Ecole Doctorale 129). SIMBA data are available at Sennéchael et al. (2015) https://doi.org/10.17882/59624 and Itkin et al. (2015) https://doi.org/10.21334/npolar.2015.6ed9a8ca and interfaces and ocean fluxes at Sennéchael and Provost (2015) https://doi.org/10.17882/59709.

References

Andreas, E. L. (1987). A theory for the scalar roughness and the scalar transfer coefficients over snow and sea ice. *Boundary Layer Meteorology*, *38*, 159–184. https://doi.org/10.1007/BF00121562

Bitz, C. M., & Lipscomb, W. H. (1999). An energy conserving thermodynamic model of sea ice. *Journal of Geophysical Research*, *104*, 15,669–15,677. https://doi.org/10.1029/1999JC900100

Cohen, L., Hudson, S. R., Walden, V. P., Graham, R., & Granskog, M. A. (2017). Meteorological conditions in a thinner Arctic sea ice regime from winter to summer during the Norwegian Young Sea Ice expedition (N-ICE2015). *Journal of Geophysical Research: Atmospheres*, *122*, 7235–7259. https://doi.org/10.1002/2016JD026034

Dee, D. P., Uppala, S. M., Simmons, A. J., Berrisford, P., Poli, P., Kobayashi, S., et al. (2011). The ERA-Interim reanalysis: Configuration and performance of the data assimilation system. *Quartely Journal of the Royal Meteorological Society*, *137*(656), 553–597. https://doi.org/10.1002/qj.828

Duarte, P., Meyer, A., Olsen, L. M., Kauko, H. M., Assmy, P., Rösel, A., et al. (2017). Sea ice thermohaline dynamics and biogeochemistry in the Arctic Ocean: Empirical and model results. *Journal of Geophysical Research: Biogeosciences*, *122*, 1632–1654. https://doi.org/10.1002/2016JG003660

Dupont, F., Higginson, S., Bourdallé-Badie, R., Lu, Y., Roy, F., Smith, G. C., et al. (2015). A high-resolution ocean and sea-ice modelling system for the Arctic and North Atlantic Oceans. *Geoscientific Model Development*, *8*, 1577–1594. https://doi.org/10.5194/gmd-8-1577-2015

Golden, K. M., Ackley, S. F., & Lytle, V. I. (1998). The percolation phase transition in sea ice. *Science*, *282*, 2238–2241. https://doi.org/10.1126/science.282.5397.2238

Graham, R. M., Rinke, A., Cohen, L., Hudson, S. R., Walden, V. P., Granskog, M. A., et al. (2016). A comparison of the two Arctic atmospheric winter states observed during N-ICE2015 and SHEBA. *Journal of Geophysical Research: Atmospheres*, *22*, 5716–5737. https://doi.org/10.1002/2016JD025475

Granskog, M., Assmy, P., Gerland, S., Spreen, G., Steen, H., & Smedsrud, L. H. (2016). Arctic research on thin ice—Consequences of Arctic sea ice loss. *Eos, Transactions American Geophysical Union*, *97*(5), 22–26. https://doi.org/10.1029/2016EO044097

Granskog, M. A., Rösel, A., Dodd, P. A., Divine, D., Gerland, S., Martma, T., & Leng, M. J. (2017). Snow contribution to first-year and second-year Arctic sea ice mass balance north of Svalbard. *Journal of Geophysical Research: Oceans*, *122*, 2539–2549. https://doi.org/10.1002/2016JC012398

Hudson, S. and L. Cohen (2016), N-ICE2015 surface meteorology v1. Norwegian Polar Institute (Tromsø, Norway), https://data.npolar.no/dataset/056a61d1-d089-483a-a256-081de4f3308d.

Huwald, H., Tremblay, L.-B., & Blatter, H. (2005). A multilayer sigma-coordinate thermodynamic sea ice model: Validation against Surface Heat Budget of the Arctic Ocean (SHEBA)/Sea Ice Model Intercomparison Project Part 2 (SIMIP2) data. *Journal of Geophysical Research*, *110*, C05010. https://doi.org/10.1029/2004JC002328

Itkin, P., Spreen, G., Cheng, B., Doble, M., Gerland, S., Granskog, M. A., Helgeland, C. (2015). N-ICE2015 buoy data. Norwegian Polar Institute, https://doi.org/10.21334/npolar.2015.6ed9a8ca

Jackson, K., Wilkinson, J., Maksym, T., Meldrum,D., Beckers, J., Haas, C., & McKenzie, D. (2013). A novel and low-cost sea-ice mass balance buoy,*Journal of Atmospheric and OceanicTechnology*, *30*, 2676–2688. https://doi.org/10.1175/JTECH-D-13-00058.1

Jutras, M., Vancoppenolle, M., Lourenço, A., Vivier, F., Carnat, G., & Madec, G. (2016). Thermodynamics of slush and snow–ice formation in the Antarctic sea ice zone. *Deep Sea Research Part II*, *131*, 75–83. https://doi.org/10.1016/j.dsr2.2016.03.008.hal-01303755

Kim, J. G., Hunke, E. C., & Lipscomb, W. L. (2006). A sensitivity analysis and parameter tuning scheme for global sea-ice modeling. *Ocean Modelling.*, *14*, 61–80. https://doi.org/10.1016/j.ocemod.2006.03.003

Koenig, Z., Provost, C., Villacieros-Robineau, N., Sennéchael, N., & Meyer, A. (2016). Winter ocean-ice interactions under thin sea ice observed by IAOOS platforms during N-ICE 2015: Salty surface mixed layer and active basal melt. *Journal of Geophysical Research: Oceans*, *121*, 7898–7916. https://doi.org/10.1002/2016JC012195

Lecomte, O., Fichefet, T., Vancoppenolle, M., & Nicolaus, M. (2011). A new snow thermodynamic scheme for large-scale sea-ice models. *Annals of Glaciology*, *52*(57), 337–346. https://doi.org/10.3189/172756411795931453

Lindsay, R., & Schweiger, A. (2015). Arctic sea ice thickness loss determined using subsurface, aircraft, and satellite observations. *The Cryosphere*, *9*, 269–283. https://doi.org/10.5194/tc-9-269-2015

Maykut, G. A. (1978). Energy exchange over young sea ice in the central Arctic. *Journal of Geophysical Research*, *83*(C7), 3646–3658. https://doi.org/10.1029/JC083iC07p03646

Merkouriadi, I., Gallet, J.-C., Graham, R. M., Liston, G. E., Polashenski, C., Rösel, A., & Gerland, S. (2017). Winter snow conditions on Arctic sea ice north of Svalbard during the Norwegian young sea ICE (N-ICE2015) expedition. *Journal of Geophysical Research: Atmospheres*, *122*, 10,837–10,854. https://doi.org/10.1002/2017JD026753

Overland, J. E., & Wang, M. (2013). When will the summer Arctic be nearly sea ice free? *Geophysical Research Letters*, *40*, 2097–2101. https://doi.org/10.1002/grl.50316

Persson, P., Fairall, C., Andreas, E., Guest, P., & Perovich, D. (2002). Measurements near the Atmospheric Surface Flux Group tower at SHEBA: Near-surface conditions and surface energy budget. *Journal of Geophysical Research*, *107*(C10), 8045. https://doi.org/10.1029/2000JC000705

Pringle, D. J., Eicken, H., Trodahl, H. J., & Backstrom, L. G. E. (2007). Thermal conductivity of Landfast Antarctic and Arctic sea ice. *Journal of Geophysical Research*, *112*, C04017. https://doi.org/10.1029/2006JC003641

Provost, C., Sennéchael, N., Miguet, J., Itkin, P., Rösel, A., Koenig, Z., et al. (2017). Observations of flooding and snow ice formation in a thinner Arctic sea ice regime during the N-ICE2015 campaign: Influence of basal ice melt and storms. *Journal of Geophysical Research: Oceans*, *122*, 7115–7134. https://doi.org/10.1002/2016JC012011

Schmidt, G. A., Bitz, C. M., Mikolajewicz, U., & Tremblay, L.-B. (2004). Ice-ocean boundary conditions for coupled models. *Ocean Model*, *7*, 59–74. https://doi.org/10.1016/S1463-5003(03)00030-1

Sennéchael N., Provost C. (2015), Interfaces and ocean heat flux derived from SIMBA_2015a and SIMBA_2015f data during N-ICE campaign in winter 2015. SEANOE. https://doi.org/10.17882/59709

Sennéchael N., Provost C., Villacieros-Robineau N., Calzas M., Guillot A., Savy J.-P., et al. (2015), IAOOS winter SIMBA data during N-ICE 2015 North of Svalbard. SEANOE. https://doi.org/10.17882/59624.

Spreen, G., Kwok, R., & Menemenlis, D. (2011). Trends in Arctic sea ice drift and role of wind forcing: 1992-2009. *Geophysical Research Letters*, *38*, L19501. https://doi.org/10.1029/2011GL048970

Sturm, M., Holmgren, J., König, M., & Morris, K. (1997). The thermal conductivity of seasonal snow. *Journal of Glaciology*, *43*(143), 26–41. https://doi.org/10.3189/S0022143000002781

Urrego-Blanco, J. R., Hunke, E. C., & Urban, N. (2016). Uncertainty quantification and global sensitivity analysis of the Los Alamos sea ice model. *Journal of Geophysical Research: Oceans*, *112*, 2709–2732. https://doi.org/10.1002/2015JC011558

Vancoppenolle, M., Fichefet, T., & Goosse, H. (2008). Simulating the mass balance and salinity of Arctic and Antarctic sea ice. 2: Importance of sea ice salinity variations. *Ocean Modelling*, *27*(1-2), 54–69. https://doi.org/10.1016/j.ocemod.2008.11.003

Vancoppenolle, M., Goosse, H., de Montety, A., Fichefet, T., Tremblay, B., & Tison, J.-L. (2010). Modeling brine and nutrient dynamics in Antarctic sea ice: The case of dissolved silica. *Journal of Geophysical Research*, *115*, C02005. https://doi.org/10.1029/2009JC005369

Vancoppenolle, M., & Tedesco, L. (2017). *An introduction to sea ice, chap. 20 Numerical models of sea ice biogeochemistry*, (pp. 492–515). Wiley. https://lccn.loc.gov/2016031586

Vihma, T., Pirazzini, R., Fer, I., Renfrew, I. A., Sedlar, J., Tjernström, M., et al. (2014). Advances in understanding and parameterization of small-scale physical processes in the marine Arctic climate system: A review. *Atmospheric Chemistry and Physics*, *14*, 9403–9450. https://doi.org/10.5194/acp-14-9403-2014

Zhang, J., & Rothrock, D. A. (2001). A thickness and enthalpy distribution sea-ice model. *Journal of Physical Oceanography*, *31*, 2986–3001. https://doi.org/10.1175/1520-0485(2001)031<2986:ATAEDS>2.0.CO;2

Estimation de la conductivité de la neige et de flux latéraux dans la glace de mer à partir d'observations de température

Sommaire

4.1 Résumé

Dans ce second article - consacré uniquement à l'analyse d'observations - nous étudions les données collectées par quatre SIMBAs qui ont dérivé pendant 3 à 9 mois avec la banquise Arctique, à partir de Septembre 2015. A partir de profils de température et de "température chauffée" (établie comme un proxy de la conductivité thermique plutôt que de la diffusivité), il est possible non seulement d'estimer le degré de stratification du manteau neigeux mais aussi de déterminer quantitativement la conductivité (et la densité) de chacune des couches le constituant. Le déploiement des SIMBAs induit des perturbations inévitables du milieu. Dans le trou foré dans la glace pour y introduire la chaîne IMB, de la neige tassée/mouillée a été ajoutée entre le niveau de l'eau et l'interface air/glace (franc bord). La conductivité/densité de cette couche correspondant au franc bord (jusqu'à 25 cm dans cette étude) a également été estimée (jusqu'à $650 kg/m^3$). Une première relation entre la "température chauffée" mesurée et la conductivité de la neige est donnée dans ce chapitre. Le calcul subséquent de la densité dépend de la relation entre conductivité et densité que l'on choisit.

La congélation complète de l'eau de mer dans le trou de déploiement a duré plus de deux mois et s'est faite du haut vers le bas, en raison du transfert de chaleur vertical vers l'atmosphère, et horizontalement, en raison du transfert de chaleur latéral venant de la glace de mer environnante. Ces flux de chaleur latéraux sont très mal connus. Nous proposons ici une méthode de calcul de la densité de flux latéral, effectuée à partir de l'analyse des profils de température dans la glace et la cinétique de congélation de l'eau de mer dans le trou de déploiement.

Ce chapitre est constitué d'un article en voie de soumission dans le *Journal of Geophysical Research.*

Estimating snow stratification, snow conductivity, and sea ice lateral heat flux from temperature profiles provided by ice mass balance instruments.
Part I: analysis of Arctic observations.

S Gani, J. Sirven, N. Sennéchael, and C. Provost.

IPSL/LOCEAN/UPMC/CNRS/IRD/MNHN

Sorbonne Université, Paris, France

Key points :

- Sea ice mass balance instruments provide information on the snow cover stratification.

- The conductivity and density of each snow layer is estimated from observed temperature profiles.

- Sea ice lateral heat fluxes, essential to the refreezing of the deployment holes, are evaluated.

Abstract

Four buoys equipped with ice mass balance instruments were deployed near the North Pole in September 2015, and drifted with the Arctic ice pack for a period ranging from 3 to 9 months. The ice mass balance instruments measured high-resolution temperature and heated temperature profiles in air, snow, sea ice, and ocean. These profiles have been used to determine the evolution of snow depth and ice thickness. A new method to estimate the stratification, conductivity, and density of the snow layers along the trajectory of the buoys has been developed. The obtained densities ranged from 260 to 380 kg/m^3 and are in the range of snow pits observations. A layer with a larger density (up to 650 kg/m^3) just above the ice corresponded to packed/wet snow added in the deployment hole to fill the freeboard. The complete refreezing of seawater in the deployment holes needed more than 2 months. By analyzing the temperature profiles in the ice and the position of the freezing front in the deployment holes, lateral heat flux densities through the side wall of the holes were estimated. They could reach 10 W/m^2 at the beginning of the refreezing.

Plain language summary

Four sea ice mass balance instruments deployed near the North Pole at the end of September 2015 drifted in the Arctic ocean and recorded repeated temperature profiles and a proxy of conductivity during several months. The evolution of snow and ice thickness, and the density of the layered snow cover have been estimated. The lateral heat fluxes necessary to freeze the sea water present in the deployment hole have also been evaluated.

1. Introduction

In recent years, Arctic sea ice has undergone drastic changes, shifting from a dominating thick and old sea ice to a younger and thinner ice *(Kwok., 2020; Lindsay & Schweiger, 2015; Hansen et al., 2013; Spreen et al., 2011; Maslanik et al., 2011).* Sea ice mass balance has become more dependent on the overlying snow *(Webster et al., 2018; Perovich et al., 2017 b; Sturm and Massom, 2017; Ledley, 1991)*. Snow regulates the energy balance of the planet by reflecting 85% of the incoming solar radiation *(Perovich et al, 2002; Warren, 1982)* : in spring and summer, the high albedo of the snow layer protects the sea ice surface from solar radiation *(Leu et al., 2010)* and delays the onset of its melt *(Petrich et al., 2012)*. In autumn and winter, the low density snowpack plays an insulator role and reduces the heat loss from the ice to the atmosphere. This insulating snow layer slows the sea ice growth, especially for thin ice *(Perovich, 2003; Sturm et al., 2002a; Sturm et al., 2002; Maykut and Untersteiner, 1971)*. Snow-ice formation may occur when the snow/ice interface sinks under the water line (negative freeboard). This process then increases the sea ice contribution to the total Arctic mass balance *(Provost et al., 2017; Granskog et al., 2017)*. It is thus fundamental to determine the snow properties to understand the physical processes at stake in the coupled air/snow/sea-ice/ocean Arctic system *(Sturm and Masson., 2017)*.

Snow is a complex medium with a large spatial and temporal heterogeneity *(Webster et al., 2018; Sturm et al., 2002)*. It is strongly affected by wind, liquid or solid precipitations, and air temperature *(Gani et al., 2019, Merkouriadi et al., 2017b, Bokhorst et al., 2016; Lecomte et al., 2011).* Once deposited on sea ice, snow crystals undergo transformations known as snow metamorphism (*Hobbs, 1968; Colbeck, 1982, Sturm et al., 1998*). These transformations are associated with changes of snow density and insulating properties.

The lack of information on snow properties induces uncertainties on snow depth and sea-ice thickness estimates from satellite radar or laser altimetry (*Nandan et al. 2020; Yackel et al., 2019; Kern et al., 2015; Ricker et al., 2014; Zygmuntowska et al., 2014; Kurtz and Farrell., 2011; Kwok et al., 2011; Giles et al., 2007*).

Snow density measurements are sparse and require an operator (snow pits, SnowMicroPen; e.g. Schneebeli and Johnson, 1998; King et al., 2020; Fierz et al., 2009). SAMS Ice Mass Balance (hereafter SIMBA) installed on drifting buoys are autonomous and continuously measure temperature profiles in snow and ice. These profiles can be used to determine changes of snow depth and ice thickness (Jackson et al., 2013; Provost et al. 2017).

Building on Gani et al., [2019], we here analyse observations provided by four SIMBAs deployed in the Arctic at the end of summer. The stratification, conductivity and density of the snow layer is further investigated through the temperature and heated temperature profiles. The complete refreezing of the SIMBA deployment holes lasted until late November (more than 2 months). It is known from studies made on cracks that the refreezing is a two-dimensional process, from the top to the bottom, due to the vertical heat transfer to the atmosphere, and sideways, due to the lateral heat transfer from the surrounding sea ice *(Petrich et al., 2007).* These lateral fluxes are poorly known. We here give an estimate of their values from the observed temperature profiles. These estimates are corroborated with simulations presented in a companion paper.

The paper is organized as follows. Section 2 describes the experimental set-up, the observations and the different interfaces. The approach used to calculate the snow conductivity and the corresponding results are presented in section 3. Section 4 describes the kinetic of the refreezing in the deployment hole and the lateral flux estimations. Finally, section 5 summarizes the results and provides perspectives.

2. SIMBA observations

2.1 Experimental set up

During the expedition PS94 "TransArc II“ (Trans-Arctic survey of the Arctic Ocean in transition) in September 2015, four IAOOS platforms were deployed in the Arctic around the North Pole, away from immediate active sea-ice deformation processes. The four buoys followed southwestward trajectories with the Transpolar Drift Stream, for a period ranging from 3 to 9 months (Figure 1, Table 1). Each IAOOS buoy carried a SIMBA (Jackson et al., 2013)

hereafter noted S16, S17, S18, and S19 : the controller board and batteries were attached on the IAOOS buoy while the SIMBA chain was put aside with a wooden support to limit perturbations from the buoy (Figure 2). The 5 m long SIMBA chain was inserted into a 5 cm diameter hole drilled in the ice and measured temperatures in air, snow, sea-ice, and ocean. Surrounding snow was put into the hole to fill the gap between the waterline and the ice surface (Figure 2). The wooden support proved to be fragile and broke after some time at S16 and S19 sites (Table 1).

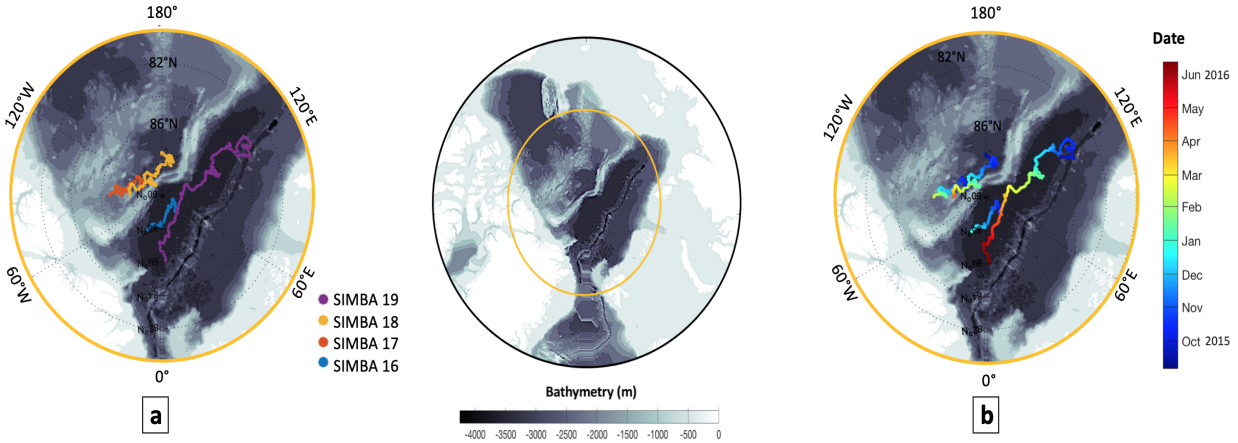

Figure 1. For the four SIMBAs S16, S17, S18, and S19 : **(a)** Trajectories. **(b)** Time evolution. The background is bathymetry (m).

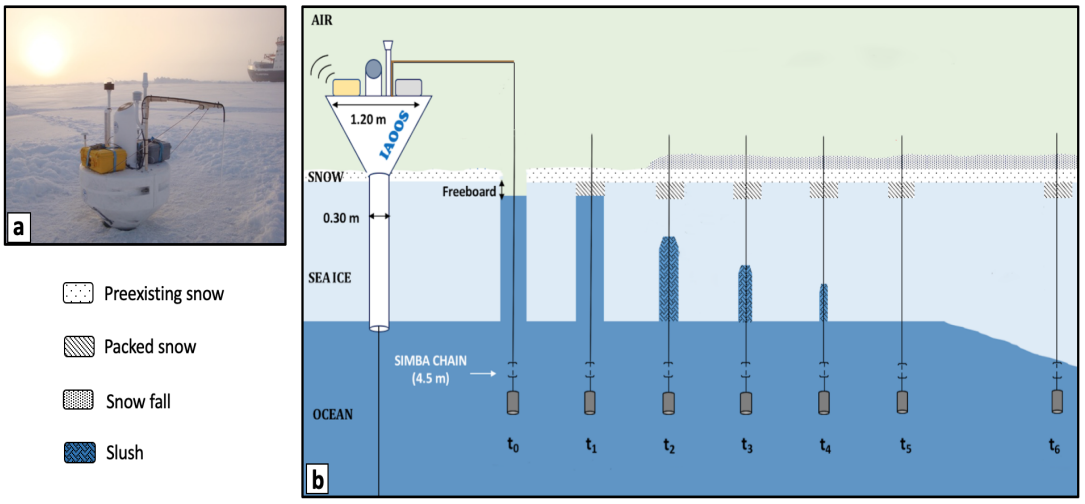

Figure 2. (a) Photograph of the platform. **(b)** Schematic of the set-up and sketch describing the refreezing of the hole around the SIMBA chain. to is the deployment day and t5 the day when the hole is totally frozen.

2.2 Determination of the interfaces

Sensors located every 2 cm on the chain measure temperature with a $\pm 0.1\,°C$ accuracy (*Jackson et al., 2013*). Resistors enable a heating mode during which temperature is measured after 0 s (T0), 30 s (T1), and 120 s (T2) ; To and the temperature differences HST1 = T1-To and HST2 = T2-To are recorded. HST2 can be considered as a proxy of thermal conductivity k (see Appendix 1). Temperature was initially measured every 4 h, while heating with a duration of 120 s was activated once per day. To limit excessive battery consumption during the cold season, the sampling interval was increased to 8 h for temperature and to 5 days for the heating mode from December 19 onward (Table 1).

	S16	S17	S18	S19
Drift duration Start End Support collapse	105 days Sept 5, 2015 Dec 19, 2016 Sept 24, 2015	157 days Sept 11, 2015 Feb 15, 2016	212 days Sept 14, 2015 Apr 13, 2016	254 days Sept 19, 2015 May 30 , 2016 Jan 2, 2015
Initial thickness (cm) Snow Ice Ice draft Freeboard	 0 143 118 25	 0 161 142 19	 5 150 145 5	 1 117 116 1
Initial position Latitude Longitude	 89.3 59.6	 88.8 -121	 87.7 188.3	 84.9 125
Time sampling Temperature (h) Heating mode (days)	 4/8 1/5	 4/8 1/5	 4/8 1/5	 4/8 1/5

Table 1. Temporal coverage, initial conditions (measured at time of deployment), and sampling frequency of the four SIMBAs.

Following Provost et al. (2017), we used the temperature and HST2 profiles to determine the position of the interfaces between the different media (Figures 3, 4, 5). Starting from the top of the chain, a simultaneous large increase of the vertical temperature gradient and decrease of the temporal standard deviation of the temperature defined the *air/snow* interface (Figures 3, 5). The *snow/ice* interface was obtained from the large difference of the HST2 values between both media (Figures 4, 6). As the freeboard was filled with snow at the

deployment, the snow/ice interface corresponds to the initial waterline and the SIMBA derived ice thickness corresponds to the ice draft (Figure 2). The deployment hole was initially flooded with sea water, which gradually solidified and formed a mixture of sea water and ice (slush ice) characterized by HST2 values larger than those of sea water (Figures 4, 6). Note that unlike winter and spring deployments, more than 2 months were necessary for the deployment hole to fully freeze. The *ice/slush* interface was estimated as the location where the slope of the temperature profiles changed. During the refreezing of the hole, the *slush/ocean* interface was set constant at its initial value. Once the hole was completely frozen, the *ice/ocean* interface was determined using the same method as for the ice/slush interface.

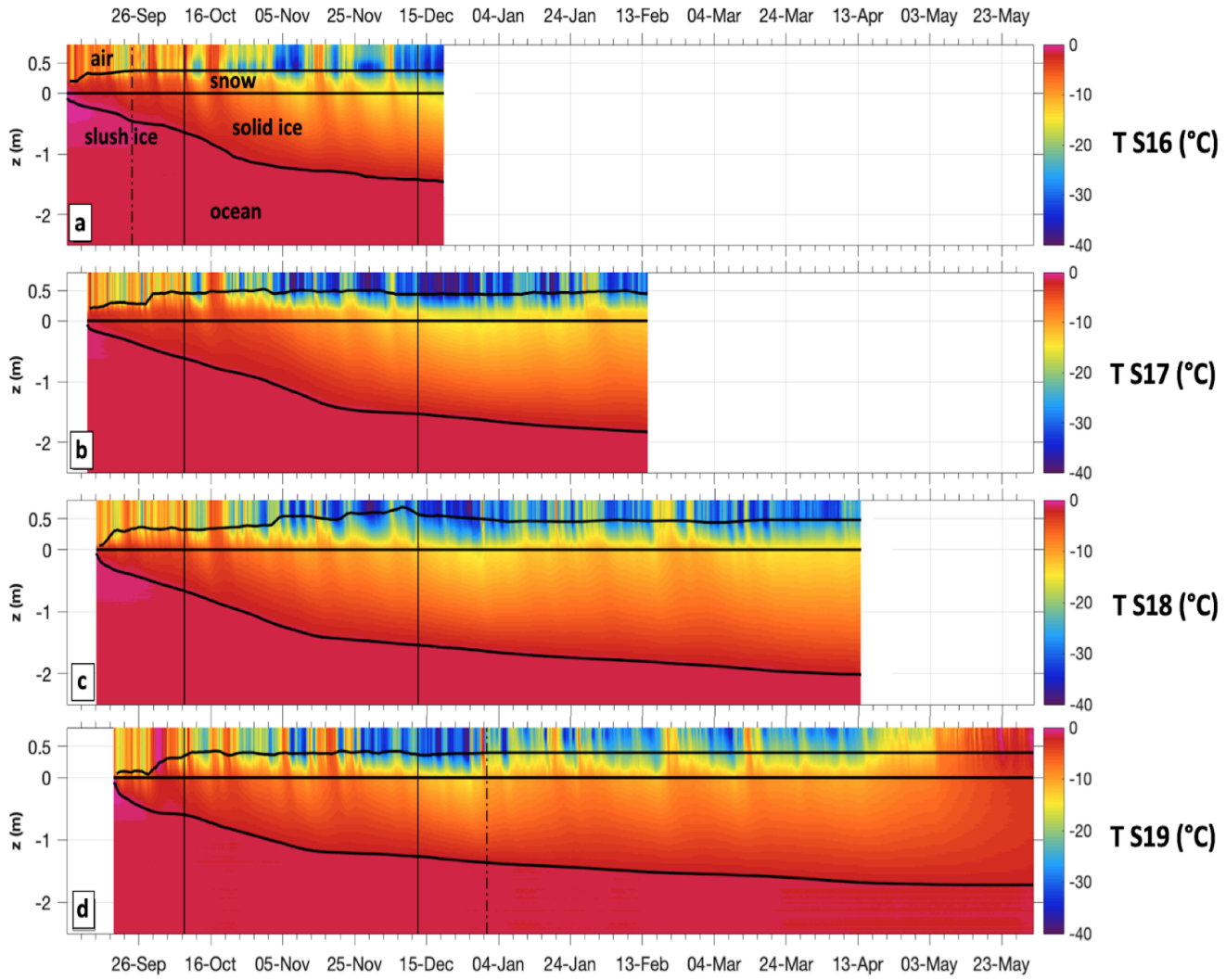

Figure 3. Temperature (°C) along the trajectory for **(a)** S16 **(b)** S17 **(c)** S18 **(d)** S19. The distance between two sensors is 2 cm. Black continuous lines correspond to the air/snow, snow/ice, ice/slush and slush/ocean interfaces. The black dotted line corresponds to the day when the support collapsed (S16 and S19). Black vertical lines refer to the selected temperature profiles in figure 8.

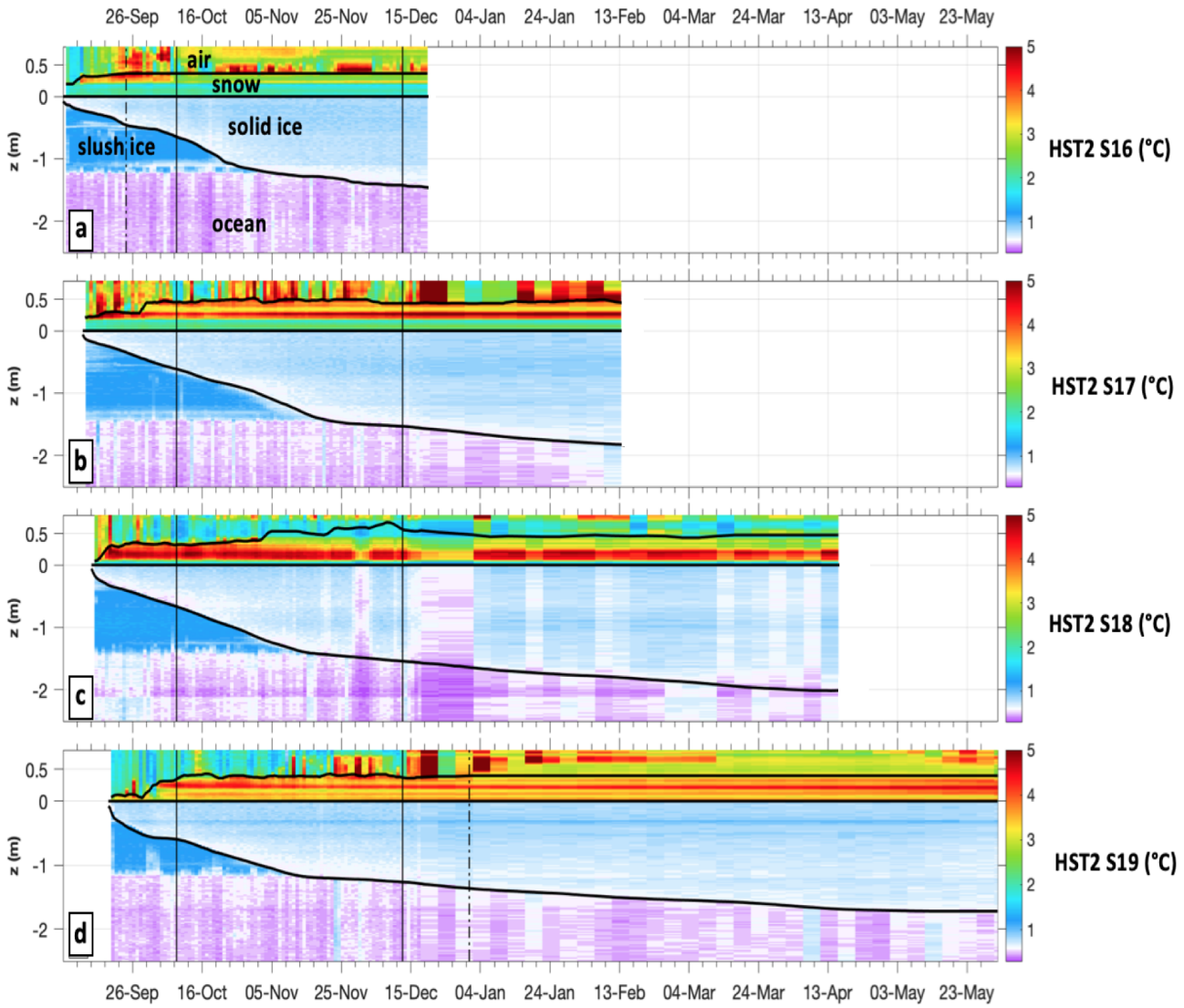

Figure 4. HST2 (°C) along the trajectory for **(a)** S16 **(b)** S17 **(c)** S18 **(d)** S19. The distance between two sensors is 2 cm. Black continuous lines correspond to the air/snow, snow/ice, ice/slush and slush/ocean interfaces. The black dotted line corresponds to the day when the support collapsed (S16 and S19). Black vertical lines refer to the selected temperature profiles in figure 8.

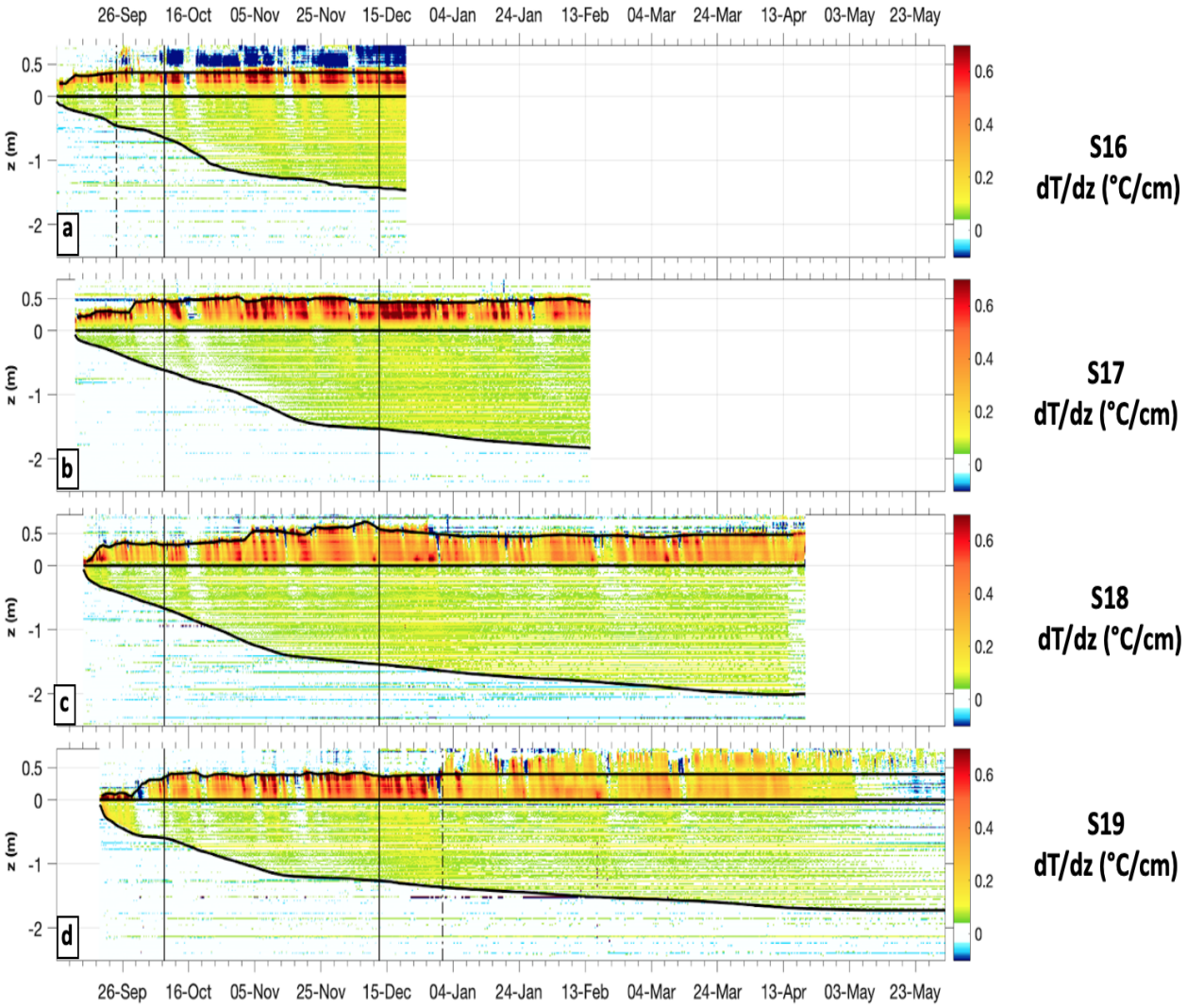

Figure 5. Vertical derivative of temperature dT/dz (°C/cm) along the trajectory for **(a)** S16 **(b)** S17 **(c)** S18 **(d)** S19. The distance between two sensors is 2 cm. Black continuous lines correspond to the air/snow, snow/ice, ice/slush and slush/ocean interfaces. The black dotted line corresponds to the day when the support collapsed (S16 and S19). Black vertical lines refer to the selected temperature profiles in figure 8.

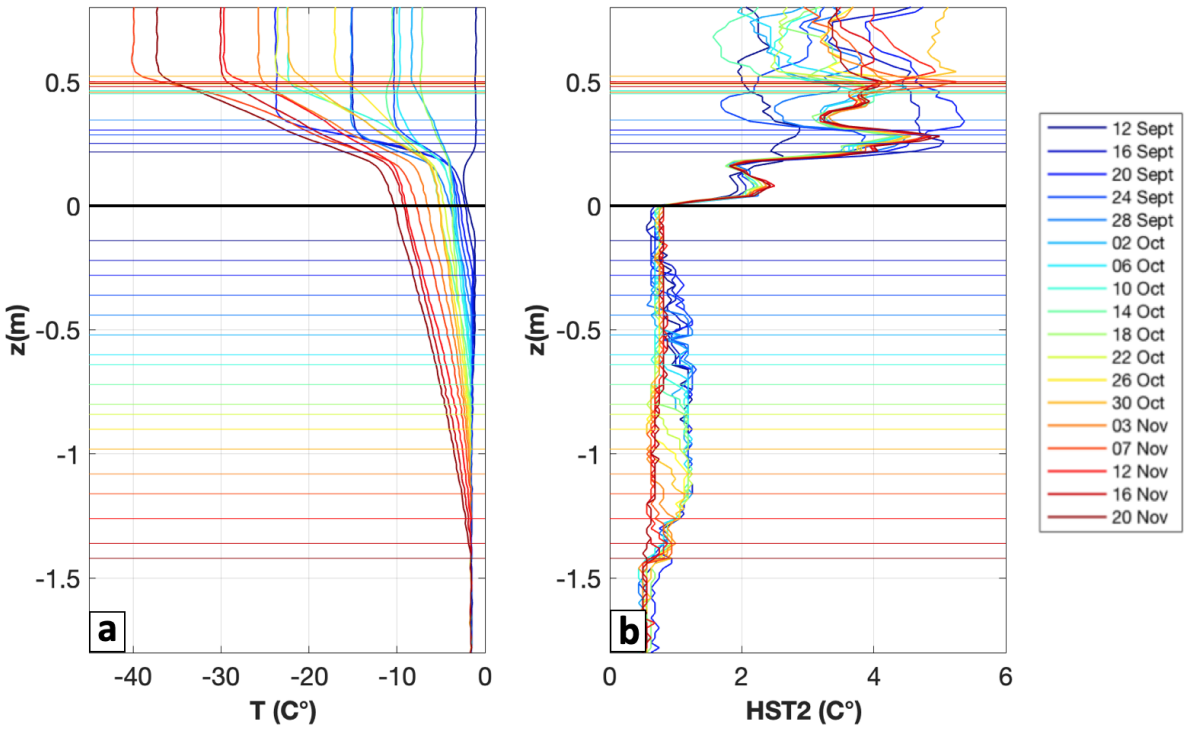

Figure 6. Observed **(a)** temperature profiles and **(b)** HST2 (°C) for S17. The positions of the freezing front at the top of the hole (respectively of the air/snow interface) are indicated by the colored horizontal lines below (above) the black snow/ice interface.

2.3 Evolution of the interfaces

The initial snow thickness corresponds to the initial freeboard value since snow had been added in the deployment hole above the waterline (Table 1). During the drift, the SIMBA recorded snow depths ranging between 0 and 70 cm with significant increases shortly after deployment; September 18 for S16, September 21 for S18, and September 28 for S17 and S19 (Figure 7a). From January 4 onward, snow depths remained around 35 to 50 cm for the four SIMBAs. Note that the air/snow interface was set constant after the support collapsed in S16 (September 24), and S19 (January 2) (Figure 7a). From this date, data above the air/snow interface were not considered. This way, final snow thicknesses range from 37 cm for S16 to 48 cm for S18 (44 cm for S17 and 40 cm for S19).

The observed ice thickness at deployment ranged from 1,17m (S19) to 1,61m (S17). The deployment hole drilled in sea-ice progressively refroze (Figure 2). The chain documented the evolution of the freezing front in the hole, that is the interface between the solid ice

(Figure 7b) and the slush ice below (Figure 7c). After one or two days of fast refreezing, the freezing front deepens at an average speed of 2 cm/day for the four SIMBAs (Figure 7d). Note that the position of the freezing front in the hole for S19 did not change during 8 days from September 30 (Figure 7c). This is due to a week-long burst of warm air, with temperature around zero degree (Figure 3d) associated with a snow depth increase of 30 cm (Figure 7a). The refreezing of the holes took between 58 and 72 days (Figure 7c). From then on, the ice growth rate was about 0.8 cm/day for all the SIMBAs (Figure 7d).

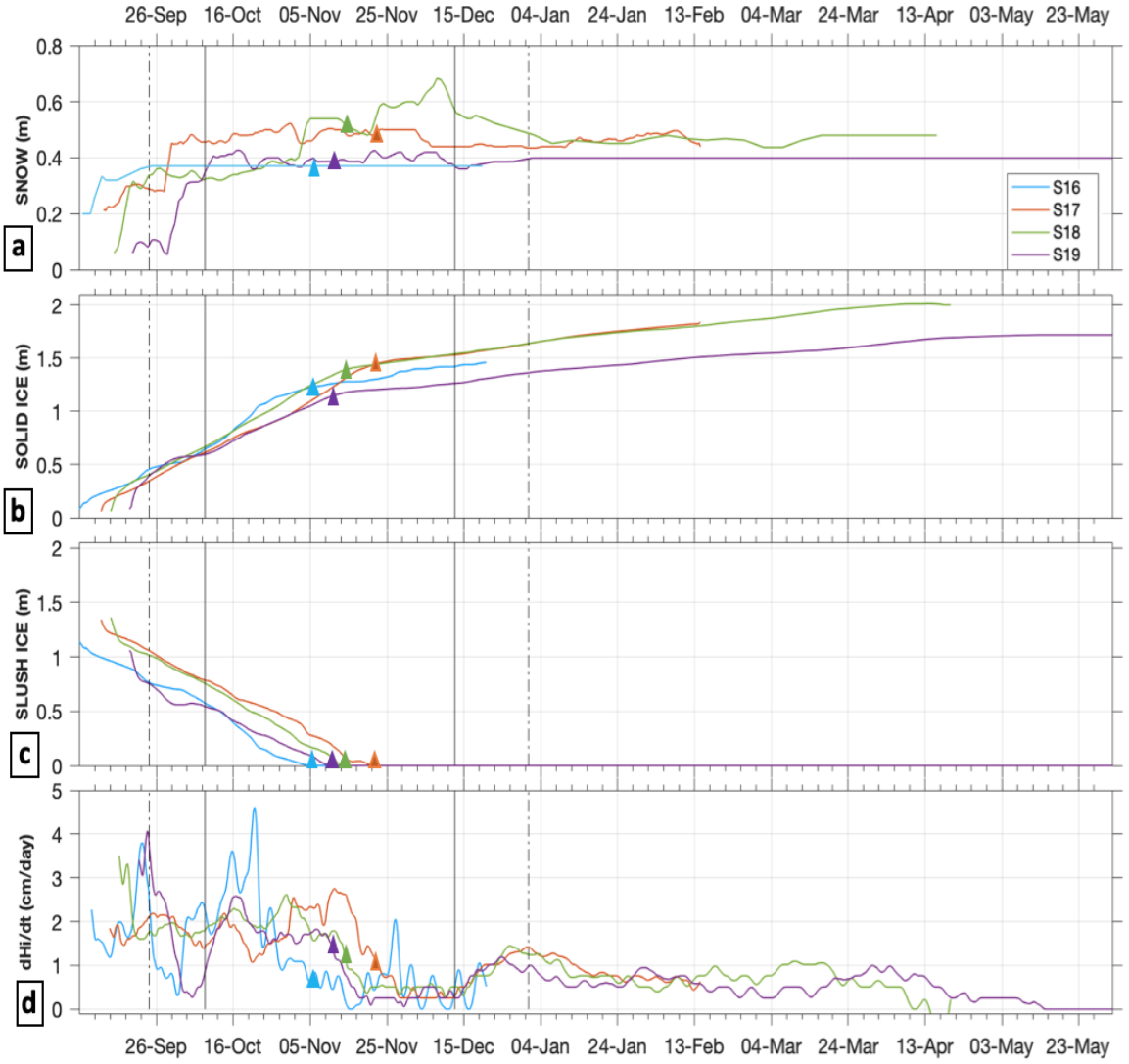

Figure 7. Time series of **(a)** snow thickness (m), **(b)** solid ice thickness (m), **(c)** slush thickness h(t) (m), and **(d)** solid ice growth rate (cm/day) for S16, S17, S18, and S19. The triangles indicate the end of refreezing in the deployment hole. The black dotted line corresponds to the day when the support collapsed (S16 and S19). Black vertical lines refer to the selected temperature profiles in figure 8.

3. Analysis of snow data

3.1 Stratification of the snow

The four SIMBAs featured different HST2 values in the snow and, in some cases, snow layers with distinct properties could be identified. HST2 is a proxy of the conductivity (see Appendix 1); the larger the conductivity, the smaller HST2. As a result, changes in HST2 in snow (Figure 8a, c) reflect changes in conductivity and correspond to slope breaks in the temperature profile (Figures 8b, d).

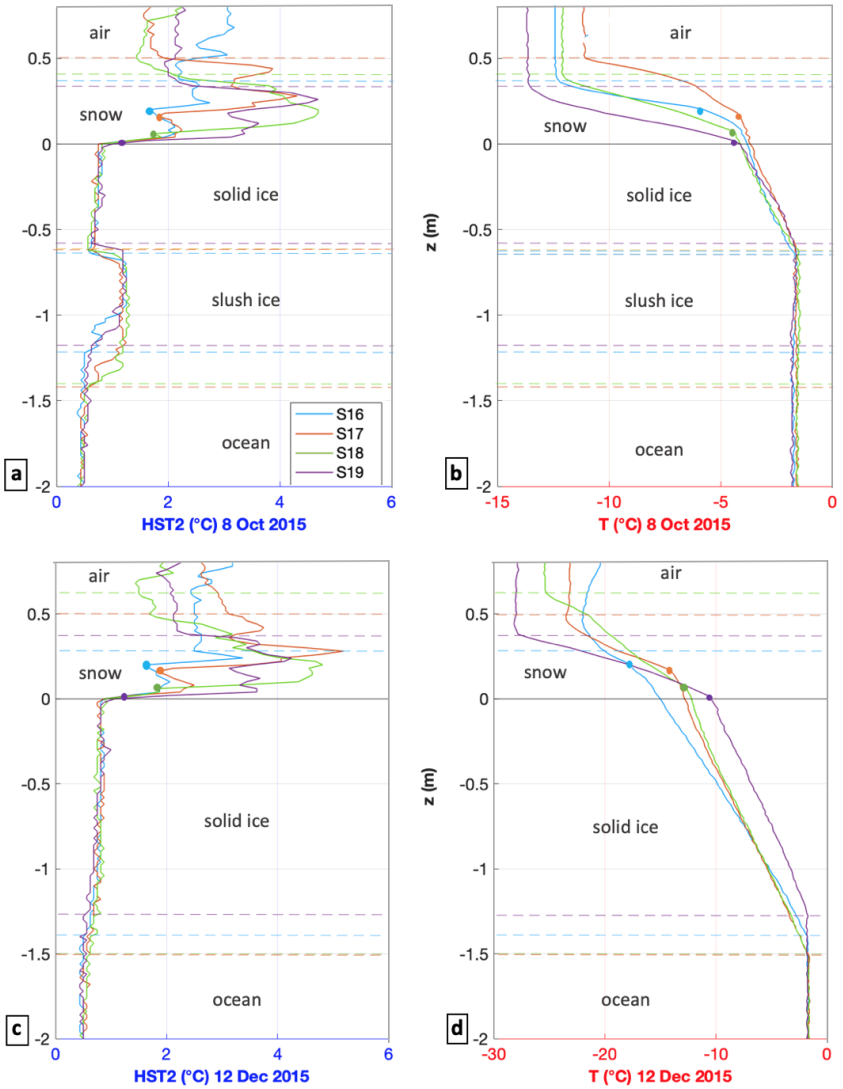

Figure 8. For the four SIMBAs **(a)** HST2 profile (°C) and **(b)** temperature profile (°C) on October 8. **(c)** Same as (a) on December 12. **(d)** Same as (b) on December 12. The colored dots show the freeboard position.

For S16, S17, and S18, the freeboard filled with snow (located between the colored dots and the snow/ice interface (z=0) in Figure 8) corresponds to HST2 values around 2 °C (Figures 8a, c) and to the steepest part of the temperature profile (Figures 8b, d) in the snow layer. These values persisted throughout the drift (Figures 4a, b). For S19, the freeboard did not exceed 1 cm at the deployment and is not visible on the HST2 and temperature profiles. Above the freeboard, HST2 values were larger, reaching 3 to 5°C (Figure 8a), and probably correspond to fresh snow accumulated between the deployment and October 8 (Figure 6, 7a). For S17 two distinct snow layers with different HST2 values can be identified above the freeboard (Figure 8a).

On October 8, S18 profiles featured an homogeneous snow layer above the freeboard (depth around 35 cm, HST2 values close to the midpoint around 4°C, and a linear temperature profile with no slope break) (Figures 8a, b). On December 12, the snow thickness was about 60 cm at S18 site (Figure 8d). HST2 values were not reliable as the heating mode was deficient in the upper part of the chain.

3.2 Estimates of snow conductivities and densities

The S17 series which exhibited three different snow layers (two different snow layers above the freeboard) is chosen to illustrate the method followed to estimate the snow conductivity and density (Figure 9).

The heat flux density through the snow and the ice is defined by the relation

$$J_0(t,z) = -k\frac{\partial T(t,z)}{\partial z} \qquad (1)$$

where k is the conductivity of the considered medium (ice or snow layer) at the depth *z*. In stationary conditions, $J_0(t,z)$ no longer depends on t and z and the vertical derivatives of the temperature are constants.

Consequently

$$J_0 = -k_i\frac{\partial T_i}{\partial z} = -k_{sj}\frac{\partial T_{sj}}{\partial z} \qquad (2)$$

where k_i and k_{sj} (j = 1,2,3) are respectively the conductivities of the ice and of the snow layers (Figure 10). Knowing J_0 and the vertical derivatives of temperature in snow, it is then possible to determine the conductivity of each snow layer.

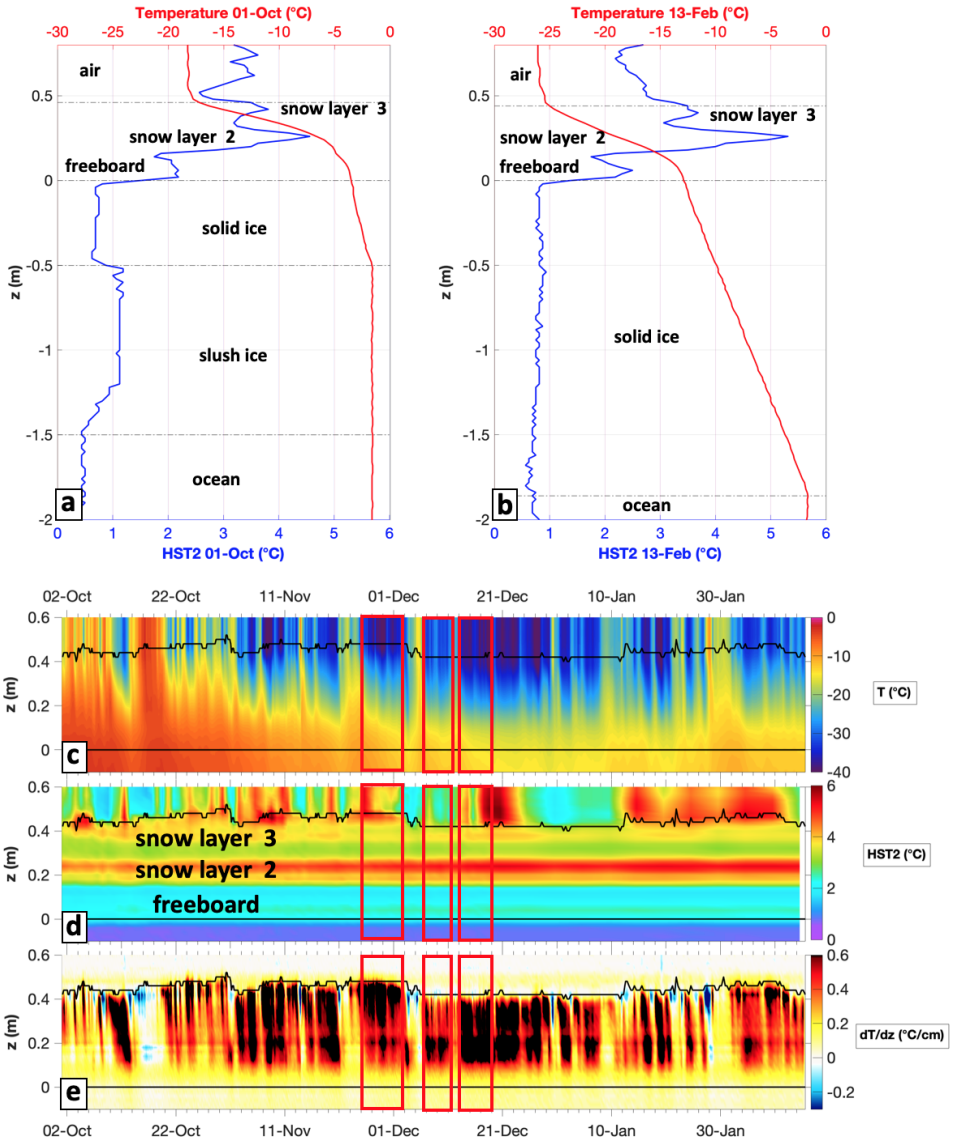

Figure 9. Observed diffusivity proxy (blue) and temperature profiles (red) for S17 on **(a)** October 1 **(b)** February 13. Along the trajectory: close up of snow **(c)** Temperature (°C) **(d)** HST2 (°C) **(e)** Vertical derivative of temperature (**°C/cm).** Air/snow and snow/ice interfaces are represented by black lines. Red boxes correspond to periods selected for the computation of the snow density, when the time derivative in air temperature remains less than 0.1°C/h (quasi stationary states).

Assuming that the snow cover is made of three distinct homogeneous layers, the heat flux density J_0 through the snow cover is also given by the relation

$$J_0 = \frac{(T_{surf} - T_{ice})}{\frac{Z_1}{k_{s1}} + \frac{Z_2}{k_{s2}} + \frac{Z_3}{k_{s3}}} \qquad (3)$$

where Z_i and k_{sj} are the thicknesses and conductivities of each snow layer (Figure 10). The sensible heat flux density through the snow cover is thus proportional to the difference between the temperature at the air/snow and at the snow/ice interfaces $T_{surf} - T_{ice}$(this temperature difference is indicated in Figure 10). For each snow layer and for the ice, the vertical derivative of temperature is thus proportional to the temperature difference $T_{surf} - T_{ice}$ and depends on the layer conductivity k_{sj}.

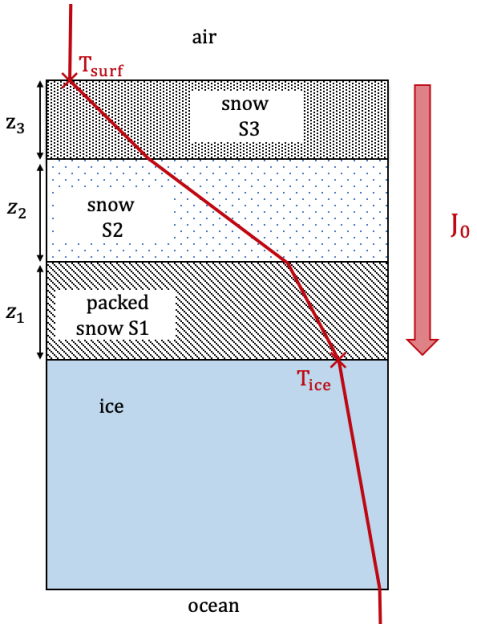

Figure 10. Schematic of the snow and ice configuration at the S17 site. The sensible heat flux through snow J_0 is proportional to the temperature difference $T_{surf} - T_{ice}$between air/snow and snow/ice interfaces. The depths of each snow layer are specified by Z_1, Z_2, Z_3.

The scatter plot of HST2 (proxy of conductivity) and *dT/dz* for the snow and the upper part of the ice illustrates the variability of the conditions experienced by the snow. The plot features distinguishable clouds of points (Figure 11a). We discriminate the ice (HST2 ~ 0.6°C and *dT/dz* ~ 0.1 °C/cm), the ice/snow interface (HST2 ~ 1.3°C and dT/dz ~ 0.09°C/cm), the packed snow

layer corresponding to the freeboard (HST2 ~ 2.2°C and dT/dz ~ 0.2 °C/cm), and the snow cover with a wide range of values (HST2 ~3 to 5.5 °C). The two layers of snow above the freeboard are however impossible to distinguish. Note that the blue dots correspond to warm air temperature bursts, leading to a larger temperature at the air/snow interface than at the snow/ice interface.

To compute the different snow conductivities, it is indispensable to determine quasi stationary periods. We thus selected periods for which the time derivative of the air temperature dT/dt was smaller than 0.1°C/h (red boxes in Figure 9c, d, and e). We only took into account temperature profiles with a temperature difference between air/snow and snow/ice interfaces $T_{surf} - T_{ice}$ exceeding 15°C. By plotting only these selected period data (Figure 12), we could distinguish the snow layer 2 (HST2 ~ 3.7°C and dT/dz ~ 0.67 °C/cm), and the snow layer 3 (HST2 ~ 4.9°C and dT/dz ~ 0.74 °C/cm, Figure 11b).

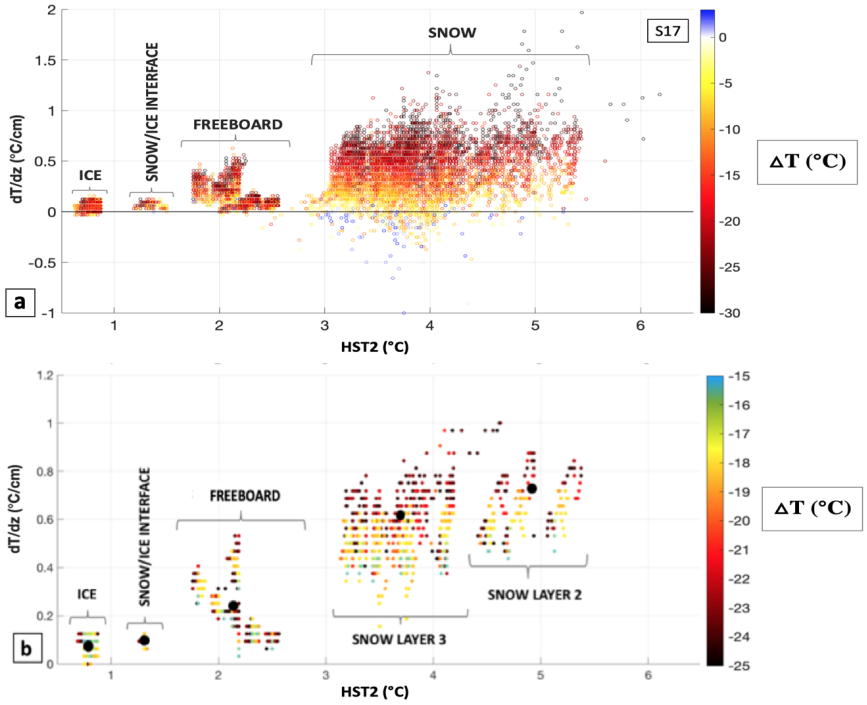

Figure 11 (a) Vertical derivative of temperature (°C/cm) as a function of HST2 (°C) for S17. The color bar shows the temperature difference between the air/snow and the snow/ice interfaces. **(b)** Vertical derivative of temperature as a function of HST2 for periods when the time derivative of the air temperature was less than 0.1°C/h and the temperature difference between the air and the ice just below the snow/ice interface exceeded 15°C. The color bar shows the temperature difference between the air/snow and the snow/ice interfaces. Black points designate the barycenter of each layer in (dT/dz, HST2) space.

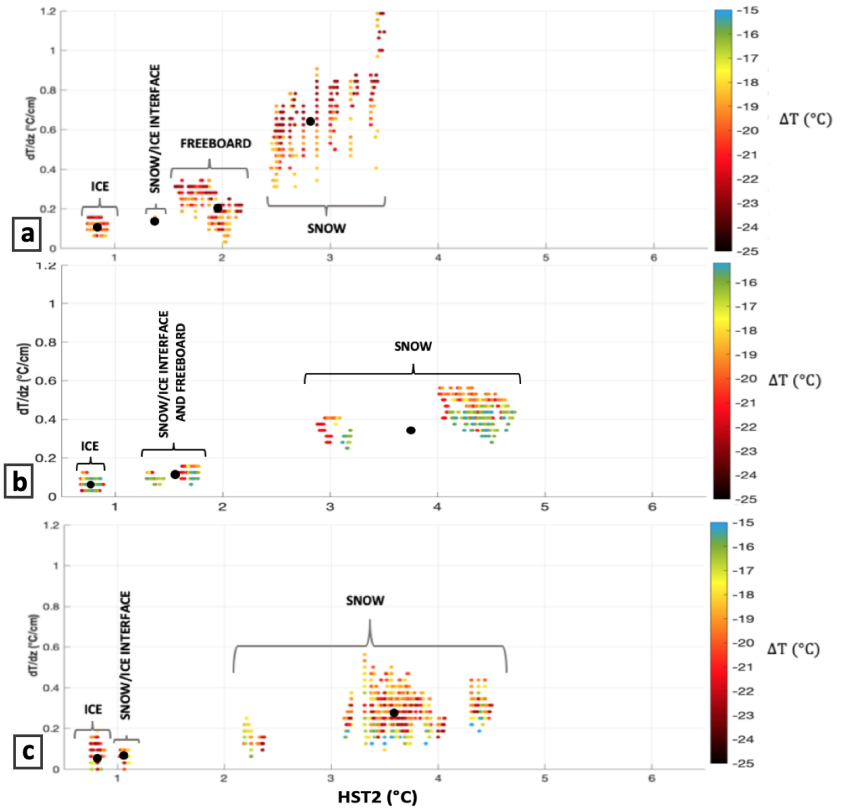

Figure 12. (a)S16, **(b)** S18, **(c)** S19 vertical derivative of temperature as a function of HST2 for periods when the time derivative of the air temperature was less than 0.1°C/h and the temperature difference between the air and the ice just below the snow/ice interface exceeded 15°C. The color bar shows the temperature difference between the air/snow and the snow/ice interfaces. Black points designate the barycenter of each layer in (dT/dz, HST2) space.

The vertical derivatives of temperature of ice $\frac{\partial T_i}{\partial z}$ and snow $\frac{\partial T_{sj}}{\partial z}$ are estimated from their average value in each medium (black dots in Figure 11). Starting from ice conductivity values of 1.8 and 2.2 W/m/K, J_0 is estimated. Then the conductivity of the packed snow (corresponding to the initial freeboard) and of the second and third snow layers are computed using the relation (2).

As in Gani et al. (2019), we used the Abel's relation to estimate the snow density in each layer from the conductivity:

$$k_s = 2.846 \times 10^{-6} \times \rho_s^2 \qquad (4)$$

Following the same approach for the other three SIMBAs (selecting data with dT/dt < 0.1°C/h and $T_{surf} - T_{ice}$ > 15°C), we estimated the conductivity and density of the different snow layers

(see Figure 12 and Table 2). Using an ice conductivity of 2.2 $W.m^{-1}.K^{-1}$, the calculated snow densities ranged from 530 (S17) to 660 (S16) kg/m^3 (480 to 595 kg/m^3 for $k_i = 1.8\,W.m^{-1}.K^{-1}$) for the freeboard values (packed snow) and from 289 to 377 kg/m^3 (261 to 342 kg/m^3 for $k_i = 1.8\,W.m^{-1}.K^{-1}$) for the other snow layers. These snow densities, in the range of observations made in snow pits (Merkouriadi et al., 2017 b; King et al., 2020), are used in simulations carried out in the companion paper.

For $k_i = 2.2$ $k_i = 1.8$ $(W.m^{-1}.K^{-1})$	$k_{FB}(s1)$ $(W.m^{-1}.K^{-1})$	$\rho_{FB}(s1)$ (kg/m^3)	k_{s2} $(W.m^{-1}.K^{-1})$	ρ_{s2} (kg/m^3)	k_{s3} $(W.m^{-1}.K^{-1})$	ρ_{s3} (kg/m^3)
S16	1.20 0.98	650 587	0.38 0.31	366 331	/	/
S17	0.80 0.65	530 480	0.26 0.21	304 275	0.24 0.19	289 261
S18	1.24 1.01	660 595	0.34 0.28	346 313	/	/
S19	/	/	0.41 0.33	377 342	/	/

Table 2. Calculated snow conductivities and densities for each snow layer for the four SIMBAs.

The relationship between snow conductivity and HST2 was further investigated for an ice conductivity of 1.8 W/m/K and of 2.2 W/m/K (respectively red and black dots in Figure 13). The best dashed-cubic fit to these dots provided tentative continuous estimates of snow conductivity as a function of HST2. To test the relevance of these curves, we applied them to the data used in Gani et al. [2019]. For the so-called SIMBAa (SIMBAh), the observed mean snow HST2 of 3.09 °C (2.87 °C) led to conductivity estimates between 0.42 and 0.33 W/m/K (0.40 and 0.51 W/m/K) and therefore to a density between 338 and 383 kg/m^3 (376 and 423 kg/m^3) using Abel's relation. This is in good agreement with the snow density values of 370 kg/m^3 (390 kg/m^3) obtained by tuning the snow density in numerical experiments (Gani et al., 2019).

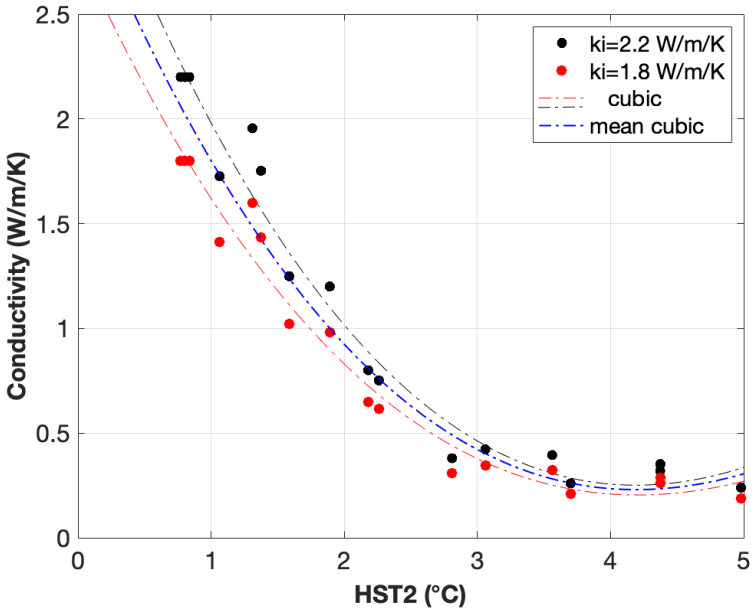

Figure 13. Snow conductivity (W/m/K) obtained from computation explained in 3.2, as a function of HST2 (°C). Two series are represented; the red one is computed with an ice conductivity of 1.8 W/m/K and the black one with an ice conductivity of 2.2 W/m/K. The dash-dotted curves show the best cubic fit related to these points. The blue dash-dotted curve shows the mean best cubic of all the points :

$k = -0.01 \times HST2^3 + 0.25 \times HST2^2 - 1.5 \times HST2 + 3.1$; $R^2 = 0.97$; $RMSE = 0.43$)

The time evolution of the snow density profile at S17, obtained from the cubic curves in Figure 13, shows that density remained rather constant at each level and variations were small, mostly below 50 kg/m^3 (Figure 14). Snow density did not show any trend, except in the freeboard denser layer, where it decreased from about 550 to 450 kg/m^3. The stability of snow density in this winter period is consistent with Gallet et al. [2017].

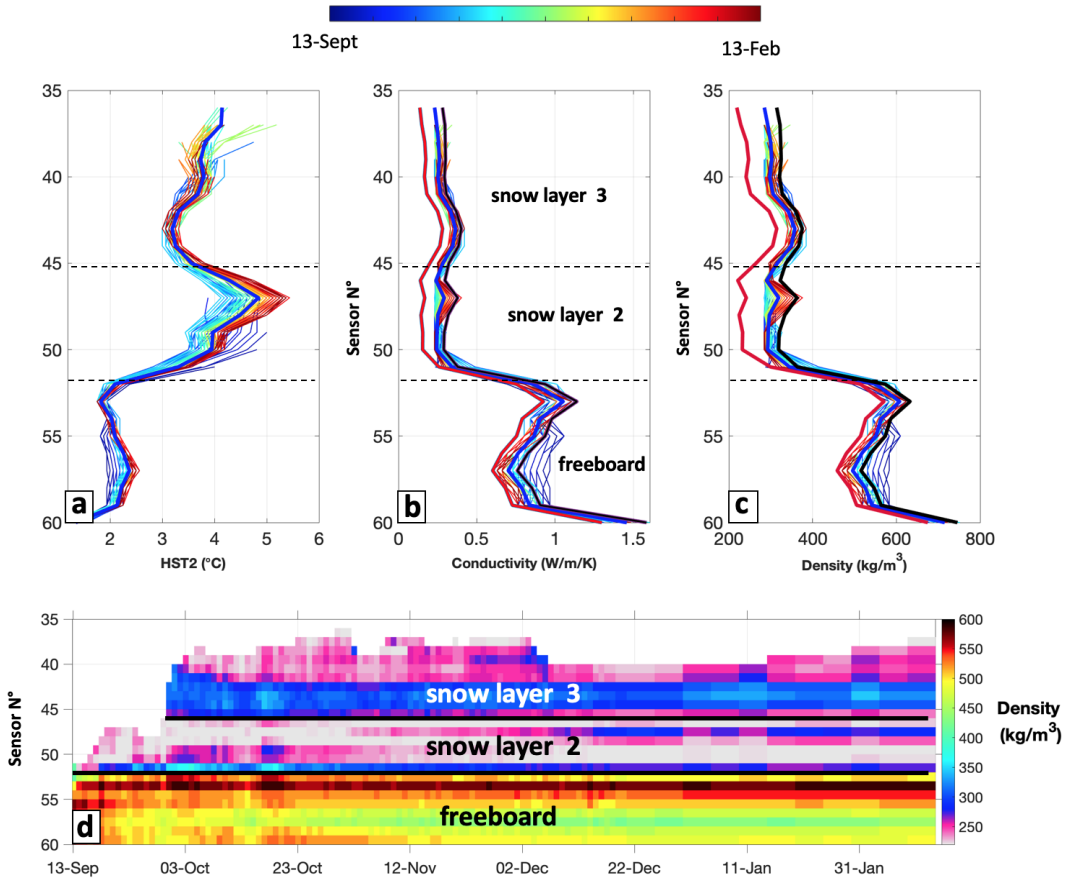

Figure 14. For S17: **(a)** HST2 (°C) profiles. **(b)** Conductivity (W/m/K) profiles obtained from the mean blue cubic curve in Figure 13. **(c)** Density (kg/m^3) profiles obtained from the conductivity and Abel's relation. Red (respectively black) bold profile corresponds to the mean profiles using an ice conductivity of 1.8 $W.m^{-1}.K^{-1}$ (2.2 $W.m^{-1}.K^{-1}$). **(d)** Time evolution of the snow density profile (kg/m^3).

4. Kinetics of the refreezing in the deployment hole

We investigated the kinetics of the two-month long refreezing of the deployment hole and estimated lateral fluxes due to heat transfer from the surrounding sea ice.

4.1 Lateral density heat fluxes estimated from observations

Heat flux densities through the side wall of the deployment hole were estimated from the SIMBA data using two different methods.

4.1.1 Energy balance method : vertically integrated flux densities

The latent heat required to fully refreeze the water in the hole is $L = \rho\mathcal{L}(\pi R_0^2 H_0)$ where $\mathcal{L}$ is the latent heat per mass unit, ρ the sea water density, H_0 the initial height of the hole, and R_0 the initial hole radius. This energy is provided through three heat flux densities: $J_{top}(t)$ through the top of the hole, $J_{lat}(t)$ through the side wall, and $J_{bot}(t)$ through the bottom of the hole (Figure 15b). More precisely, the following relation must be verified:

$$L - \mathcal{L}\rho\pi R^2(t)h(t) = \int_0^t (\pi R^2(u) J_{top}(u) + 2\pi R(u)h(u)J_{lat}(u) + \pi R^2(u) J_{bot}(u))du \quad (5)$$

where $h(t)$and $R(t)$ are respectively the slush thickness and radius at time *t*. The flux density $\mathcal{J}_{top}(t)$ is estimated from the temperature profile in the ice above the deployment hole:

$$J_{top}(t) = -k_i \partial_z T(t, H_0 - h(t))_{z=H_0-h(t)} \quad (6)$$

Assuming that the heat flux density J_{bot} is negligible, the relation simplifies and reads

$$L - \mathcal{L}\rho\pi R^2(t)h(t) = \int_0^t (\pi R^2(u) J_{top}(u) + 2\pi R(u)h(u)J_{lat}(u))du \quad (7)$$

The instantaneous heat flux density is also estimated through the derivative of equation (7)

$$J_{lat}(t) = \frac{-\pi R^2(t)\,((h'(t)+2h(t)\,R'(t)/R(t))\,\mathcal{L}\rho + J_{top}(t))}{2\pi R(t)h(t)} \quad (8)$$

This way, we obtain the vertically integrated lateral heat flux density as a function of time: the SIMBA data provide the slush thickness *h(t)*, its time derivative *h'(t)*, and the vertical derivative of temperature $\partial_z T(t)$ in the solidified ice, and we assume that the slush radius *R(t)* linearly decreases from its initial value (2.5 cm) to 0.

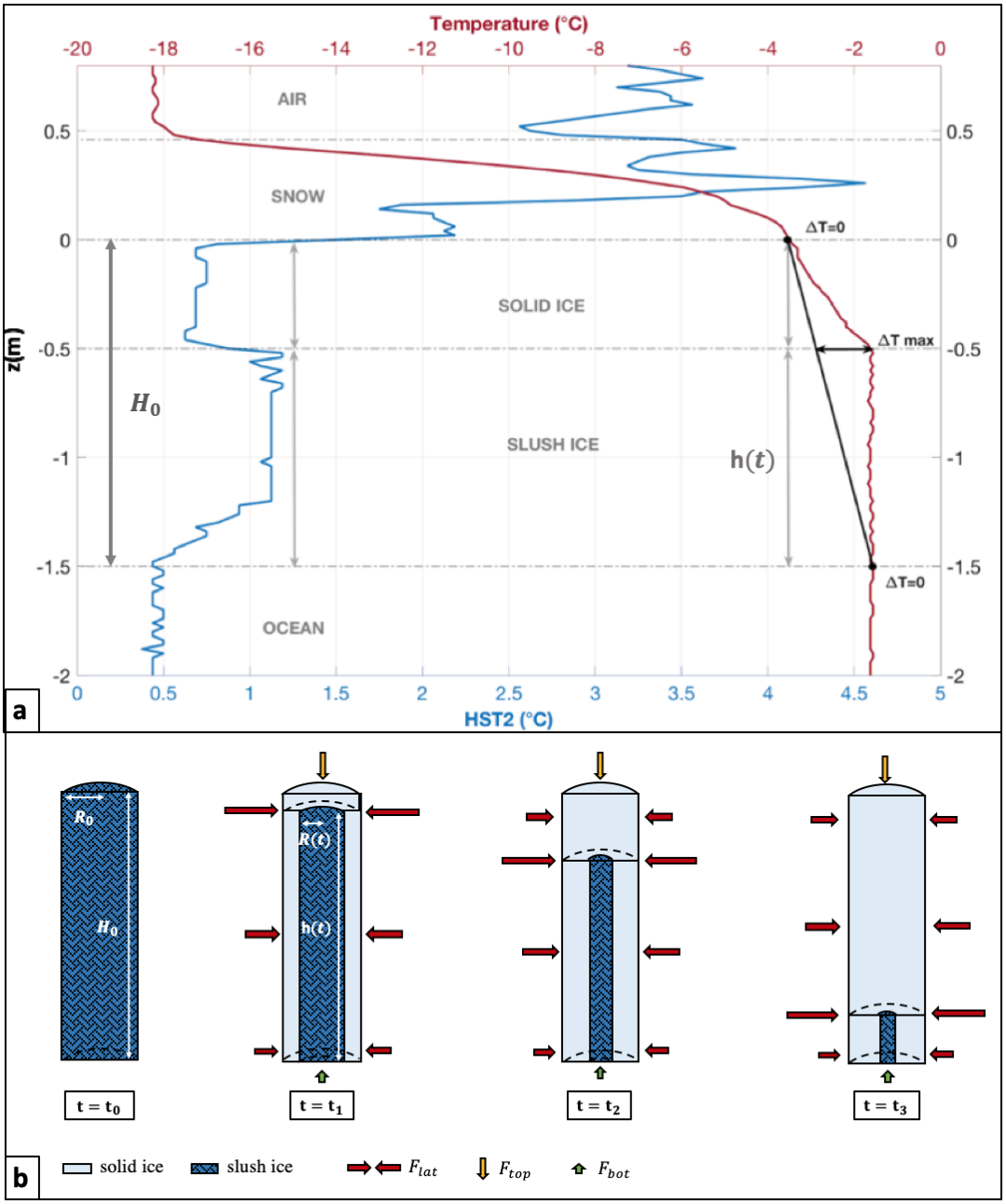

Figure 15. (a) Observed temperature (red) and diffusivity proxy (blue) profile on October 1 for S17. The temperature profile in the surrounding ice (black) is assumed to be linear, which gives ΔT used to compute the lateral flux. **(b)** Sketch illustrating the progressive refreezing of the deployment hole. The heat flux densities: $F_1(t)$ through the top of the hole, $F_2(t)$ through the side wall, and $F_3(t)$ through the bottom of the hole are symbolized by colored arrows.

4.1.2 Vertically dependent flux density estimates

The second method is more direct but requires supplementary hypotheses. We note $j_{lat}(t,z)$ the lateral heat flux density at a depth z below the snow/ice interface. It is given by Fourier law :

$$j_{lat}(t,z) = -k_i \partial_r T(r,z,t)_{r=R(t)} \quad (9)$$

where r is the distance from the axis of the deployment hole and $R(t)$ the slush radius. Supplementary assumptions must be made to estimate this derivative. We first assume that the temperature profile in the surrounding ice $T_{sur}(t,z)$ is linear between the interface temperature $T_i(t)$ just below the snow and the bottom temperature fixed by the underlying ocean $T_{oce}(t)$ (Figure 15a). This reads

$$T_{sur}(z,t) = \frac{(h_i(t)-z)T_i(t)+zT_{oce}(t)}{h_i(t)} \quad (10)$$

where $h_i(t)$is the surrounding ice thickness.

We then estimate $\partial_r T(r,z,t)_{r=R(t)}$ as a simple finite difference

$$\partial_r T(r,z,t)_{r=R(t)} = \frac{T_{sur}(z,t)-T_{obs}(z,t)}{D} \quad (11)$$

where $T_{obs}(z,t)$is the measured temperature in the ice or in the deployment hole. This estimation requires a geometrical parameter D, which is the distance between the hole and the location in the surrounding ice where the temperature profile is linear. This distance has to be estimated.

With these approximations:

$$j_{lat}(t,z) = -k_i \frac{h_i(t)(T_i(t)-T_{obs}(z,t))+z(T_{oce}(t)-T_i(t))}{D\,h_i(t)} \quad (12)$$

SIMBAs provide $T(z,t)$, and the surrounding ice thickness $h_i(t)$ required in equation (12).

We define the lateral heat flux density $J_{lat2}(t)$, which is the mean value over the slush depth $h(t)$ of the flux density $j_{lat}(t,z)$:

$$J_{lat2}(t) \approx \frac{\int_{h_i(t)-h(t)}^{h_i(t)} j_{lat}(z,t)dz}{h(t)} \qquad (13)$$

We performed a sensitivity study to the parameter D and assessed the validity of the approximations comparing $J_{lat}(t)$ ($method\ 1\ section\ 4.1.1$) with $J_{lat2}(t)$ ($method\ 2$).

4.2 Evolution of the lateral flux

The evolution of the vertical flux $F_{top}(t)$ and the lateral flux $F_{lat}(t)$ and $F_{lat2}(t)$ are obtained by multiplying the flux densities $J_{top}(t)$, J_{lat}(t), $J_{lat2}(t)$ by the corresponding surface (the disk area $\pi R(t)^2$ for $J_{top}(t)$ and the cylinder area $2\pi R(t)h(t)$ for $J_{lat}(t)$ and $J_{lat2}(t)$). The flux $F_{lat}(t)$ is one order of magnitude larger than $F_{top}(t)$ (Figure 16c, d). For the four SIMBAs, the flux $F_{top}(t)$ decreases throughout the drift from about 0.03 to 0 W (Figure 16c). The general decrease reflects the deepening of the freezing front in the hole. $F_{top}(t)$ is also modulated by the snow depth variations (see for example series S19 in Figures 16b, c after September 30). For the four SIMBAs, the flux $F_{lat}(t)$ decreases from 0.3 to 0 W while fluctuating (Figure 16d). For S17 and S18, $F_{lat}(t)$ regularly decreases. For S19, $F_{lat}(t)$ collapses on September 30, due to a burst of warm air (Figure 16 a) associated with a snow thickness increase (up to 0.30 m, Figure 16b). The S16 support fell down on September 24; the snow depth and surface temperature are therefore uncertain from this date. This leads to less precise flux calculation.

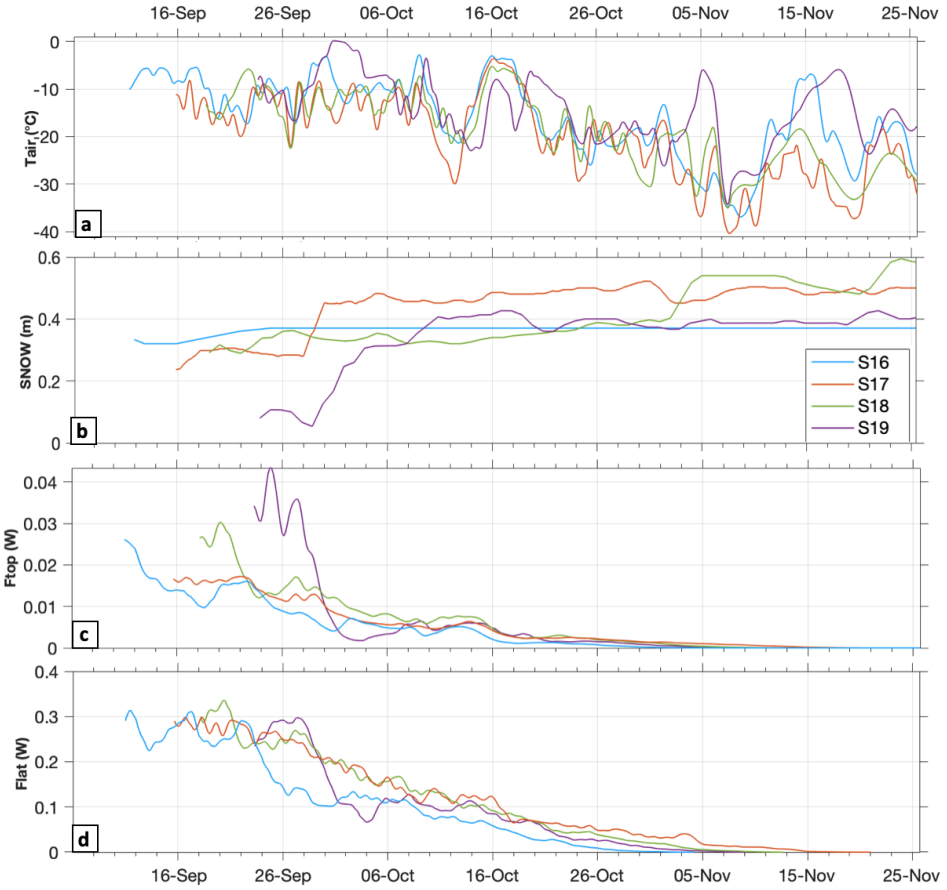

Figure 16. For the four SIMBAs : **(a)** Air temperature (°C) **(b)** Snow thickness (m). Heat fluxes (W) estimated with the energy balance method **(c)** through the top of the hole ($F_{top}(t)$) and **(d)** through its side wall ($F_{lat}(t)$).

To assess the validity of the hypotheses involved in the second method, we computed $J_{lat2}(t, z)$ using distance D values ranging from 0.40 m to 1.20 m and integrated it vertically to compare $F_{lat2}(t)$ to the flux $F_{lat}(t)$ obtained using the energy balance method (Figure 17 a, b, c, d). The two methods give comparable results. $F_{lat2}(t)$ (Figure 17 a, b, c, d) and $F_{top}(t)$ (Figure 16c) strikingly covary as they directly depend on the temperature at the snow/ice interface (equation 6 and 9). The distance D for the best agreement between the two methods is 1.0 m for S18, and around 0.80 m for S17. This difference could be due to the insulating packed snow introduced above the waterline at S17 site, which results in the use of a slightly overestimated temperature at the snow/ice interface (equation 10). It is more difficult to

estimate an optimal D for S16 and S19, since it clearly changes between the beginning and the end of the series. For S19, the second method overestimates the total heat fluxes at the beginning of the series when the snow cover is very thin and the ice thickness is about 1.1 m. Note that when the air temperature rapidly increases, the temperature profile in the surrounding ice is not linear since the system is no longer in a quasi stationary state. In this case the agreement between the two methods might deteriorate; this occurs for example when the air temperature rapidly varies from October 10 to 16 (Figure 16a, 17a, b, c) and at the beginning of the drift for S18 and S19.

The evolution of the lateral density flux profile $J_{lat2}(t, z)$with D = 0.80 m is shown in Figures 17 c, d, e, f, for each SIMBA. The maximum density flux is located at the ice/slush interface, where the temperature difference ΔT between the slush in the hole and the surrounding ice is maximum, and decreases down to zero towards the slush/ocean and ice/snow interfaces, where $\Delta T = 0$ (Figure 15a). The lateral heat flux density for S19 peaks at $15\, W/m^2$ at the beginning of the series at the slush/solid ice interface (Figure 17g). Those large values correspond to the thin insulating snow layer (less than 0.1 m) (Figure 7a) and a small ice thickness (1.17 m) (Figure 7b); as a result, the temperature difference between the slush and the surrounding ice was large at the slush/solid ice interface. In contrast, S17, with a rather deep (0.30m) insulating snow layer and an initial ice thickness of 1.61 m, featured small lateral heat flux density ($3\, W/m^2$). For the four SIMBAs, the lateral heat flux density decreases during bursts of warm air (Figure 16a), for example on October 16 for S16, S17, and S18, and around September 30 for S19 which is not in the same region (Figure 17e,f,g,h).

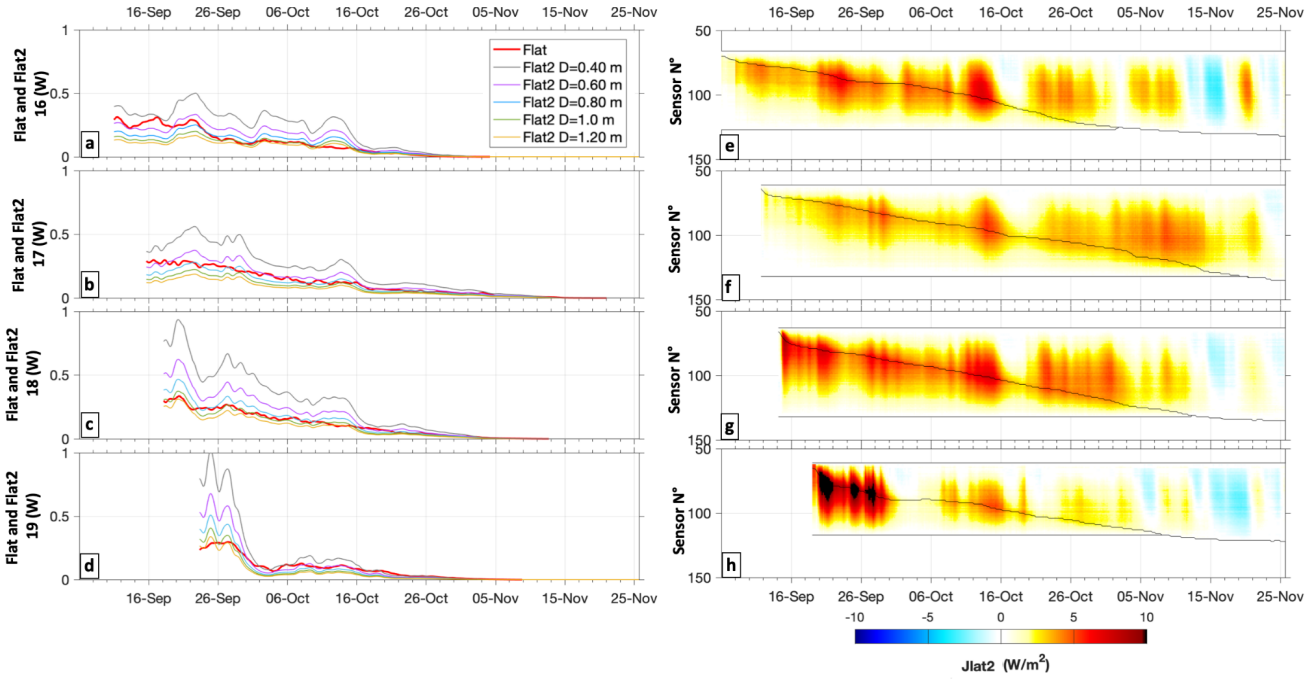

Figure 17. Lateral heat flux (W) estimated with the first method $F_{lat}(t)$ (red) and with the second method $F_{lat2}(t)$ for different distances D ranging from 0.40 m to 1.20 m for **(a)** S16, **(b)** S17, **(c)** S18, and **(d)** S19. Evolution of the lateral heat flux density (W/m^2) $J_{lat2}(t,z)$ for D=0.80 m for **(e)** S16, **(f)** S17, **(g)** S18, and **(h)** S19.

5. Conclusion-discussion

Four buoys equipped with SIMBA instruments were deployed in the Arctic in September 2015. The SIMBA chain was inserted in a hole drilled in sea ice and temperature and heated temperature (HST2) were repeatedly measured along the chain through the air, snow, ice, and ocean, during a period ranging from 3 to 9 months.

As in previous studies (Gani et al. 2019, Liao et al. 2018, Provost et al. 2017), the evolution of snow and sea ice thickness was deduced from these observations. Moreover, the vertical heterogeneity of the snow cover was investigated through the joint analysis of temperature and HST2 profiles for the first time. The snow cover proved to be stratified, displaying layers with different thermal and physical properties; the conductivity and the density of each snow layer could be estimated. The calculated snow density ranged from 260 to 380 kg/m3, which is in agreement with observations from snow pits (Merkouriadi et al., 2017; King et al., 2020). The density of the upper layer of snow was larger than the density of the intermediate layer,

which also agrees with data from direct observations (Domine et al., 2020; King et al., 2020; Shook, 1995). This study shows that autonomous instruments (SIMBAs) can provide continuous information on snow conductivity and density, which are fundamental to understanding the physical processes at work in the coupled air/snow/sea-ice/ocean Arctic system. Analysis of spring data, when the snow density tends to increase, should precise the relationship between heated temperature and snow conductivity.

Introducing a SIMBA chain induces inevitable perturbations of the system in both snow and sea ice. Just above the ice, a layer of packed/wet snow with a large density (up to 660 kg/m3) was added in the deployment hole to fill the gap between the waterline and the top of the ice. This layer was shown to persist over time and to affect the temperature at the top of the ice. This added layer of snow, whose thickness is known, does not prevent us from knowing the snow depth and ice thickness all around.

The refreezing of the deployment hole in sea ice took more than 2 months, as the air temperature is still mild in autumn (it took a few days for a deployment in January). To analyze the physical processes at stake during this period, we developed two different methods to estimate the lateral heat flux. The first one was based on an energy balance and estimated the energy necessary for the seawater in the hole to refreeze. The second one was more local and rested on an estimation of the lateral heat flux density profiles. Although based on independent hypotheses, these two methods gave similar results. The lateral heat fluxes are ten times larger than the vertical heat fluxes from the atmosphere in October and November. The heat flux density was maximum close to the freezing front (about $10\ W/m^2$ at the beginning of the refreezing). This study about lateral heat flux will be completed in the companion paper Gani et al. [2021b] using numerical modelling.

Appendix 1:

The IMB heating mode: HST1 a diffusivity proxy and HST2 a conductivity proxy

The thermal evolution of the medium (snow or ice) is characterized by the heat equation

$$\rho\, C \partial_t T = div(k\, grad\, T) \qquad (1)$$

where ρ is the medium density, C the specific heat, and k the heat conductivity. This equation completed by initial and boundary conditions provides the evolution of temperature. If the coefficients ρ , C, and k are constant, the heat diffusivity $\upsilon = k/(\rho\, C)$ is introduced and the heat equation becomes

$$\partial_t T = \upsilon\, div(\text{grad T}) \qquad (2)$$

When the heating mode is activated, the medium temperature increases by about 2 to 4°C during approximately 50 s and then stabilizes around a constant value (see for example Figures 4 and 6 in Jackson et al., [2013]).

The heating is modeled by adding a supplementary boundary condition with a heat flux $\boldsymbol{j}$ (proportional to the power furnished to the resistor) around the resistor.

$$j = -\, k\, grad\, T|_S \qquad (3)$$

where j is the heat flux density due to the heating and S is a surface depending on the geometry of the resistor.

Three temperatures are recorded during a 120s-long heating: To as heating starts, T1 in the transient state after 30 s, and T2 after stabilization at 120 s.

$HST1 = T1 - T0$ mainly depends on ν as temperature changes via the heat equation (2). Consequently HST1 provides a proxy of the diffusivity of the medium.

In contrast, $HST2 = T2 - T0$ corresponds to a quasi-stationary state ($\partial_t T \simeq 0$) and the system is governed by the equations $0 = div(k\, grad\, T)$ and $j = -\, k\, grad\, T|_S$ which only depends on conductivity. HST2 is thus a proxy of conductivity rather than a proxy of diffusivity.

Acknowledgments

We thank the crew and scientists who participated in the PS94 "TransArc II campaign. We thank Nicolas Villacieros Robineau and Jean-Philippe Savy for the IAOOS deployments. We acknowledge support from the ANR EQUIPEX IAOOS project, through ANR-10-EQPX-32-01 grant. Research funded under PhD scholarships from Sorbonne Université, Paris.

Data availability

The SIMBA data and interfaces are available at :

https://data.ifremer.fr/Deposer-Archiver-des-donnees/SEANOE

REFERENCES

Bokhorst, S., Pedersen, S.H., Brucker, L. et al. Changing Arctic snow cover: A review of recent developments and assessment of future needs for observations, modelling, and impacts. Ambio 45, 516–537 (2016). https://doi.org/10.1007/s13280-016-0770-0.

Chris Petrich, Pat. J. Langhorne, Tim G. Haskell. (2007). Formation and structure of refrozen cracks in land-fast first-year sea ice. J. Geophys. Res: Oceans, 112, https://doi.org/10.1029/2006JC003466.

Colbeck, S. C. The layered character of snow covers. Rev. Geophys. 291, 81–96 (1991).

C. Fierz, R.L. Armstrong, Y. Durand, P. Etchevers, E. Greene, D.M. McClung, K. Nishimura, P.K. Satyawali, S.A. Sokratov. The International Classification for Seasonal Snow on the Ground. IHP-VII Technical Documents in Hydrology n 83 IACS Contribution n 1 (2009)

Gani, S., Sirven, J., Sennéchael N., Provost C. Revisiting Winter Arctic Ice Mass Balance Observations With a 1-D Model: Sensitivity Studies, Snow Density Estimation, Flooding, and Snow Ice Formation. Journal of Geophysical Research. Oceans, Wiley-Blackwell, 2019, 124 (12), pp.9295-9316. ⟨10.1029/2019JC015431⟩.

Giles, K. A., Laxon, S. W., Wingham, D. J., Wallis, D. W., Kra-bill, W. B., Leuschen, C. J., McAdoo, D., Manizade, S. S., and Raney, R. K.: Combined airborne laser and radar altimeter mea-surements over the Fram Strait in May 2002, Remote Sens. En-viron., 111, 182–194, https://doi.org/10.1016/j.rse.2007.02.037,2007.

Granskog, M. A., Rösel, A., Dodd, P. A., Divine, D., Gerland, S., Martma, T., & Leng, M. J. (2017). Snow contribution to first-year and second-year Arctic sea ice mass balance north of Svalbard. Journal of Geophysical Research: Oceans, 122, 2539– 2549. https://doi.org/10.1002/2016JC012398.

Hansen, E., Gerland, S., Granskog, M. A., Pavlova, O., Renner, A. H. H., Haapala, J., et al. (2013). Thinning of Arctic Sea ice observed in Fram Strait: 1990–2011. Journal of Geophysical Research: Oceans, 118(10), 5202–5221. https://doi.org/10.1002/jgrc.20393.

Jackson, K., Wilkinson, J., Maksym, T., Meldrum, D., Beckers, J., Haas, C., & McKenzie, D. (2013). A novel and low-cost sea-ice mass balance buoy,Journal of Atmospheric and OceanicTechnology, 30, 2676– 2688. https://doi.org/10.1175/JTECH-D-13-00058.1

Kern, S., Khvorostovsky, K., Skourup, H., Rinne, E., Parsakhoo, Z. S., Djepa, V., Wadhams, P., and Sandven, S.: The impact of snow depth, snow density and ice density on sea ice thickness retrieval from satellite radar altimetry: results from the ESA-CCI Sea Ice ECV Project Round Robin Exercise, The Cryosphere, 9, 37–52, https://doi.org/10.5194/tc-9-37-2015, 2015.

King, J., Howell, S., Brady, M., Toose, P., Derksen, C., Haas, C., and Beckers, J.: Local-scale variability of snow density on Arctic sea ice, The Cryosphere, 14, 4323–4339, https://doi.org/10.5194/tc-14-4323-2020, 2020.

Kurtz, N. T. and Farrell, S. L.: Large-scale surveys of snow depth on Arctic sea ice from Operation IceBridge, Geophys. Res. Lett., 38, L20505, https://doi.org/10.1029/2011GL049216, 2011.

Kwok, Ronald & Untersteiner, Norbert. (2011). The thinning of Arctic sea ice. Physics Today. 64. 36-41. 10.1063/1.3580491.

Kwok, R., Kacimi, S., Webster, M. A., Kurtz, N. T., & Petty, A. A. (2020). Arctic snow depth and sea ice thickness from ICESat-2 and CryoSat-2freeboards: A first examination. Journal of Geophysical Research: Oceans, 125, e2019JC016008. https://doi.org/10.1029/2019JC016008.

Lecomte, O., Fichefet, T., Vancoppenolle, M., & Nicolaus, M. (2011). A new snow thermodynamic scheme for large-scale sea-ice models. Annals of Glaciology, 52(57), 337– 346.

Ledley, T. S. Snow on sea ice: competing effects in shaping climate. J. Geophys. Res. 96, 17195–17208 (1991).

Leu, E., Wiktor, J., Søreide, J. E., Berge, J. & Falk-Petersen, S. Increased irradiance reduces food quality of sea ice algae. Mar. Ecol. Prog. Ser. 411, 49–60 (2010).

Lindsay, R., & Schweiger, A. (2015). Arctic sea ice thickness loss determined using subsurface, aircraft, and satellite observations. The Cryosphere, 9, 269– 283.

Maslanik, J., Stroeve, J., Fowler, C. & Emery, W. Distribution and trends in Arctic sea ice age through spring 2011. Geophys. Res. Lett. 38, L13502 (2011).

Maykut, G. A., and N. Untersteiner (1971), Some results from a time-dependent thermodynamical model of sea-ice, J. Geophys. Res., 76, 1550–1575.

Merkouriadi, I., J.-C. Gallet, R. M. Graham, G. E. Liston, C. Polashenski, A. Rösel, and S. Gerland (2017b), Winter snow conditions on Arctic sea ice north of Svalbard during the Norwegian young sea ICE (N-ICE2015) expedition, J. Geophys. Res. Atmos., 122, doi:10.1002/2017JD026753.

Nandan, V., R. K Scharien, T. Geldsetzer, R. Kwok, J. J. Yackel, M. Mahmud, A. Rösel, R. Tonboe, M. Granskog, R. Willatt, J. Stroeve, P. Nomura, M Frey:Snow Property Controls on Modeled Ku-Band Altimeter Estimates of First-Year Sea Ice Thickness: Case Studies From the Canadian and Norwegian Arctic.IEEE Journal of Selected Topics in Applied Earth Observations and Remote Sensing13, 1082-1096, 2020.

Perovich, D. K., Grenfell, T. C., Light, B. & Hobbs., P. V. Seasonal evolution of the albedo of multiyear Arctic sea ice. J. Geophys. Res. 107(C10), 8044 (2002).

Perovich D. K., T. C. Grenfell, J. A. Richter-Menge, B. Light, W. B. Tucker III, and H. Eicken,' Thin and thinner: Sea ice mass balance measurements during SHEBA,', J. Geophys. Res., 108 (C3), 8050, doi:10.1029/2001JC001079, 2003.

Perovich, D. et al. Observing and understanding climate change: Monitoring the mass balance, motion, and thickness of Arctic sea ice. http://imb-crrel-dartmouth.org (2017b).

Petrich, C., Eicken, H., Polashenski, C. M., Sturm, M., Harbeck, J. P., Perovich, D. K., & Finnegan, D. C. (2012). Snow dunes: A controlling factor of melt pond distribution on Arctic sea ice. Journal of Geophysical Research: Oceans, 117, C09029. https://doi.org/10.1029/2012JC008192.

Provost, C., Sennéchael, N., Miguet, J., Itkin, P., Rösel, A., Koenig, Z., Villacieros-Robineau, N., and Granskog, M. A. (2017). Observations of flooding and snow ice formation in a thinner Arctic sea ice regime during the N-ICE2015 campaign: Influence of basal ice melt and storms. Journal of Geophysical Research: Oceans, 122, 7115– 7134. https://doi.org/10.1002/2016JC012011.

Ricker, R., Hendricks, S., Helm, V., Skourup, H., and Davidson, M.: Sensitivity of CryoSat-2 Arctic sea-ice freeboard and thickness on radar-waveform interpretation, The Cryosphere, 8, 1607–1622, https://doi.org/10.5194/tc-8-1607-2014, 2014.

Schneebeli, Martin & Johnson, Jerome. (1998). A constant-speed penetrometer for high-resolution snow stratigraphy. Annals of Glaciology. 26. 107-111. 10.3189/1998a0g26-1-107-111.

Spreen, G., Kwok, R., & Menemenlis, D. (2011). Trends in Arctic sea ice drift and role of wind forcing: 1992–2009. Geophysical Research Letters, 38, L19501. https://doi.org/10.1029/2011GL048970.

Sturm, M., Morris, K. & Massom, R. in Antarctic Sea Ice: Physical Processes, Interactions and Variability Vol. 74 (ed. Jeffries, M. O.) 1–18 (AGU, Washington DC, 1998).

Sturm, M., Holmgren, J. & Perovich, D. K. Winter snow cover on the sea ice of the Arctic Ocean at the Surface Heat Budget of the Arctic Ocean (SHEBA): temporal evolution and spatial variability. J. Geophys. Res. 107(C10), 8047 (2002). An observational analysis on the evolution and spatial distribution of snow on Arctic sea ice over the seasonal cycle, which concludes with recommendations for representing snow cover variations in models.

Sturm, M., Perovich, D. K. & Holmgren, J. Thermal conductivity and heat transfer through the snow on the ice of the Beaufort Sea. J. Geophys. Res. 107(C21), 8043 (2002).

Sturm, M. & Massom, R. A. in Sea Ice 3rd edn (ed. Thomas, D. N.) 65–109 (Wiley and Blackwell, Oxford, 2017).The most recent review of snow on Arctic and Antarctic sea ice.

Warren, S. G. Optical properties of snow. Rev. Geophys. 20, 67–89 (1982).

Webster, M, S Gerland, M Holland, E Hunke, R Kwok, O Lecomte, R Massom, D Perovich, and M Sturm. 2018. "Snow in the Changing Sea-Ice Systems." Nature Climate Change 8: 946-953. https://doi.org/10.1038/s41558-018-0286-7.

Yackel, J.; Geldsetzer, T.; Mahmud, M.; Nandan, V.; Howell, S.E.L.; Scharien, R.K.; Lam, H.M. Snow Thickness Estimation on First-Year Sea Ice from Late Winter Spaceborne

Scatterometer Backscatter Variance. *Remote Sens.* 2019, *11*, 417. https://doi.org/10.3390/rs11040417

Zeliang Liao, Bin Cheng, JieChen Zhao, Timo Vihma, Keith Jackson, Qinghua Yang, Yu Yang, Lin Zhang, Zhijun Li, Yubao Qiu & Xiao Cheng (2019) Snow depth and ice thickness derived from SIMBA ice mass balance buoy data using an automated algorithm, International Journal of Digital Earth, 12:8, 962-979, DOI: 10.1080/17538947.2018.1545877

Zygmuntowska, M., Rampal, P., Ivanova, N., Smedsrud, L.H., 2014. Uncertainties in Arctic sea ice thickness and volume: new estimates and implications for trends. Cryosphere 8, 705e720. http://dx.doi.org/10.5194/tc-8-705-2014.

Modélisation numérique de la neige et de la glace de mer : conductivité de la neige et flux latéraux dans la glace.

Sommaire

5.1 Résumé

Les simulation numériques réalisées à partir de modèle unidimensionnel de glace de mer permettent de confirmer des estimations effectuées à partir des observations, d'analyser des processus physiques et de tester de nouvelles paramétrisation.

Dans cette étude, des simulations numériques sont réalisées avec le modèle unidimensionnel LIM1D. On essaie de reproduire le mieux possible les 4 séries d'observations décrites dans le chapitre 4, non seulement pour vérifier que les estimations obtenues à partir de l'analyse directe des observations ne sont pas erronées mais aussi pour déterminer leur impact sur la modélisation numérique. Tout d'abord, le modèle a été adapté (en introduisant 10 couches de neige) pour tenir compte d'une couverture neigeuse stratifiée. De plus, un terme de flux latéral a été ajouté dans l'équation de diffusion de la chaleur afin de représenter les flux latéraux mis en évidence dans les observations. Cela a nécessité de développer une paramétrisation de ce flux.

En utilisant les densités de neige obtenues par l'analyse des observations, le modèle simule l'évolution des profils de température dans la neige et la glace avec une précision satisfaisante pour l'étude des processus, et ce tout au long de la dérive. On montre également que lorsque la conductivité équivalente du manteau neigeux est correcte (bien que la stratification ne le soit pas forcément), l'évolution de l'épaisseur de glace l'est aussi. Mais dans ce cas, le profil de température dans la neige peut être très biaisé. Pour obtenir ce dernier, il est indispensable de représenter la neige par plusieurs couches de conductivité et densité différentes.

La cinétique du rebouchage du trou et la contribution du flux latéral par rapport au flux vertical atmosphérique ont également été évaluées en comparant les simulations numériques aux observations. La qualité des simulations a permis de confirmer la méthode d'estimation du flux latéral responsable du transfert de chaleur entre l'eau de mer dans le trou de déploiement et la glace environnante.

Ce chapitre est un article conjoint au chapitre 4, également en voie de soumission dans le *Journal of Geophysical Research.*

Estimating snow stratification, snow conductivity, and sea ice lateral heat flux from temperature profiles provided by ice mass balance instruments.
Part II: Numerical modeling assessment

S Gani, J. Sirven, N. Sennéchael, and C. Provost.

IPSL/LOCEAN/UPMC/CNRS/IRD/MNHN

Sorbonne Université, Paris, France

Key points:

- The snow cover stratification is represented with a multilayer scheme introduced in the LIM1D model.
- Snow conductivity estimates coming from observations provide correct modeled sea ice growth evolutions.
- The refreezing of the deployment hole is simulated and the lateral heat flux density estimated using a simple parameterisation.

Abstract

Temperature and heated temperature profiles were measured by four SAMS ice mass balance instruments (SIMBA) through air, snow, sea ice and ocean between September 2015 and May 2016. Numerical experiments with a state-of-the-art one-dimensional snow and ice model (LIM1D) are performed to simulate the evolution of these temperature profiles in snow and ice. The model has been modified in order to introduce a stratified snow cover, using the snow conductivity and density previously estimated from the observations. The simulations are in good agreement with the observations and the root-mean-square difference between simulated and observed temperature profiles in sea ice is around 0.5°C. The complete refreezing of seawater in deployment holes needed more than two months. To correctly represent it, a parameterisation of the lateral heat flux is added to the LIM1D model through the heat diffusion equation. This gives an estimate of the lateral heat flux, which compares well with that obtained from observations. Without this term, the model is no longer able to reproduce the observed processes.

Plain language summary

Sea ice mass balance instruments drifted in the Arctic ice pack from September 2015 and recorded repeated temperature profiles in air, snow, sea ice, and ocean. One-dimensional numerical experiments, which simulate the temperature profiles in snow and ice, support the snow density estimates previously obtained by observational analysis. The refreezing of seawater in the deployment hole is simulated by adding a lateral heat flux term to the heat diffusion equation. The estimates of these fluxes are also in good agreement with those obtained from the observations.

1. Introduction

Sea ice and snow are essential components of the heat budget in a changing Arctic (Skyllingstad & Polashenski, 2018, Semmler et al., 2012). Sea ice acts as a thermal reservoir due to the large value of the latent heat of fusion, while snow regulates the energy transfer between atmosphere, sea ice and ocean, through its thermal (conductivity), physical (density), and optical (albedo) properties (Bokhorst et al., 2016; Blazey et al., 2013; Pedersen and Winther, 2005; Sturm et al., 2002a). It is essential to better represent the snow properties and their spatiotemporal variability to understand the physical processes at stake in the Arctic system (Merkouriadi et al., 2017) .

Various snow models exist, with different levels of complexity. Even if complex snow models such as SNOWPACK (Bartelt and Lehning, 2002) and Crocus (Vionnet et al., 2012) include a multilayer snow scheme (computationally expensive), the simulated snow density profiles are not completely realistic (Barrere et al., 2017). Simplified snow schemes are used in the majority of climate models (Decharme et al., 2016; Chadburn et al., 2015; Paquin & Sushama, 2015; Burke et al., 2013; Dutra et al., 2012; Lawrence & Slater, 2010). Snow properties such as albedo, conductivity, density, and grain size are commonly set constant in a single snow layer at the top of the ice (Massonnet et al., 2011; Hunke et al., 2010; Pedersen and Winther, 2005). This offers a convenient way to reproduce the Arctic snow depth at large scale (Lecomte et al., 2015; Castro-Morales et al., 2017). Studies based on observations estimated that three to four layered models could describe the vertical variability of the snow properties (eg. density) over the Arctic sea ice (Gallet et al., 2017). Lastly, one-dimensional snow and sea ice models provide efficient tools for testing parameterizations of small-scale physical processes within sea ice and snow and for interpreting field observations. They also give access to variables that cannot be measured continuously (Vancoppenolle and Tedesco, 2017, Lecomte et al. 2011). These models require an adequate representation of snow depth and conductivity to correctly represent the temperature profiles in snow and sea-ice and the sea ice growth.

In a companion paper, we analyzed high-resolution observations provided by four SAMS ice mass balance instruments (SIMBA) (Jackson et al., 2013). Snow and sea ice thickness evolution were determined from the analysis of temperature profiles, and the snow cover stratification was also investigated. A method was developed to estimate the conductivity and density of the different snow layers, directly from the observations. The kinetics of the refreezing in the deployment hole and estimations of the lateral heat fluxes from temperature profiles were also investigated.

In this study, simulations are performed with a state of the art snow and sea ice one dimensional model (the model LIM1D, see Vancoppenolle et al.,2008, 2010) to (1) confirm the estimates of the snow density obtained in Gani et al., [2021a] and measure the impact of the introduction of a multilayer snow system on the evolution of the ice characteristics. We also (2) compute the lateral heat fluxes in the deployment hole, evaluate their contribution to its refreezing, and compare them to those estimated in the companion paper. The model has been modified to achieve these two objectives.

The paper is organized as follows. Section 2 briefly describes the model, with a focus on the points which differ from the standard version of LIM1D. The reference experiments corresponding to the four SIMBAs are presented in section 3. In section 4, we show some sensitivity experiments to the snow density and to the lateral heat flux estimations. Finally, section 5 summarizes the results and provides perspectives.

2. The LIM1D model

From initial conditions, the state of the art LIM1D model solves the heat equation in snow and sea ice and a supplementary advective-diffusive equation for the salt in sea ice (see Bitz and Lipscomb [1999] and Vancoppenolle et al., [2007], [2010], [2017]). The modeled evolution of the temperature profiles in snow and sea ice are compared with the SIMBA high-resolution observations. This comparison gives an assessment of the quality of the simulations. Other quantities inaccessible to direct measurement such as brine fraction, conductivity and salinity in sea ice are also estimated. In the following, we summarize the

main characteristics of the LIM1D model and detail new developments compared to the model used in Gani et al. [2019].

2.1 Modeling of the snow cover

In a companion paper, we analyzed temperature profiles from four SIMBAs (hereafter S16, S17, S18, and S19) which drifted with the Arctic ice pack during 3 to 9 months (see Figure 1 in Gani et al., 2021a). Snow depth, snow stratification and the mean density of the different snow layers were estimated from temperature and heated temperature (hereafter HST2) profiles. Here, 10 layers of snow were introduced in the model to take into account the vertical heterogeneity of the snow cover. At each 1h-time step, the model distributes the thicknesses of the 10 snow and 20 ice layers in such a way that the enthalpy of the system is conserved (Figure 1).

The initial conditions used for the reference experiments are specified in Table 1. The snow densities come from Gani et al. [2021a]. For series S17 and S18, the snow thickness varies as described in Gani et al. [2021a]. At S16 site, the chain support collapsed on September 24 and the snow thickness has been kept constant after this date (0.37 m). For S19, the chain support collapsed on January 2 and observations suggested an increase in snow depth (Figure 5 in Gani et al. [2021a]). From this date, the snow depth was set to 0.60 m until the end of the drift, which gave the best simulation (see section 3).

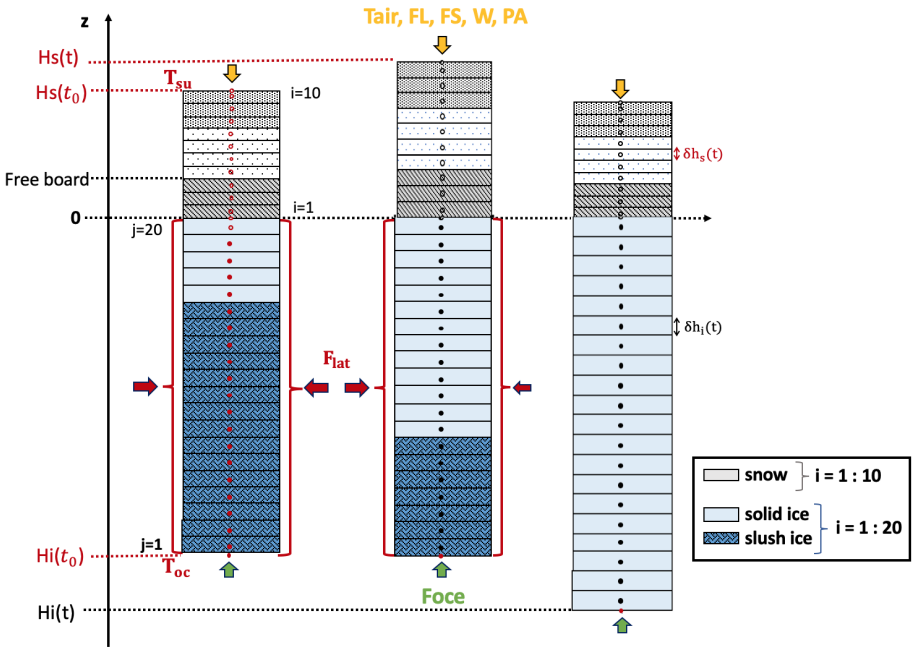

Figure 1. Schematic of the model. The snow cover is represented with ten layers of equal thickness $\delta h_s(t)$ and the sea-ice with twenty layers of thickness $\delta h_i(t)$. Red (respectively black) items correspond to prescribed (calculated) values. H_s: snow thickness, H_i: ice thickness, Tair: air temperature, FL: longwave flux, FS: shortwave flux, W: wind, PA: sea level pressure, Foce: ocean flux. T_{Su}: snow surface temperature, T_{OC}: ocean temperature.

2.2 Lateral flux parameterization

To deploy a SIMBA, a chain is inserted into a 5 cm diameter hole drilled in the ice. The complete refreezing of these holes took more than 2 months, as evidenced by the heated temperature profiles and the location of the freezing front (Figures 2 and 4 in Gani et al., 2021a). Studies made on cracks showed that they freeze in two dimensions, from the top to the bottom due to the vertical heat transfer to the atmosphere, and horizontally, due to the lateral heat transfer to the surrounding sea ice (Petrich et al., 2007). As the diameter of the hole is smaller than the distance considered in Petrich et al., [2007], we do not try to reproduce the arch-shaped described by these authors; however the lateral flux cannot be neglected and thus have been introduced in the LIM1D model. A supplementary term has been added in the heat diffusion equation for the ice when the hole is refreezing. This equation then reads:

$$\rho C_p \partial_t T = \partial_z (k \partial_z T) + I_0 \kappa e^{-\kappa z} + \frac{2}{R} (k \partial_\rho T|_R) \quad (4)$$

where ρ is the ice density, C_p the specific heat, k the ice conductivity, I_0 the radiation transmitted at the top of the sea ice, and κ the extinction coefficient. The last term in equation (4) models the heat flux at the boundary between the hole and the surrounding solid ice (Figure 2).

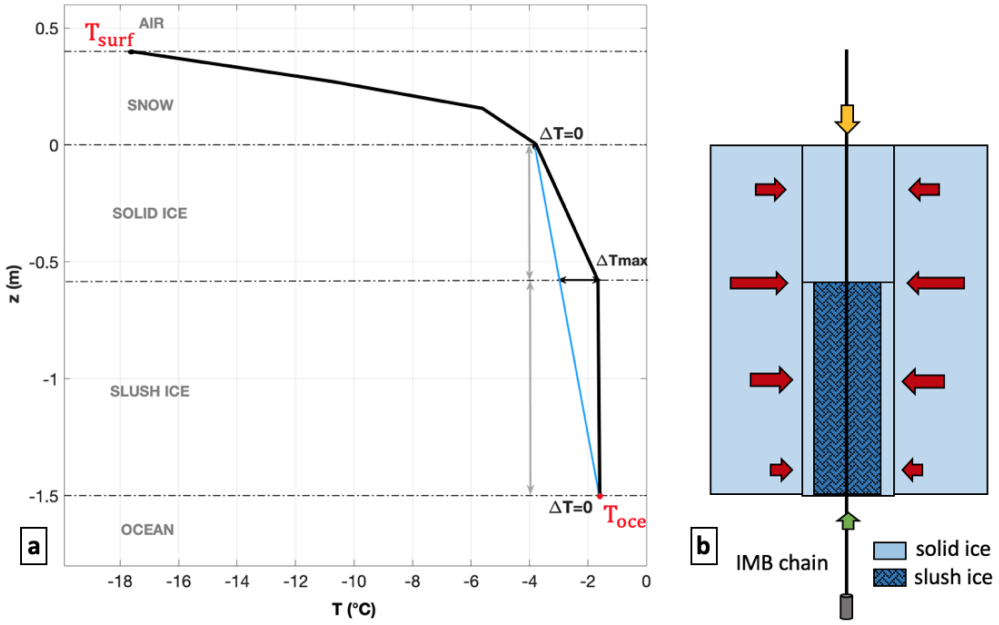

Figure 2. Schematic of the computation of the lateral heat flux density. **(a)** Modeled temperature profile (black) on October 1st for S17. The temperature profile in the surrounding ice (blue) is assumed to be linear. **(b)** The sketch shows the three heat flux densities contributing to the refreezing of the deployment hole: $F_1(t)$ through the top of the hole (yellow), $F_2(t)$ through the side wall (red), and $F_3(t)$ through the bottom of the hole (green).

The lateral heat flux density is estimated as in Gani et al., [2021a]. We assume that the temperature profile in the surrounding ice is linear, and increases from an interface temperature just below the snow up to a bottom temperature fixed by the underlying ocean (Figure 2). This reads

$$T_{sur}(z,t) = \frac{(h_i(t)-z)T_i(t) + z\,T_{oce}(t)}{h_i(t)} \quad (5)$$

where $h_i(t)$ is the ice thickness; $\partial_\rho T_R$ is then computed as a simple finite difference

$$\partial_{\rho} T_R(z,t) = \frac{T_{sur}(z,t) - T(z,t)}{D} \quad (6)$$

where D is a typical distance used to characterize the radial derivative $\partial_{\rho} T_R$, and $T(z,t)$ is the temperature in the deployment hole. When z is larger than the depth of the refreezing front at the top of the slush ice in the hole (Figure 2), the numerator gives an estimation of the difference between the temperature in the freezing hole and the temperature in the surrounding ice at the same depth. With these approximations, the last term in equation (4) becomes

$$\frac{2}{R}(k\partial_{\rho} T_R) \simeq \frac{2k}{RD}\left(T(z,t) - T_i(t) + \frac{(T_{OCE}(t) - T_i(t))z}{h(t)}\right) \quad (7)$$

This estimation requires a unique unknown parameter D whose order of magnitude defines the distance over which the impact of the deployment hole on the surrounding sea ice temperature was measurable.

3. Reference experiments

3.1 Forcing terms

The conditions needed to force the model are presented in Figure 3. The air temperature and the atmospheric pressure are available with a 1h resolution from the central unit of the buoy on which the SIMBAs were installed. The long-wave flux FL, the short-wave flux FS, the wind speed at 10 m, and the atmospheric pressure PA come from the global reanalysis ERA-Interim (ERA-I), with a 6h resolution (Dee et al., 2011). The ocean heat flux *F*OC is computed after the refreezing of the hole from the sensible heat flux and the sea ice growth rate (Provost et al., 2017). All the series have been linearly interpolated to match the one hour time step of the model. For the four SIMBAs, the air temperature ranged from -42°C to -1°C and exhibited daily variations in addition to a cold trend until December 25 (Figure 3a). Air temperature varied almost in the same way for the S16, S17, and S18 series whereas the S19 series (which was not in the same region) exhibited strong heat bursts absent from the other three series (for example on November 5 and November 16, Figure 3a). The S19 air temperature increased from late March, from -30°C to nearly 0°C by late May (Figure 3a).

During the drift of the buoys, the longwave flux ranged between 120 W/m² and 300 W/m², its variations being correlated with those of the air temperature (Figure 3b). Because of the polar night, the short wave flux FS was null until mid March, then increased up to about 300 W/m² in May (buoy S19). The wind speed averaged 5 m/s, but sometimes showed short peaks up to 15 m/s (Figure 3d). A decrease of atmospheric pressure is generally associated with an increase in air temperature and wind speed (for example in mid-March, Figure 3e). After the refreezing of the deployment hole, the ocean heat flux varied between -30 and 20 W/m² (Figure 3f).

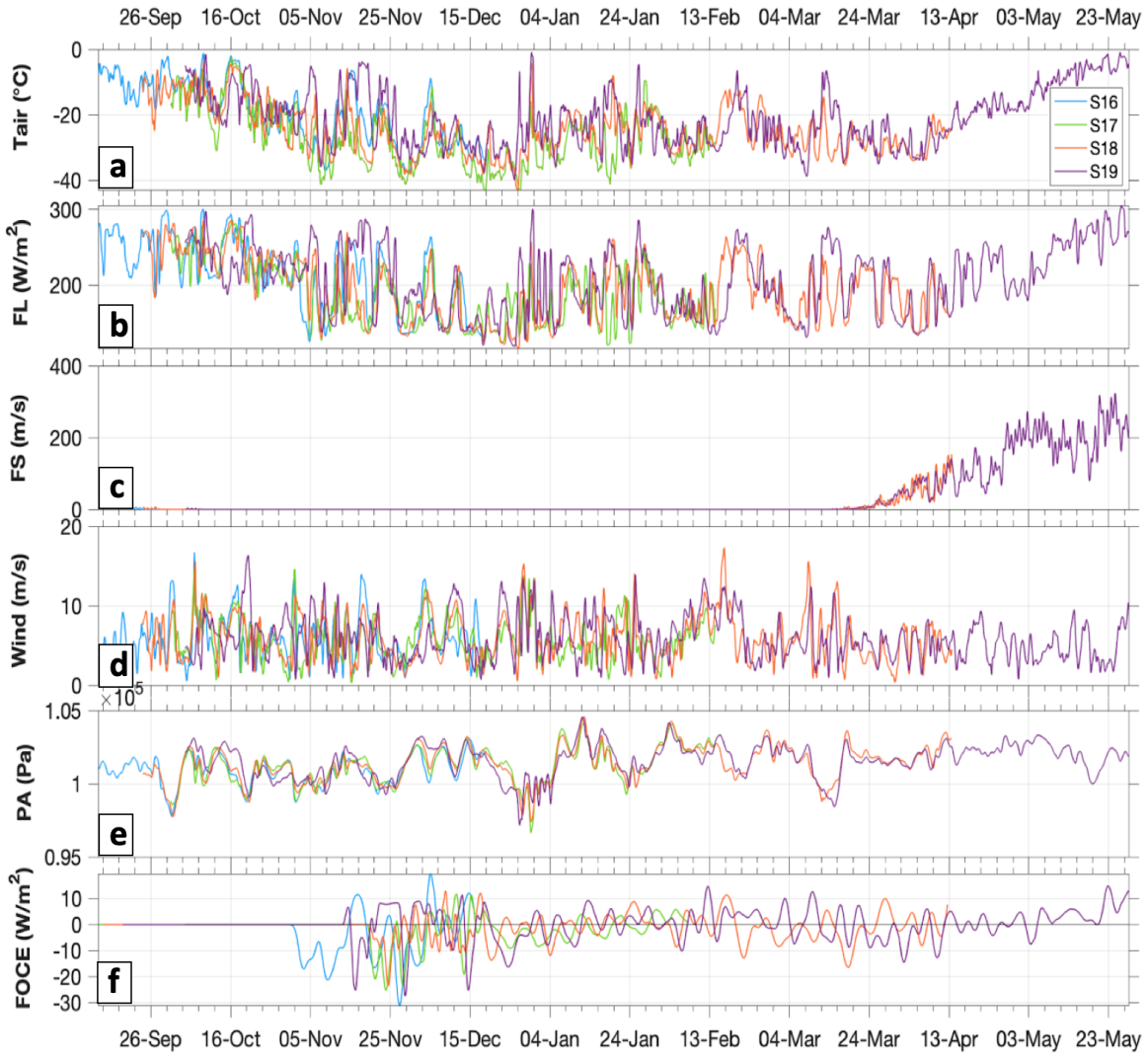

Figure 3. Time series of the forcing terms for the four SIMBAs: **(a)** Central unit air temperature (°C) **(b)** ERA-I longwave flux (W/m²) **(c)** ERA-I shortwave flux (W/m²) **(d)** ERA-I wind speed (m/s) **(e)** Central unit air pressure (Pa) **(f)** Computed oceanic heat flux (W/m²). All the series have been interpolated to fit the 1 hour time step of the model.

3.2 Initial conditions

The simulations start after the first snow accumulation at the beginning of the drifts and when the solid ice thickness is larger than 20cm (Table 1). The reference runs were initialized with the observed snow depths, sea ice thicknesses, and temperature profiles (Table 1). The initial snow thicknesses ranged from 0.30 m (S19) to 0.40 m (S17), and the solid ice thickness from 0.21 m (S16) to 0.52 m (S19). The mixture of sea water and ice in the hole (slush ice) is modeled as sea ice with a large bulk salinity, increasing from 10 psu at the solid-ice/slush interface to 25 psu at the slush/ocean interface. The bulk salinity was initialized at 4 psu for the solid ice, which corresponds to a brine fraction of 5% ; above this value, the brine pockets are connected and sea ice becomes permeable (Golden et al., 1998). The initial salinity profile has been chosen after several tries since observations are lacking. The snow specific heat is set to 2062 J/kg/K and the ice density to 917 kg/m ^{3} .

	Deployment date	Simulation Date	Snow thickness (m)	Solid ice thickness (m)	Slush ice thickness (m)	Snow layer	Density kg/m3
SIMBA 16	Sept 5	Sept 13	0.34	0.21	1.25	1 to 4	590
						5 to 10	335
SIMBA 17	Sept 11	Oct 1	0.40	0.50	1.0	1 to 3	530
						4 to 6	289
						7 to 10	304
SIMBA 18	Sept 14	Sept 24	0.36	0.40	1.04	1	600
						2 to 10	380
SIMBA 19	Sept 19	Oct 4	0.30	0.52	0.65	1 to 10	360

Table 1. Date of the beginning of the numerical experiments (date), initial snow, solid-ice, and slush-ice thickness, and the snow densities for each model layer (numbered from 1 to 10, see Figure 1) for the reference simulations of the four SIMBAs.

3.3 The reference runs

Figures 4-7 show the evolution of observed temperature, modeled temperature, differences between these two fields in snow and ice, as well as the evolution of salinity in ice for each reference run. For the four SIMBAs, the temperature profiles in snow, sea ice, and slush are in good agreement with the observations (Figure 4-7, panels a and b). The root mean square difference (RMSD) between the observed and simulated temperature in snow is between 1.3 °C (series S18) and 1.8°C (series S19) (Table 2). The temperature differences (panel c) in snow are maximum close to the snow/air interface, suggesting atmospheric fluxes as a possible source of inaccuracy (Gani et al., 2019). For series S16 and S19, our partial knowledge of the snow depth, which could not be calculated after the failure of the supports (see section 2.2) is a potential source of miscalculation. Small differences are observed at times, at the interface between two layers with distinct densities.

In solid ice, the RMSD is smaller than in the snow, between 0.4 °C for S17 and 0.7 °C for S18. Simulated temperature is slightly colder (less than 2°C) than the observed one when sea water in the hole is still refreezing (panel c). After the refreezing of the hole, the maximal temperature difference between simulation and observation are located at the snow/ice interface and decrease downwards. The modeled evolution of the sea ice thickness matches the observed one; for the four SIMBAs, differences never exceed 5 cm during the simulation.

The refreezing of the hole is well simulated : the progression of the freezing front is in agreement with the observations and the temperature difference between observations and simulations below the solid ice never exceeds 0.4 °C for the four SIMBAs.

The simulation also provides insights on the evolution of properties that cannot be measured continuously : the bulk salinity (Figure 4d-7d), the brine fraction (relative volume of salty water in the ice), and the conductivity of sea ice (not shown). When the ice forms in the hole, the salt rejected below the ice/slush interface percolates and reaches the ocean. At the end of the simulation, approximately 70% (respectively 90%) of the simulated sea ice has a bulk salinity below 4 psu (5 psu) and a brine fraction below 5% (10%), which is the

threshold at which brine pockets are isolated and sea ice is no longer permeable (Golden et al. [1998]).

The good agreement between observations and simulations for the four SIMBAs supports the estimates of snow density made in Gani et al. [2021a]. A sensitivity experiment to the snow density is described in section 4 to emphasize the importance of accurately representing the stratification of the snow cover.

RMSD (°C)	S16	S17	S18	S19
snow				
reference run	1.5	1.7	1.3	1.8
sensitivity test	2.8	2.2	1.5	1.9
sea ice				
reference run	0.5	0.4	0.7	0.4
sensitivity test	0.8	0.6	1.2	0.6

Table 2. Root-Mean-Square Difference between the observed and simulated temperature in snow and ice for the reference runs.

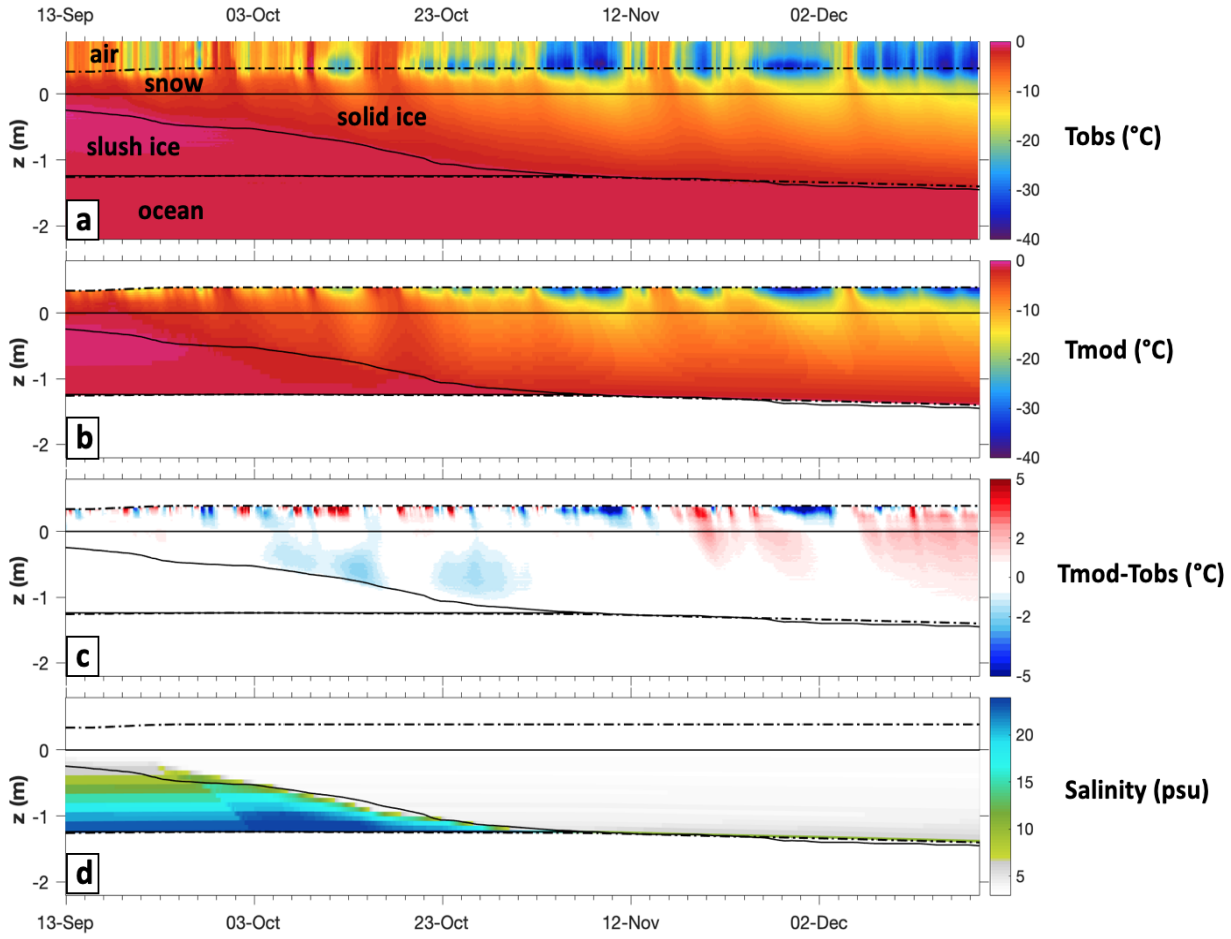

Figure 4. Reference run for S16. As a function of time: **(a)** Observed temperature in air, snow, ice, slush, and ocean (°C) **(b)** Simulated temperature in snow and ice, and slush (°C). **(c)** Temperature differences between simulation and observations (°C). Model outputs are interpolated to the vertical resolution of the data (2 cm). **(d)** Simulated salinity (psu). Dotted lines correspond to the modeled interfaces and solid lines to the observed ones.

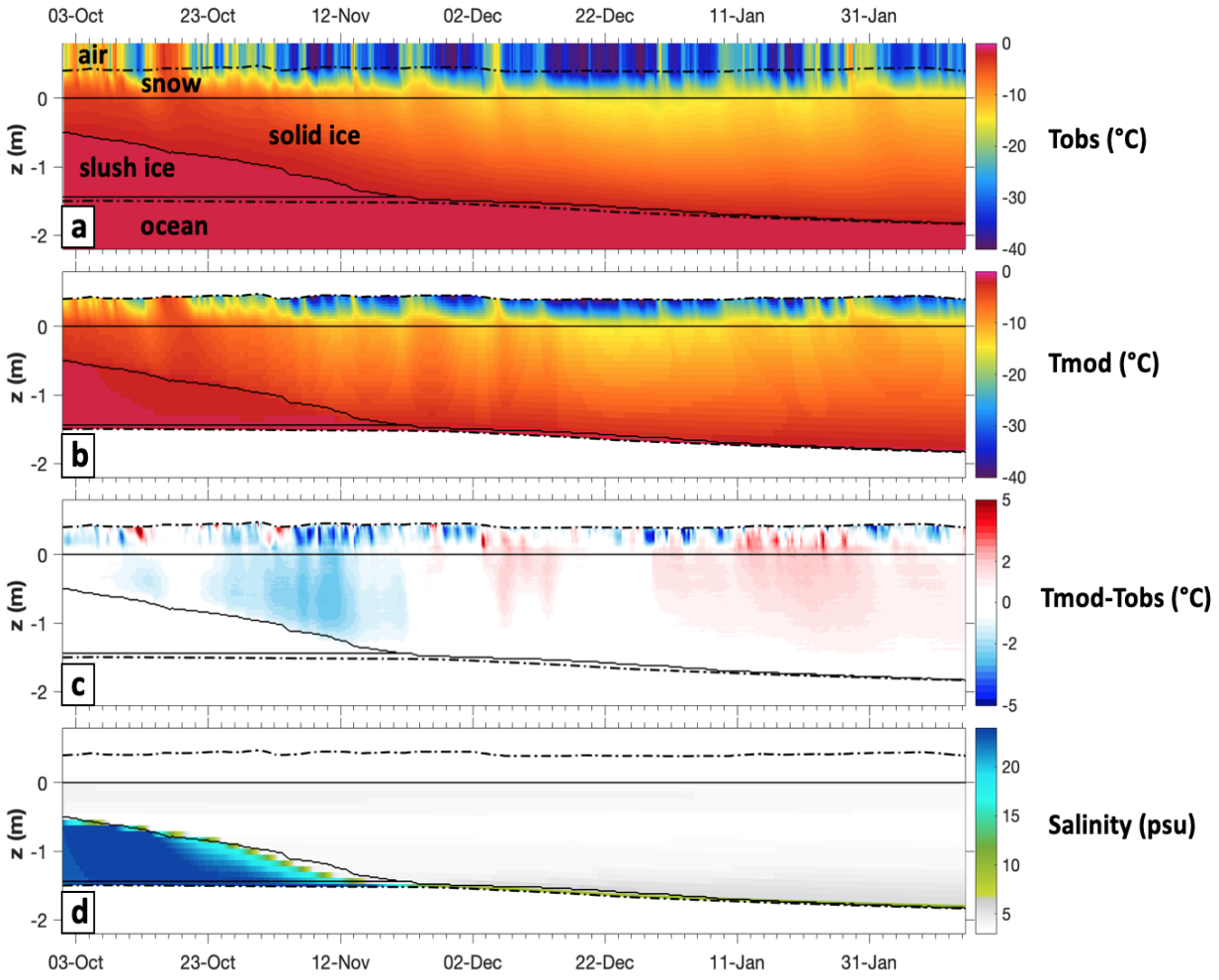

Figure 5. Reference run for S17. As a function of time: **(a)** Observed temperature in air, snow, ice, slush, and ocean (°C) **(b)** Simulated temperature in snow and ice, and slush (°C). **(c)** Temperature differences between simulation and observations (°C). Model outputs are interpolated to the vertical resolution of the data (2 cm). **(d)** Simulated salinity (psu). Dotted lines correspond to the modeled interfaces and solid lines to the observed ones.

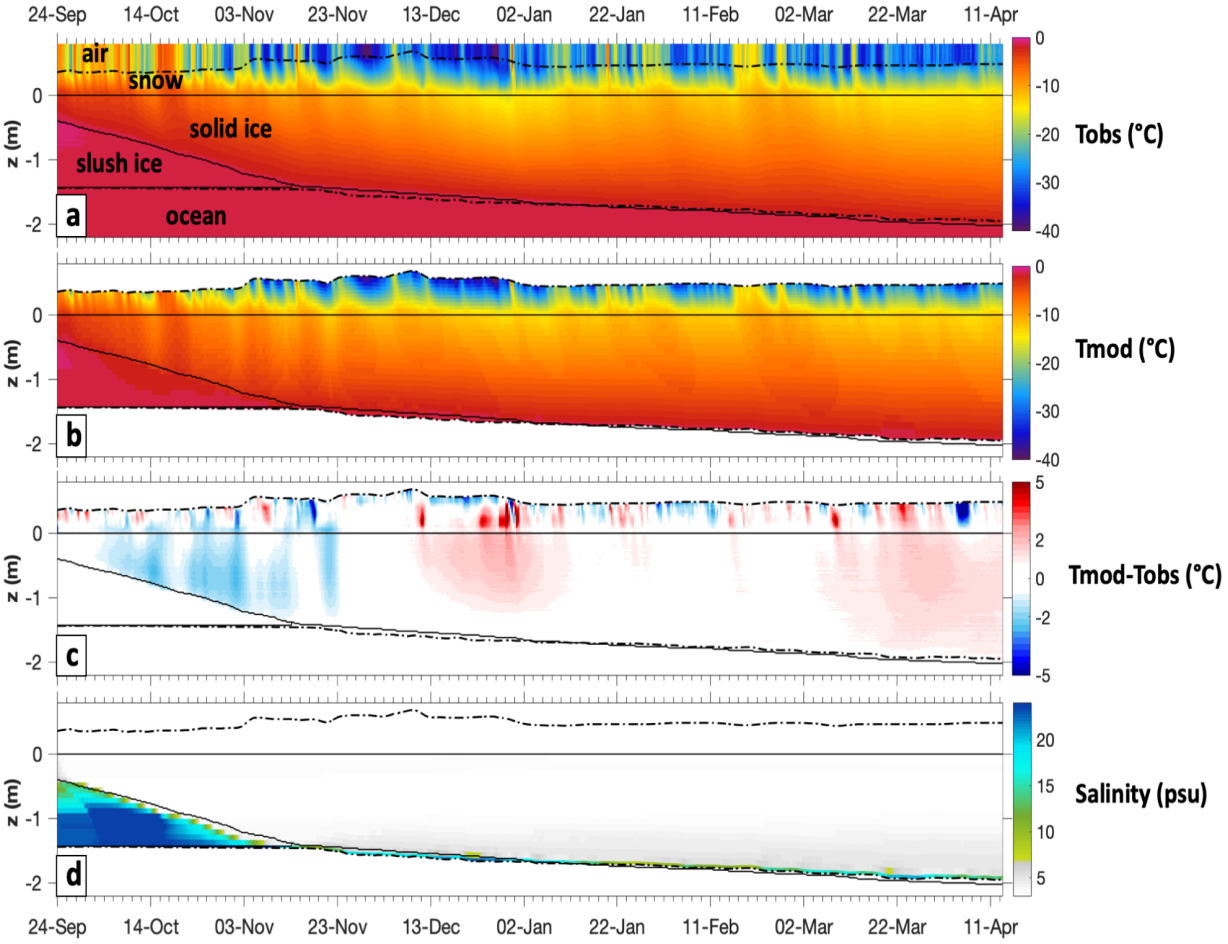

Figure 6. Reference run for S18. As a function of time: **(a)** Observed temperature in air, snow, ice, slush, and ocean (°C) **(b)** Simulated temperature in snow and ice, and slush (°C). **(c)** Temperature differences between simulation and observations (°C). Model outputs are interpolated to the vertical resolution of the data (2 cm). **(d)** Simulated salinity (psu). Dotted lines correspond to the modeled interfaces and solid lines to the observed ones.

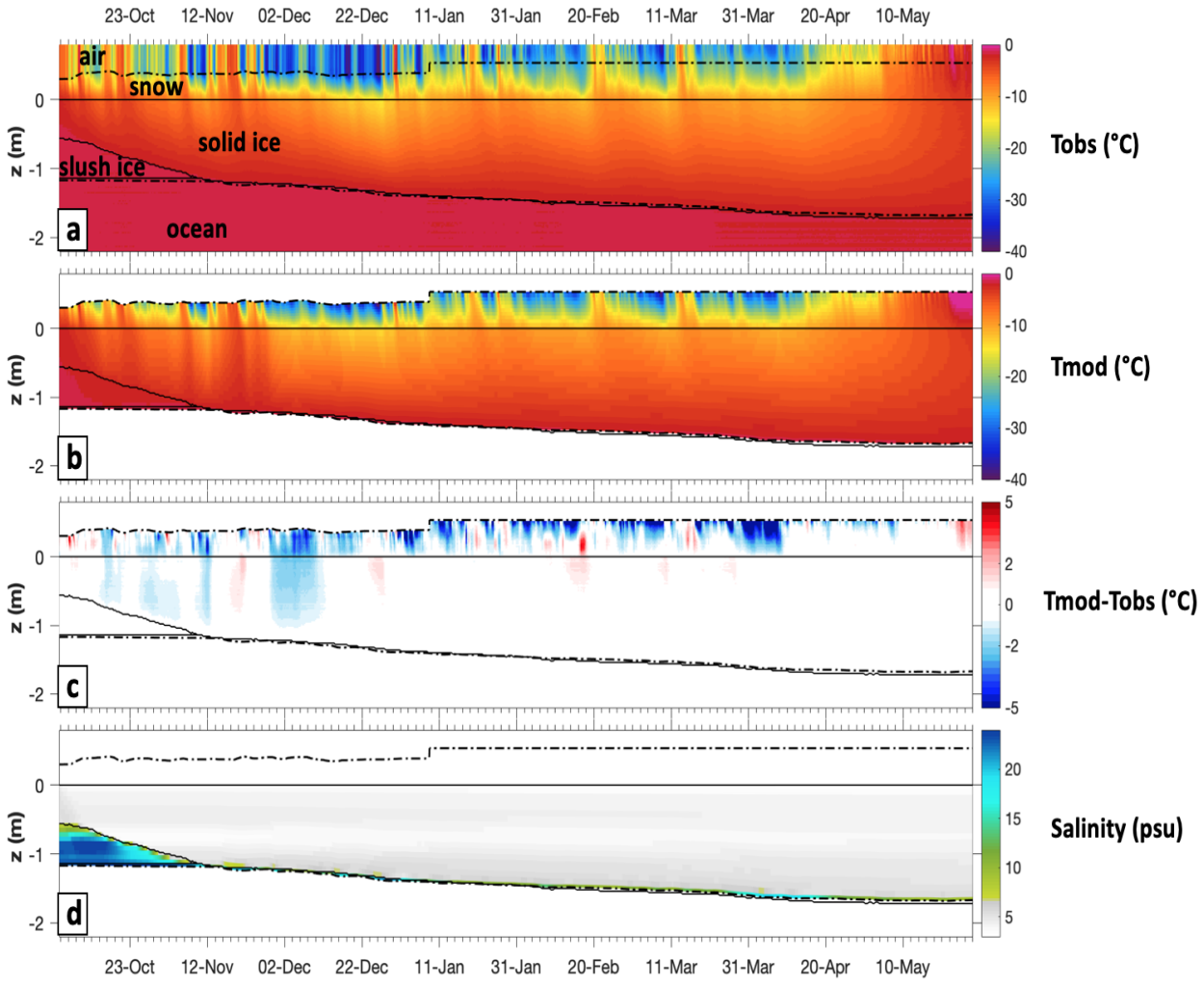

Figure 7. Reference run for S19. As a function of time: **(a)** Observed temperature in air, snow, ice, slush, and ocean (°C) **(b)** Simulated temperature in snow and ice, and slush (°C). **(c)** Temperature differences between simulation and observations (°C). Model outputs are interpolated to the vertical resolution of the data (2 cm). **(d)** Simulated salinity (psu). Dotted lines correspond to the modeled interfaces and solid lines to the observed ones.

3.4 Close up on the lateral heat flux density

The profiles of the modelled lateral heat flux density are shown in Figure 8 for the four SIMBAs. We recall that the lateral heat flux is set to zero after the refreezing of the hole. When the hole has completely frozen, the heat flux density can still be calculated using the previous assumption (linearity of the temperature profile in the surrounding ice). In this case the result of the calculation provides the heat flux density corresponding to the difference between a linear profile and the actual profile. It yields an estimate of the lateral heat flux density uncertainty inherent to the method (less than 1 W/m^2). It is zero if the quasi-stationary hypothesis is verified.

Experiments were performed varying the D coefficient (see equation (7)); the optimal values chosen for the reference simulations were found between 0.80 to 1.20 m (depending on the series), in the value range estimated from the observations. The lateral flux density is maximal at the ice/slush interface (peaking to 5 W/m^2), where $\Delta T$is maximum, and decreases down to zero towards the slush/ocean and ice/snow interfaces, where $\Delta T = 0$ (Figures 8 and 2). When the air temperature increases (October 16, Figure 8), ΔTdecreases and, consequently, the lateral heat flux density decreases too.

The kinetics of the refreezing in the hole is similar to the observed one: indeed, the maxima of the simulated heat flux densities are located on or close to the ice/slush interface deduced from the observations. The quasi-stationarity assumption involved in equation (7) provides reasonable estimates of the lateral heat flux density.

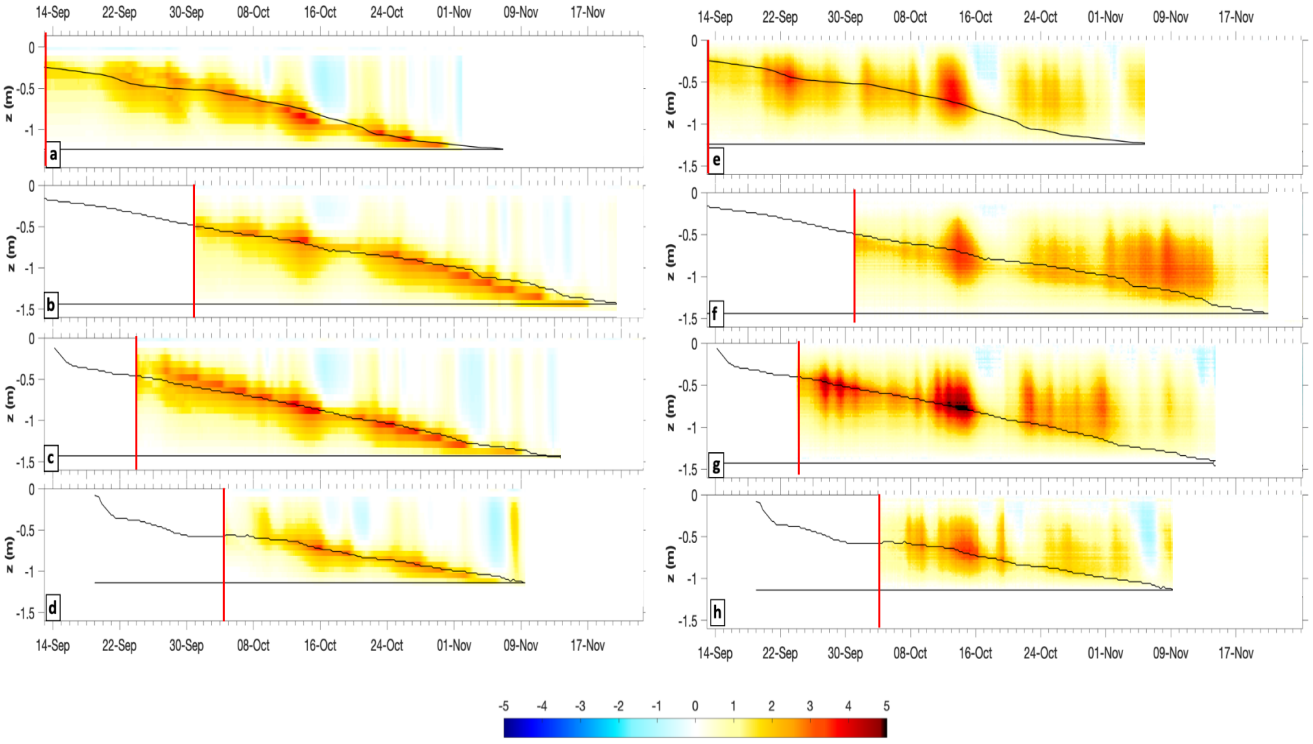

Figure 8. Evolution of the lateral heat flux density (in W/m^2) computed with the simulated temperature profiles for **(a)** S16, **(b)** S17, **(c)** S18, and **(d)** S19. Evolution of the lateral heat flux density (in W/m^2) computed with the observed temperature profiles for **(e)** S16, **(f)** S17, **(g)** S18, and **(h)** S19. On all the panels, black lines correspond to the observed ice/slush and slush/ocean interfaces.

4. Sensitivity experiments

Sensitivity experiments were carried out to investigate (1) if the snow density estimates based on the observations lead to better simulations and (2) if the addition of the lateral flux is essential to correctly simulate the observations.

4.1 Constant snow density

Simulations were performed using a constant snow density of 330 kg/m^3 and a conductivity of 0.31 W/m/K, which corresponds to common value used in modelling studies (e.g., Castro-Morales et al., 2015, Lecomte et al., 2013).

For S16, S18 and S19 series, using a constant snow density degraded the simulation in both snow and ice (Table 2). Figure 9b shows the temperature difference between the simulated and observed temperature for S18, where the RMSD in ice is now 1.20 °C. The temperature difference between the two simulations (Figure 9c) is close to zero at the air/snow interface

since the temperature of the upper snow layer is mainly driven by the atmospheric conditions. The conductivity associated with the total insulating capacity of the snowpack is 0.31 W/m/K (0.44 W/m/K for the reference run, Table 3). The snow layer is thus more insulating than in the reference run and the temperature at the snow ice interface is larger (around 3 °C, Figure 9a, c). This heat diffused through the ice, leading to a temperature difference of 2 °C at 1 m depth. From January 2, the ice thickness obtained using a constant density is smaller than the observed one (Figure 9b). At the end of the simulation (after more than 3 month), the simulated sea ice thickness is 20 cm smaller than the observed one. S16 and S19 series give similar results (not shown, see Table 3).

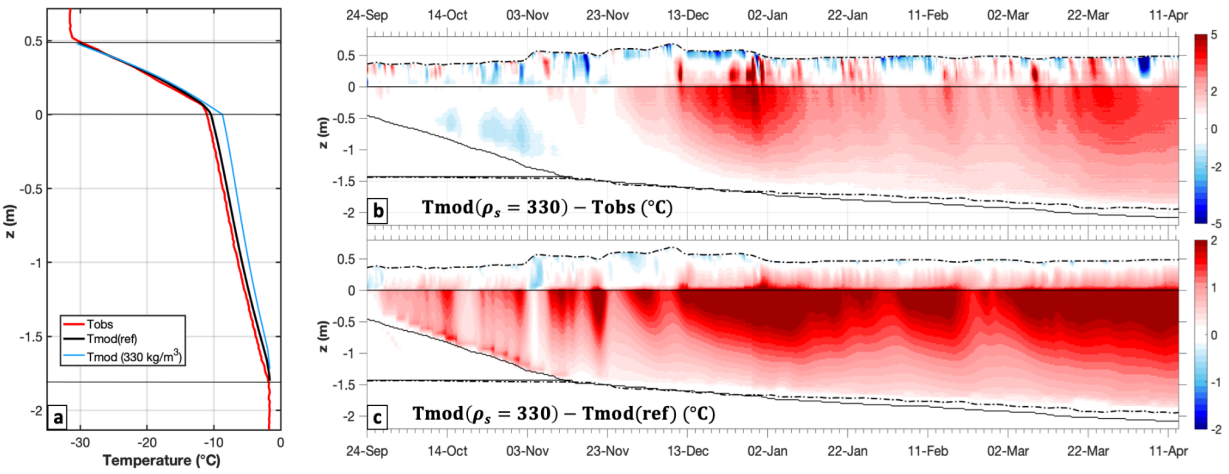

Figure 9. For S18: **(a)** Observed temperature profile (red), reference modeled temperature (black) and modeled temperature using a constant snow density (blue) on December 22 (°C). **(b)** Temperature differences between simulation using a constant snow density of 330 kg/m³ and observations (°C) **(c)** Temperature difference between the simulation using a constant snow density and the reference simulation (°C). Dotted lines correspond to the modeled interfaces and solid lines to the observed ones. Model outputs are interpolated to the vertical resolution of the data (2 cm).

The case of S17 looks paradoxical. The use of a constant snow density (hence conductivity) instead of 3 different densities distributed in ten layers degrades the simulation in snow but its impact on ice is limited (Figure 10): the RMSD between the observed and simulated temperature is 2.2°C in the snow and 0.6°C in the ice. The snow temperature is colder than that obtained in the reference run (around 3 °C, Figure 10c). The differences are maximum

above the snow/ice interface, where the snow density was around 530 kg/m³ in the reference run, but the temperature at the snow-ice interface is almost equal to the temperature obtained in the reference experiment (Figure 10a). This paradox can be explained : the snow conductivity corresponding to a constant density of 330 kg/m³ (ks = 0.31 W/m/K) is very close to the equivalent conductivity associated with the 3 layers of different density used in the reference run (0.32 W/m/K, Table 3). Sea ice temperature is thus well simulated and leads to a sea ice thickness in good agreement with observations (Figure 10b). This result agrees with those of Domine et al., [2019], who show that the ground temperature is correctly estimated if the total insulating capacity of the snowpack is well represented but the layering of thermal snow conductivity is ill represented.

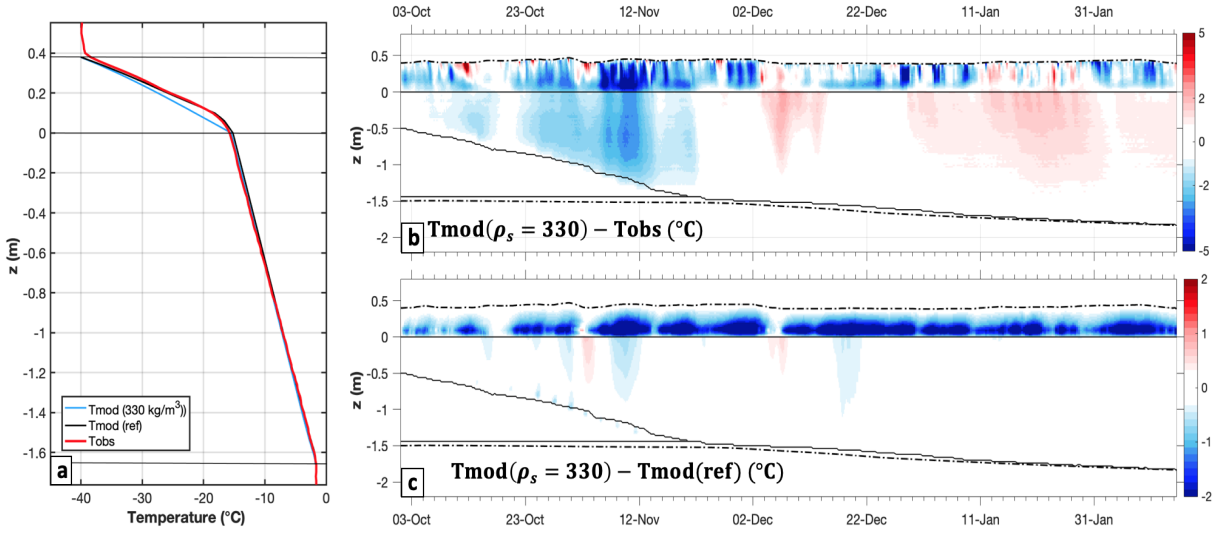

Figure 10. For S17: **(a)** Observed temperature profile (red), reference modeled temperature (black) and modeled temperature using a constant snow density (blue) on December 22 (°C). **(b)** Temperature differences between simulation using a constant snow density of 330 kg/m³ and observations (°C) **(c)** Temperature difference between the simulation using a constant snow density and the reference simulation (°C). Dotted lines correspond to the modeled interfaces and solid lines to the observed ones. Model outputs are interpolated to the vertical resolution of the data (2 cm).

	Snow layer	Conductivity W/m/K	Equivalent conductivity W/m/K
SIMBA 16	1 to 4	0.98	**0.43**
	5 to 10	0.31	
SIMBA 17	1 to 3	0.80	
	4 to 6	0.24	**0.32**
	7 to 10	0.27	
SIMBA 18	1	1.02	**0.44**
	2 to 10	0.41	
SIMBA 19	1 to 10	0.37	**0.37**
Sensitivity experiment	1 to 10	0.31	**0.31**

Table 3. Snow conductivity for each model layer (numbered from 1 to 10, see Figure 1), equivalent conductivity for the reference simulations of the four SIMBAs and conductivity for the sensitivity experiment.

4.2 Experiment with no lateral fluxes

Simulations are performed without adding the lateral heat flux density term in the heat diffusion equation (equation 4). Here, we present the results obtained using the S17 series, (they are similar for the 3 other series). In the absence of lateral heat flux, the model was no longer able to correctly reproduce the freezing of the seawater in the hole and the following sea ice growth (Figure 11). The observations showed that the 1.5 m deep hole was entirely frozen on November 21 and the final sea ice thickness reached 1.8 m on February 14. The simulation with no lateral heat flux led to a solid sea ice thickness of 0.75 m on November 21 and 1.10 m at the end of the simulation, on February 14 (Figure 11a).

The modelled sea ice temperature is up to 8 °C warmer than the observed one (Figure 11b). The temperature difference between the run with no lateral flux and the observations illustrates the contribution of the lateral flux to the sea ice cooling (Figure 11b).

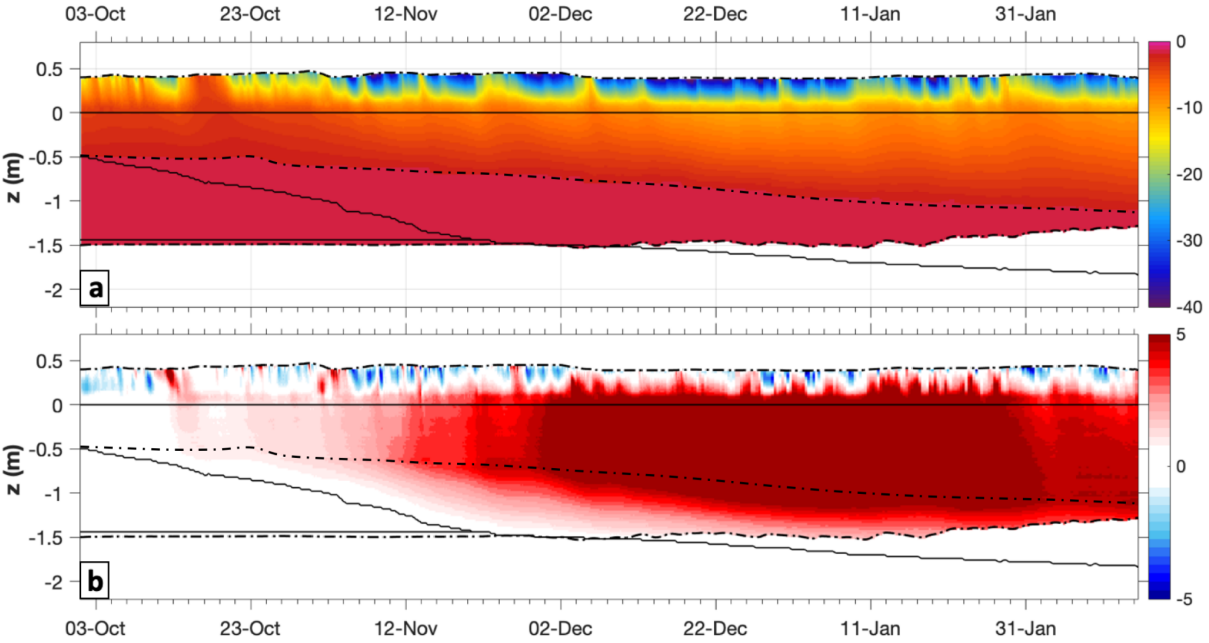

Figure 11. For S17: **(a)** Evolution of the simulated temperature obtained with no lateral heat flux (°C). **(b)** Temperature differences between simulation with no lateral flux and observations (°C). Dotted lines correspond to the modeled interfaces and solid lines to the observed ones.

5. Conclusion

In a companion paper, we analyzed temperature profiles through snow and sea ice coming from SIMBA instruments, which were deployed in September 2015 and drifted with the Arctic ice pack for several months. The densities of the different snow layers were estimated as well as the lateral heat flux densities required to refreeze the deployment holes. Here the state-of-the-art one-dimensional model LIM1D is used to simulate these observations, to check the validity of the analysis of Gani et al. [2021a], and to draw additional information not available from the observations. The model was modified to account for a layered snow cover (by introducing 10 snow layers), and, building on Petrich et al., [2007], a lateral heat flux term was also introduced into the heat diffusion equation.

The model provided correct simulations of temperature profiles when using the snow densities estimated by the observation analysis. The RMSD between simulations and observations ranged from 0.4 to 0.7 °C in sea ice and from 1.3 to 1.8 °C in snow. The simulations support the snow density estimates from observations. The larger differences

are located at the air/snow interface and may come from the atmospheric fluxes (see Gani et al. 2019). Sensitivity experiments showed that using a common constant value of snow density of 330 kg/m³ generally degrades the evolution of the simulated temperature profiles and sea ice thicknesses. However, if the total thermal conductivity of the snow cover is correctly estimated, the simulated evolution of the ice temperature and thickness is in agreement with the observed one.

The kinetics and duration (2 months) of the deployment hole refreezing in the model were in good agreement with the observations. Modeled values of lateral heat flux densities (up to $5\,W/m^2$) corroborated those obtained from the observations. Simulations performed without lateral flux (with only vertical heat fluxes active) led to a too slow refreezing rate in the deployment hole and an incorrect sea ice thickness evolution. It would be interesting to study the refreezing of the hole and compare the lateral heat flux estimates for a period when the sea ice is colder than in September.

Note that these observations were collected at the beginning of the winter when the density of the snow layers does not vary much. In spring, snow density tends to increase (Gallet et al., 2017). Such a transformation will have to be taken into account in one-dimensional models to accurately represent the evolution of the snow-ice system in the Arctic, and evaluate the impact of the changes in snow properties on the summer melting of sea-ice.

Acknowledgments:

We thank the crew and scientists who participated in the PS94 "TransArc II campaign. We acknowledge support from the ANR EQUIPEX IAOOS project, through ANR-10-EQPX-32-01 grant. We thank Clement Rousset and Martin Vancoppenolle for helping us with the model LIM1D and for the discussions. Research funded under PhD scholarships from Sorbonne Université, Paris.

Data availability

The SIMBA data and interfaces are available at :

https://data.ifremer.fr/Deposer-Archiver-des-donnees/SEANOE

Parameters from the ERA-Interim reanalysis were obtained from ECMWF.

REFERENCES

Barrere, M., Domine, F., Decharme, B., Morin, S., Vionnet, V., and Lafaysse, M.: Evaluating the performance of coupled snow–soil models in SURFEXv8 to simulate the permafrost thermal regime at a high Arctic site, Geosci. Model Dev., 10, 3461–3479, https://doi.org/10.5194/gmd-10-3461-2017, 2017.

Bartelt, P., & Lehning, M. (2002). A physical SNOWPACK model for the Swiss avalanche warning: Part I: Numerical model. Cold Regions Science and Technology, 35(3), 123–145. https://doi.org/10.1016/S0165-232X(02)00074-5

Bitz, C. M., & Lipscomb, W. H. (1999). An energy conserving thermodynamic model of sea ice. *Journal of Geophysical Research*, *104*, 15,669–15,677. https://doi.org/10.1029/1999JC900100

Blazey, B.A., Holland, M.M., Hunke, E.C., 2013. Arctic Ocean sea ice snow depth evaluation and bias sensitivity in CCSM. Cryosphere 7, 1887e1900. http://dx. doi.org/10.5194/tc-7-1887-2013.

Bokhorst, Stef & Pedersen, Stine & Brucker, Ludovic & Anisimov, O. & Bjerke, Jarle & Brown, Ross & Ehrich, Dorothee & Essery, Richard & Heilig, Achim & Ingvander, Susanne & Johansson, Cecilia & Johansson, Margareta & Jónsdóttir, Ingibjörg & Inga, Niila & Luojus, Kari & Macelloni, Giovanni & Mariash, Heather & McLennan, Donald & Rosqvist, Gunhild & Callaghan, Terry. (2016). Changing Arctic snow cover: A review of recent developments and assessment of future needs for observations, modelling, and impacts. Ambio. 45. 10.1007/s13280-016-0770-0.

Burke, E., Dankers, R., Jones, C., & Wiltshire, A. (2013). A retrospective analysis of pan Arctic permafrost using the JULES land surface model. Climate Dynamics, 41(3–4), 1025–1038. https://doi.org/10.1007/s00382-012-1648-x

Castro-Morales, K., Ricker, R., and Gerdes, R.: Snow on Arctic sea ice: model representation and last decade changes, The Cryosphere Discuss., 9, 5681–5718, https://doi.org/10.5194/tcd-9-5681-2015, 2015.

Castro-Morales, K., Ricker, R., & Gerdes, R. (2017). Regional distribution and variability of model-simulated Arctic snow on sea ice. *Polar Science*, 13, 33– 49.

Chadburn, S. E., Burke, E. J., Essery, R. L. H., Boike, J., Langer, M., Heikenfeld, M., et al. (2015). Impact of model developments on present and future simulations of permafrost in a global land-surface model. The Cryosphere Discussions, 9(2), 1965–2012. https://doi.org/10.5194/tcd-9-1965-2015

Chris Petrich, Pat. J. Langhorne, and Tim G. Haskell. (2007). Formation and structure of refrozen cracks in land-fast first-year sea ice. J. Geophys. Res: Oceans, 112, https://doi.org/10.1029/2006JC003466.

Decharme, B., Brun, E., Boone, A., Delire, C., Le Moigne, P., and Morin, S. (2016). Impacts of snow and organic soils parameterization on northern Eurasian soil temperature profiles simulated by the ISBA land surface model. The Cryosphere, 10(2), 853–877. https://doi.org/10.5194/tc-10-853-2016

Dee, D. P., Uppala, S. M., Simmons, A. J., Berrisford, P., Poli, P., Kobayashi, S., et al. (2011). The ERA-Interim reanalysis: Configuration and performance of the data assimilation system. *Quartely Journal of the Royal Meteorological Society*, *137*(656), 553–597. https://doi.org/10.1002/qj.828

Dutra, E., Viterbo, P., Miranda, P. M. A., & Balsamo, G. (2012). Complexity of snow schemes in a climate model and its impact on surface energy and hydrology. Journal of Hydrometeorology, 13(2), 521–538. https://doi.org/10.1175/JHM-D-11-072.1

Gallet, J.-C., I. Merkouriadi, G. E. Liston, C. Polashenski, S. Hudson, A. Rösel, and S. Gerland (2017), Spring snow conditions on Arctic sea ice north of Svalbard, during the Norwegian Young Sea ICE (N-ICE2015) expedition, J. Geophys. Res. Atmos., 122, 10,820–10,836, doi:10.1002/2016JD026035

Golden, K. M., Ackley, S. F., and Lytle, V. I. (1998). The percolation phase transition in sea ice. *Science*, *282*, 2238–2241. https://doi.org/ 10.1126/science.282.5397.2238

Gani, S., Sirven, J., Sennéchael, N., and Provost, C. (2019). Revisiting winter arctic ice mass balance observations with a 1-D model: Sensitivity studies, snow density estimation, flooding, and snow ice formation.. *Journal of Geophysical Research: Oceans*, *124*, 9295–9316. https://doi.org/10.1029/ 2019JC015431

Hunke, E. C., Lipscomb, H., and Turner, A. K.: Sea-ice models for climate study: retrospective and new directions, J. Glaciol., 56, 1162–1172, doi:10.3189/002214311796406095, 2010.

Jackson, K., Wilkinson, J., Maksym, T., Meldrum,D., Beckers, J., Haas, C., and McKenzie, D. (2013). A novel and low-cost sea-ice mass balance buoy,*Journal of Atmospheric and OceanicTechnology*, *30*, 2676–2688. https://doi.org/10.1175/JTECH-D-13-00058.1

Lawrence, D. M., & Slater, A. G. (2010). The contribution of snow condition trends to future ground climate. Climate Dynamics, 34(7–8), 969–981. https://doi.org/10.1007/s00382-009-0537-4

Lecomte, O., T. Fichefet, M. Vancoppenolle, and M. Nicolaus (2011), A new snow thermodynamic scheme for large-scale sea-ice models, Ann. Glaciol.,52(57), 337–346.

Lecomte, O., T. Fichefet, M. Vancoppenolle, F. Domine, F. Massonnet, P. Mathiot, S. Morin, and P.Y. Barriat (2013), On the formulation of snow thermal conductivity in large-scale sea ice models, J. Adv. Model. Earth Syst., 5, 542–557, doi:10.1002/jame.20039.

Massonnet, F., T. Fichefet, H. Goosse, M. Vancoppenolle, P. Mathiot, and C. König Beatty (2011), On the influence of model physics on simulations of Arctic and Antarctic sea ice, Cryosphere, 5(3), 687–699, doi:10.5194/tc-5-687-2011.

Merkouriadi, I., J.-C. Gallet, R. M. Graham, G. E. Liston, C. Polashenski, A. Rösel, and S. Gerland (2017), Winter snow conditions on Arctic sea ice north of Svalbard during the Norwegian young sea ICE (N-ICE2015) expedition, J. Geophys. Res. Atmos., 122, 10,837–10,854, doi:10.1002/ 2017JD026753.

Paquin, J. P., & Sushama, L. (2015). On the Arctic near-surface permafrost and climate sensitivities to soil and snow model formulations in climate models. Climate Dynamics, 44(1–2), 203–228. https://doi.org/10.1007/s00382-014-2185-6

Pedersen, C.A., Winther, J.-G., 2005. Intercomparison and validation of snow albedo parameterization schemes in climate models. Clim. Dynam 25, 351e362. http://dx.doi.org/10.1007/s00382-005-0037-0.

Sturm, M., Holmgren, J., Perovich, D.K., 2002a. Winter snow cover on the sea ice of the Arctic Ocean at the surface heat budget of the Arctic Ocean (SHEBA): temporal evolution and spatial variability. J. Geophys. Res. 107, 8047. http://dx. doi.org/10.1029/2000JC0000400.

Semmler, Tido & Cheng, Bin & Yang, Yu & Rontu, Laura. (2012). Snow and ice on Bear Lake (Alaska) – sensitivity experiments with two lake ice models.. Tellus. 10.3402/tellusa.v64i0.17339..

Skyllingstad, E. D., & Polashenski, C. (2018). Estimated heat budget during summer melt of Arctic first-year sea ice. *Geophysical Research Letters*, 45(21), 11789– 11797. https://cdiac/10.1029/2018GL080349

Vancoppenolle, M., and L. Tedesco (2017), An Introduction to Sea Ice, chap.20 Numerical Models of Sea Ice Biogeochemistry, pp 492-515, Wiley.

Vancoppenolle, M., Fichefet, T., & Goosse, H. (2008). Simulating the mass balance and salinity of Arctic and Antarctic sea ice. 2: Importance of sea ice salinity variations. *Ocean Modelling*, *27*(1-2), 54–69. https://doi.org/10.1016/j.ocemod.2008.11.003

Vancoppenolle, M., H. Goosse, A. de Montety, T. Fichefet, B. Tremblay, and J.-L. Tison (2010), Modeling brine and nutrient dynamics in Antarctic sea ice: The case of dissolved silica, J. Geophys. Res., 115, C02005, doi:10.1029/2009JC005369.

Vionnet, V., Brun, E., Morin, S., Boone, A., Faroux, S., Le Moigne, P., et al. (2012). The detailed snowpack scheme Crocus and its imple- mentation in SURFEX v7.2. Geoscientific Model Development, 5(3), 773–791. https://doi.org/10.5194/gmd-5-773-2012.

Conclusion

Sommaire

6.1 Résumé des résultats

Depuis 2012, des bouées IAOOS ont été déployées dans l'Arctique et ont dérivé avec la glace de mer à différentes périodes de l'année. La mise en place d'un système SIMBA sur ces plateformes dérivantes rend possible l'étude des processus physiques actifs dans la glace de mer et la neige ainsi qu'aux interfaces avec l'atmosphère et l'océan. En traversant l'air, la neige, la glace et l'océan, les chaînes de thermistances de ces SIMBAs fournissent des profils de température et un proxy de conductivité thermique avec une haute résolution verticale et temporelle. Des jeux de données collectés par ces instruments constituent la principale source d'observations pour le travail présenté dans les chapitres précédents.

L'obtention de données de terrain fiables sur la glace de mer et la neige est indispensable mais aussi très coûteuse, énergivore, et beaucoup de régions de l'Arctique sont difficiles d'accès. C'est pourquoi aucune donnée ne doit être négligée et il est crucial de les étudier au maximum pour en déduire toutes les informations utiles à une meilleure compréhension des processus physiques ayant lieu en Arctique. C'était là l'objectif de ce travail de thèse où six séries de données ont été étudiées. Pour y parvenir, nous avons associé ces données à des simulations réalisées à partir d'un modèle unidimensionnel de glace et de neige (LIM1D). Des informations importantes sur la nature des milieux étudiés (neige et glace) et sur les processus physiques régissant leur évolution ont pu être étudiées.

Deux modifications ont été apportées au modèle afin de simuler avec précision les processus. Plusieurs couches de neige ont été introduites afin de rendre compte de l'hétérogénéité verticale des paramètres tels que la conductivité et une paramétrisation des flux latéraux de chaleur dans la glace à également été ajoutée.

Avec ces modifications, les évolutions des profils de température simulés sont en bon accord avec les observations : la RMSD entre la température simulée et observée dans la glace va de 0.2 à 0.7 °C selon les séries. L'épaisseur simulée de la glace de mer pendant les périodes de croissance et de fonte est également proche de celle observée, et ce pour les 6 séries (les différences sont en moyenne de 2 cm et n'excèdent pas 5 cm). Des expériences de sensibilité aux flux atmosphérique, océanique et au profil initial de salinité ont également été réalisées afin de connaître leur impact sur les simulations.

Deux séries de données ont été recueillies au cours de l'expédition norvégienne Young Sea ICE (N-ICE2015), qui a fourni une plateforme d'observation de l'atmosphère, de la neige, de la glace de mer et de l'océan de Janvier à fin Juin 2015, au nord du Svalbard. Ces observations hivernales ont montré l'existence de chutes de neige abondantes et une forte fonte basale de la glace de mer. Elles ont également permis de documenter pour la première fois la formation de glace de neige dans la banquise arctique (un processus fréquent en Antarctique mais jugé rare en Arctique jusqu'à présent). Ce processus de formation de glace de neige a été simulé avec succès en imposant le taux d'immersion de la neige (valeur du franc bord). L'évolution du profil de salinité et de la fraction de poches de saumure dans la glace à pu être étudiée lorsque la neige est inondée puis lorsque la glace de neige se forme.

Les quatre autres séries proviennent de SIMBAs déployées lors de l'expédition PS94 "TransArc II" (Trans-Arctic survey of the Arctic Ocean in transition) en Septembre 2015. Ces SIMBAs ont dérivé avec la banquise pendant 3 à 9 mois. Les trous percés dans la glace pour déployer les chaînes SIMBA ont mis environ deux mois pour se reboucher entièrement

(alors que quelques jours suffisent pour des bouées déployées au cœur de l'hiver). On a observé des épaisseurs de neige allant de 0 à 60 cm avec une forte hétérogénéité verticale du manteau neigeux. La croissance basale de la glace était de l'ordre de 0.8 cm/jour.

Nous présentons une nouvelle méthode d'estimation de la conductivité de la neige à partir de ces séries d'observations. En étudiant les profils de température (calcul des gradients verticaux) et les profils de température mesurée à la fin d'un cycle de chauffe (le représentant de la conductivité thermique), nous avons déterminé la conductivité des différentes couches qui constituaient le manteau neigeux. Nous proposons une relation qui lie les valeurs mesurées de température mesurée à la fin d'un cycle de chauffe à la conductivité de la neige, qui est un paramètre essentiel du bilan thermique. Ces estimations ont été confirmées par des simulations numériques et des expériences de sensibilité.

L'existence du trou de déploiement des SIMBAs et sa congélation ont permis d'estimer le flux latéral de chaleur dans la glace de mer au voisinage de ce trou. Ce flux latéral s'est avéré être une composante essentielle à la congélation de l'eau de mer. Les simulations numériques ont correctement représenté la cinétique de congélation du trou et ont ainsi confirmé les estimations faites à partir des observations (densité de flux allant jusqu'à 5 W/m^2).

6.2 Perspectives

Des données récoltées par plusieurs SIMBAs ont été étudiées de façon approfondie et la synergie entre observations et simulations numériques réalisées avec le modèle LIM1D s'est avérée fructueuse. En développant de nouvelles paramétrisations, nous avons pu représenter les observations avec fidélité et modéliser l'évolution de grandeurs inaccessibles en observation continue. Mais de nombreuses autres recherches peuvent encore être conduites.

Les observations analysées et modélisées étaient principalement hivernales, lorsque le flux solaire radiatif incident était nul. Aussi, l'albédo de la neige et de la glace n'a pas été étudié. Plusieurs SIMBAs ont été déployés au printemps et en été (Avril à Octobre), dans des zones différentes de l'Arctique. Il serait intéressant d'étudier ces données et en premier lieu de réaliser des expériences numériques de sensibilité à la valeur de l'albédo. En effet, l'albédo est à l'origine de processus qui contrôlent le bilan énergétique de la glace de mer, et il dépend lui-même des propriétés de la neige (*Verin et al., 2019*) telles que la densité ou la taille des grains (*Warren, 1982; Bohren and Barkstrom, 1974; Aoki et al., 2003*).

Provost et al., [2019] ont décrit des événements caractéristiques de l'été en Arctique en analysant les profils de température mesurés par deux SIMBAs (Figure 1) : fonte de la neige en surface, lac de fontes (*melt pond*), infiltration de l'eau de fonte dans la glace et formation de glace superposée (*superimposed ice*) sous la neige fondue. Développer des paramétrisations pour représenter ces phénomènes dans le modèle LIM1D permettrait de mieux analyser les processus physiques ayant lieu au sein de la neige et de la glace de mer. Si elles s'avèrent pertinentes, une utilisation dans des modèles 3D pourrait même être envisagée.

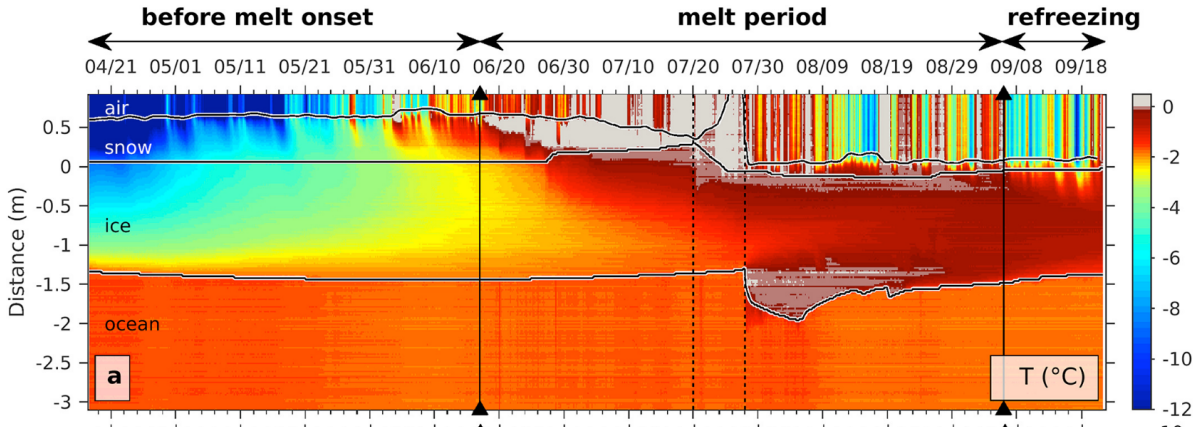

Figure 1. Données SIMBA de Température (°C). Les isolignes noires et blanches correspondent aux interfaces principales suivantes, de haut en bas : limite inférieure de l'atmosphère, limite supérieure de la glace de mer et limite supérieure de l'océan. Les lignes verticales marquent le début de la fonte des neiges (17 juin) et le début du regel (6 septembre). Les lignes verticales en pointillés marquent la période du bassin de fonte (20-27 juillet). De *Provost et al., 2019.*

Au printemps, la conductivité et la densité de la neige ont tendance à augmenter (*Gallet et al., 2017*). Cette transformation devra être prise en compte dans les modèles unidimensionnels pour représenter précisément l'évolution du système neige-glace en Arctique, et évaluer l'impact des changements des propriétés de la neige sur la fonte estivale de la banquise.

Nous avons vu que les propriétés de la neige jouent un rôle important dans le transfert de chaleur à travers la glace. En particulier la conductivité thermique de la neige, qui impacte le taux de formation de la glace de mer (Eicken et al., 1995 ; Fichefet et Morales Maqueda, 1997 ; Sturm et al., 2002; Lecomte et al., 2013). La relation que l'on propose entre les valeurs de température mesurées à la fin d'un cycle de chauffe et la conductivité de la neige mériterait d'être améliorée. Des études en laboratoire (déjà esquissées) sur le mode "chauffe" et la conductivité permettront très certainement de préciser cette relation.

Dans ces travaux nous nous sommes concentré sur la partie physique de la glace de mer et avons totalement mis de côté la partie biologique, bien qu'elle soit développée dans le modèle LIM1D (*Vancoppenolle et al.*, 2010). Les écosystèmes dans la glace de mer sont caractérisés par des microalgues vivant dans des inclusions de saumure. Le modèle LIM1D comprend une composante biologique idéalisée de la glace de mer et caractérisée par un nutriment (silice dissoute). L'étude de l'évolution des nutriments dans de la glace de mer lors de processus physiques documentés par les SIMBA pourrait également être une perspective intéressante.

Enfin, une étude plus approfondie du flux latéral mériterait d'être poursuivie. Les premières estimations au sein de la glace de mer pourraient être comparées à d'autres séries, ou la prise en glace se faisait plus ou moins rapidement selon la température de la glace, de l'air ou bien la taille de la tarière. Un parallèle pourrait être effectué entre le rebouchage des trous des SIMBAs et la prise en glace de l'eau de mer dans les leads (Figure 2). En effet, le temps de congélation de la glace de mer dans les leads a un impact

significatif sur le bilan de masse de la banquise Arctique (*Wilchinsky et al.* 2015). L'étude de la cinétique de formation de la glace de mer dans les leads à partir d'un modèle unidimensionnel a démontré l'intérêt d'introduire une composante horizontale rendant compte de la formation latérale de la glace (Heorton et al., 2017). Une piste de réflexion intéressante serait d'adapter le calcul du flux latéral à la géométrie des leads (*Petrich et al., 2007*).

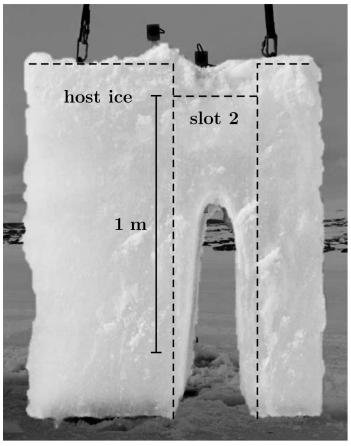

Figure 2. Bloc vertical d'un lead artificiel. Les lignes pointillées indiquent le contour original de la fente et l'interface glace/air. L'interface glace/eau est en forme d'arc. De *Petrich et al., 2007.*

Références

Albert, Mary & Courville, Zoe & Perron, F. & Dibb, J. & Lefer, Barry. (2004). Where Does Firn Air Come From?. AGU Fall Meeting Abstracts.

Aoki, T., A. Hachikubo, and M. Hori, Effects of snow physical parameters on shortwave broadband albedos, J. Geophys. Res., 108(D19), 4616, doi:10.1029/2003JD003506, 2003.

Bitz, C. M., & Lipscomb, W. H. (1999). An energy conserving thermodynamic model of sea ice. *Journal of Geophysical Research*, *104*, 15,669–15,677. https://doi.org/10.1029/1999JC9001

Boé, J., Hall, A., and Qu, X. (2009). September sea-ice cover in the Arctic Ocean projected to vanish by 2100. *Nature Geoscience*, 2(5) :341–343.

Bokhorst, Stef & Pedersen, Stine & Brucker, Ludovic & Anisimov, O. & Bjerke, Jarle & Brown, Ross & Ehrich, Dorothee & Essery, Richard & Heilig, Achim & Ingvander, Susanne & Johansson, Cecilia & Johansson, Margareta & Jónsdóttir, Ingibjörg & Inga, Niila & Luojus, Kari & Macelloni, Giovanni & Mariash, Heather & McLennan, Donald & Rosqvist, Gunhild & Callaghan, Terry. (2016). Changing Arctic snow cover: A review of recent developments and assessment of future needs for observations, modelling, and impacts. Ambio. 45. 10.1007/s13280-016-0770-0.

Bohren, C. F. and Barkstrom, B. R.: Theory of the optical properties of snow, Journal of Geophysical Research, 79, 4527–4535, https://doi.org/10.1029/JC079i030p04527, 1974.

Brandt, R.E., and S.G. Warren: Solar heating rates and temperature profiles in Antarctic snow and ice. *Journal of Glaciology*, Vol. 39, pp. 99-110, 1993.

Colbeck, S. C. The layered character of snow covers. Rev. Geophys. 291, 81–96 (1991).

Colbeck, S.C, An overview of seasonal snow metamorphism, Rev. Geophys., 20 (1) (1982), pp. 45-61.

Colbeck, S. (1973). The Theory of Metamorphism of Wet Snow. *US Army Corps Eng Cold Reg Res Eng Lab Res Rep*, page 19.

Colbeck, S. C. (1983). Theory of metamorphism of dry snow. *Journal of Geophysical Research*, 88(C9) :5475–5482.

Comiso, J. C. (2012). Large Decadal Decline of the Arctic Multiyear Ice Cover. *Journal of climate*, 25(4) :1176–1193.

Conger, S. M. and McClung, D. M. (2009). Comparison of density cutters for snow profile obser- vations. *Journal of Glaciology*, 55(189) :163–169.

Coon M., G. A. Maykut, R. S. Pritchard, D. A. Rothrock and A. S. Thorndike (1974), Modeling the pack ice as an elastic-plastic material, *AIDJEX Bull., 24*:1–105.

Coon, M. et al. (2007), Arctic Ice Dynamics Joint Experiment (AIDJEX) assumptions revised and found inadequate, *J. Geophys. Res.*, *112*, C11S90, doi:10.1029/2005JC003393.

Cox, G. F. N., and W. F. Weeks (1988), Numerical simulation of the profile properties of undeformed first-year sea ice during the growth season, *J. Geophys. Res.*, 93(C10), 12,449–12,460.

Cox, G.F.N.; Weeks, W.F. Equations for determining the gas and brine volumes in sea-ice samples. J. Glaciol. 1983, 29, 306–316.

Domine, F., Albert, M., Huthwelker, T., Jacobi, H., Kokhanovsky, A. A., Lehning, M., Picard, G., and Simpson, W. R. (2008). Snow physics as relevant to snow photochemistry. *Atmospheric Chemistry and Physics*, 8 :171–208.

Domine, Florent; Gallet, Jean-Charles; Barret, Manuel; Houdier, Stéphan; Voisin, Didier; Douglas, Thomas A; Blum, Joel D; Beine, Harry J; Anastasio, Cort; Bréon, François-Marie (2011): (Table 1) Characteristics of diamond dust events near Barrow Arctic Research Center. PANGAEA, https://doi.org/10.1594/PANGAEA.809171, In supplement to: Domine, F et al. (2011): The specific surface area and chemical composition of diamond dust near Barrow, Alaska. Journal of Geophysical Research: Atmospheres, 116, D00R06, https://doi.org/10.1029/2011JD016162

Domine, F., Gallet, J. C., Bock, J., and Morin, S. (2012). Structure, specific surface area and thermal conductivity of the snowpack around Barrow, Alaska. *Journal of Geophysical Research Atmospheres*, 117(D14).

Domine, F., Barrere, M., and Sarrazin, D. (2016). Seasonal evolution of the effective thermal conductivity of the snow and the soil in high Arctic herb tundra at Bylot Island, Canada. *The Cryosphere*, 10(6) :2573–2588.

Eicken, H., H. Fischer, and P. Lemke (1995), Effects of the snow cover on Antarctic sea ice and potential modulation of its response to climate change, Ann. Glaciol., 21, 369–376

Feys et Lietaer, Méthodes d'éléments finis pour la dynamique de la glace de mer, UCLouvain, 2005.

Fichefet, T., and M. Morales Maqueda (1997), Sensitivity of a global sea ice model to the treatment of ice thermodynamics and dynamics, J. Geophys. Res., 102(C6), 12,609–12,646

Gallée, H., Guyomarc'h, G., and Brun, E.: Impact of snow drift on the Antarctic ice sheet surface mass balance: possible sensitiv- ity to snow-surface properties, Bound.-Lay. Meteorol., 99, 1–19, 2001.

Gallet, J.-C., I. Merkouriadi, G. E. Liston, C. Polashenski, S. Hudson, A. Rösel, and S. Gerland (2017), Spring snow conditions on Arctic sea ice north of Svalbard, during the Norwegian Young Sea ICE (N-ICE2015) expedition, J. Geophys. Res. Atmos., 122, 10,820–10,836, doi:10.1002/2016JD026035

Hall, A. (2004). The Role of Surface Albedo Feedback in Climate. *Journal of climate*, 17 :1550–1568.

Hibler, W. D. and E. Schulson (2000), On modelling the anisotropic failure and flow of flawed sea ice, *J. Geophys. Res.*, *105*, 17,105-17,120.

Hunke, E. C. and J. K. Dukowicz (1997), An elastic-viscous-plastic model for sea ice dynamics, *J. Phys. Oceanogr.*, *27*(9), 1849-1867.

IPCC, 2021: *Climate Change 2021: The Physical Science Basis. Contribution of Working Group I to the Sixth Assessment Report of the Intergovernmental Panel on Climate Change* [Masson-Delmotte, V., P. Zhai, A. Pirani, S.L. Connors, C. Péan, S. Berger, N. Caud, Y. Chen, L. Goldfarb, M.I. Gomis, M. Huang, K. Leitzell, E. Lonnoy, J.B.R. Matthews, T.K. Maycock, T. Waterfield, O. Yelekçi, R. Yu, and B. Zhou (eds.)]. Cambridge University Press. In Press.

Jackson, K., Wilkinson, J., Maksym, T., Meldrum,D., Beckers, J., Haas, C., and McKenzie, D. (2013). A novel and low-cost sea-ice mass balance buoy,*Journal of Atmospheric and OceanicTechnology*, *30*, 2676–2688. https://doi.org/10.1175/JTECH-D-13-00058.1

Kevin Guerreiro. Amélioration des estimations d'épaisseur de glace de mer arctique par altimétrie spatiale. Océan, Atmosphère. Université Paul Sabatier - Toulouse III, 2017. Français. NNT: 2017TOU30277 . tel-02924618.

Kinnard, C., Zdanowicz, C. M., Fisher, D. A., Isaksson, E., Vernal, A. de, & Thompson, L. G. (2011). Reconstructed changes in Arctic sea ice over the past 1,450 years. Nature, 479(7374), 509–512. https://doi.org/10.1038/nature10581.

Kwok, R. and Rothrock, D. A. (2009). Decline in Arctic sea ice thickness from submarine and ICESat records : 1958 – 2008. *Geophysical Research Letters*, 36(May) : 1–5.

Lebrun Marion. De l'interaction entre banquise, lumière et phytoplancton arctique. Océanographie. Sorbonne Université, 2019. Français. NNT : 2019SORUS524 . tel-02918818v2

Lecomte, O., T. Fichefet, M. Vancoppenolle, and M. Nicolaus (2011), A new snow thermodynamic scheme for large-scale sea-ice models, Ann. Glaciol.,52(57), 337–346.

Lecomte, O., T. Fichefet, M. Vancoppenolle, F. Domine, F. Massonnet, P. Mathiot, S. Morin, and P.Y. Barriat (2013), On the formulation of snow thermal conductivity in large-scale sea ice models, J. Adv. Model. Earth Syst., 5, 542–557, doi:10.1002/jame.20039.

Lecomte, O., Fichefet, T., Massonnet, F., & Vancoppenolle, M. (2015). Benefits from representing snow properties and related processes in coupled ocean–sea ice models. Ocean Modelling, 87, 81–85. https://doi.org/10.1016/j.ocemod.2014.11.005.

Leppäranta, M., A review of analytical models of sea-ice growth, *Atmos. Ocean*, 31, 123–138, 1993.

Leu, Eva & Wiktor, Jozef & Søreide, Janne & Berge, Jørgen & Falk-Petersen, Stig. (2010). Increased irradiance reduces food quality of sea ice algae. Marine Ecology Progress Series. 411. 1-12. 10.3354/meps08647.

The physics of snow crystals Kenneth G Libbrecht 2005 Rep. Prog. Phys. 68 855-895 doi: 10.1088/0034-4885/68/4/R03

Liston, G. E., Haehnel, R. B., Sturm, M., Hiemstra, C. A., Berezovskaya, S., & Tabler, R. D. (2007). Simulating complex snow distributions in windy environments using SnowTran-3D. *Journal of Glaciology*, 53, 241– 256.

Maslanik, J., Stroeve, J., Fowler, C., and Emery, W. (2011). Distribution and trends in Arctic sea ice age through spring 2011. *Geophysical Research Letters*, 38(July) :2–7.

Massonnet, F., Vancoppenolle, M., Goosse, H., Docquier, D., Fichefet, T., and Wrigglesworth, E. B. (2018). Arctic sea-ice change tied to its mean state through thermodynamic processes. *Nature Climate Change*, 8 :599–605.

Maykut, G. A., and N. Untersteiner (1971), Some results from a time-dependent thermodynamic model of sea ice, *J. Geophys. Res.*, *76*(6), 1550–1575.

Maykut, G.A. 1986 The surface heat and mass balance. In Untersteiner, N., ed. *The geophysics of sea ice*. New York, Plenum Press, 395–463. (NATO ASI Ser., Ser. B, Physics, 146.)

Meredith, M., M. Sommerkorn, S. Cassotta, C. Derksen, A. Ekaykin, A. Hollowed, G. Kofinas, A. Mackintosh, J. Melbourne-Thomas, M.M.C. Muelbert, G. Ottersen, H. Pritchard, and E.A.G. Schuur, 2019: Polar Regions. In: *IPCC Special Report on the Ocean and Cryosphere in a Changing Climate* [H.-O. Pörtner, D.C. Roberts, V. Masson-Delmotte, P. Zhai, M. Tignor, E. Poloczanska, K. Mintenbeck, A. Alegría, M. Nicolai, A. Okem, J. Petzold, B. Rama, N.M. Weyer (eds.)]. In press.

Merkouriadi, I., J.-C. Gallet, R. M. Graham, G. E. Liston, C. Polashenski, A. Rösel, and S. Gerland (2017), Winter snow conditions on Arctic sea ice north of Svalbard during the Norwegian young sea ICE (N-ICE2015) expedition, J. Geophys. Res. Atmos., 122, 10,837–10,854, doi:10.1002/ 2017JD026753.

Mundy, C. J., Barber, D. G., and Michel, C. (2005). Variability of snow and ice thermal , physical and optical properties pertinent to sea ice algae biomass during spring. *Journal of Marine Systems*, 58 :107–120.

Msadek, Rym & Garric, Gilles & Fleury, Sara & Garnier, Florent & Batté, Lauriane & Bushuk, Mitch. (2020). Prévoir les variations saisonnières de la glace de mer arctique et leurs impacts sur le climat. La Météorologie. 024. 10.37053/lameteorologie-2020-0089.

Nakawo, M. and Sinha, N. (1977). Growth Rate and Salinity Profile of First-Year Sea Ice in the High Arctic. *Journal of Glaciology*, 27(96) :1981.

Nicolaus, M., Hoppmann, M., Arndt, S., Hendricks, S., Katlein, C., Nicolaus, A., Rossmann, L., Schiller, M., and Schwegmann, S.: Snow Depth and Air Temperature Seasonality on Sea Ice Derived From Snow Buoy Measurements, Front. Mar. Sci., 8, 377, https://doi.org/10.3389/fmars.2021.655446, 2021.

Notz D and Stroeve J 2016 Arctic sea ice loss directly follows cumulative anthropogenic CO2 emissions *Science* 354

Notz, D., and M. G. Worster (2008), In situ measurements of the evolution of young sea ice, *J. Geophys. Res.*, 113, C03001, doi:10.1029/2007JC004333.

Notz, D. and Worster, M. G. (2009). Desalination processes of sea ice revisited. *Journal of Geo- physical Research*, 114 :1–10.

Oertling, A. B., and R. G. Watts (2004), Growth of and brine drainage from NaClH2O freezing: A simulation of young sea ice, J. Geophys. Res., 109, C04013, doi:10.1029/2001JC001109.

Pahaut. (1976). La métamorphose des cristaux de neige (Snow crystal metamorphosis).

Parkinson, Claire & Washington, Warren. (1979). A large-scale numerical model of sea ice. Journal of Geophysical Research. 84. 10.1029/JC084iC01p00311.

Perovich, D. K., Cota, G. F., Maykut, G. A., and Grenfell, T. C. (1993). Bio-optical observations of first-year Arctic sea ce. *Geophysical Research Letters*, 20(11) :1059–1062.

Perovich, D. K., Grenfell, T. C., Light, B., and Hobbs, P. V. (2002). Seasonal evolution of the albedo of multiyear Arctic sea ice. *Journal of Geophysical Research*, 107(C10) :8044.

Perovich, D. K., Grenfell, T. C., Richter-menge, J. A., Light, B., Iii, W. B. T., Eicken, H., and Eicken, H. (2003). Thin and thinner : Sea ice mass balance measurements during SHEBA. *Journal of climate*, 108 :1–21.

Petrich, C., P. J. Langhorne, and Z. F. Sun, 2006, Modelling the interrelationships between permeability, effective porosity and total porosity in sea ice, Cold Regions Science and Technology, 44(2), 131–144. doi:10.1016/j.coldregions.2005.10.001.

Petrich, C., Nicolaus, M., and Gradinger, R. (2012). Cold Regions Science and Technology Sensi- tivity of the light field under sea ice to spatially inhomogeneous optical properties and incident light assessed with three-dimensional Monte Carlo radiative transfer simulations. *Cold Regions Science and Technology*, 73 :1–11.

Pithan, F. and Mauritsen, T. (2014). Arctic amplification dominated by temperature feedbacks in contemporary climate models. *Nature Geoscience*, 7.

Polashenski, Chris & Golden, Kenneth & Perovich, Donald & Skyllingstad, Eric & Arnsten, Alexandra & Stwertka, Carolyn & Wright, Nicholas. (2017). Percolation blockage: A process that enables melt pond formation on first year Arctic Sea ice. Journal of Geophysical Research: Oceans. 122. 10.1002/2016JC011994.

Provost, C., Sennéchael, N., Miguet, J., Itkin, P., Rösel, A., Koenig, Z., Villacieros-Robineau, N., and Granskog, M. A. (2017). Observations of flooding and snow ice formation in a thinner Arctic sea ice regime during the N-ICE2015 campaign: Influence of basal ice melt and storms. Journal of Geophysical Research: Oceans, 122, 7115– 7134. https://doi.org/10.1002/2016JC012011.

Pierre Rampal. Etude de la dérive et de la déformation de la banquise Arctique par l'analyse de tra- jectoires Lagrangiennes. Océan, Atmosphère. Université Joseph-Fourier - Grenoble I, 2008. Français. tel-00352799

Richter-Menge. J, J. E. Overland, J. T. Mathis, and E. Osborne, Eds., 2017: Arctic Report Card 2017, http://www.arctic.noaa.gov/Report-Card.

Riche F, Schneebeli M (2013) Thermal conductivity of snow measured by three independent methods and anisotropy considerations. Cryosphere 7:217–227.

Schreyer, H. L., D. L. Sulsky, L. B. Munday, M. D. Coon, and R. Kwok (2006), Elastic-decohesive constitutive model for sea ice, *J. Geophys. Res.*, doi:10.1029/2005JC003334.

Semtner, A. J.: 1976, 'A Model for the Thermodynamic Growth of Sea Ice in Numerical Investigations of Climate', *J. Phys. Oceanogr.* 6, 379–389.

Skyllingstad, E. D., C. A. Paulson, and D. K. Perovich (2009), Simulation of melt pond evolution on level ice, J. Geophys. Res., 114, C12019, doi:10.1029/2009JC005363.

Stroeve, J. C., Kattsov, V., Barrett, A., Serreze, M., Pavlova, T., Holland, M., and Meier, W. N. (2012). Trends in Arctic sea ice extent from CMIP5 , CMIP3 and observations. *Geophysical Research Letters*, 39 :1–7.

Sturm, Matthew et Carl S Benson (1997). « Vapor transport, grain growth and depth-hoar development in the subarctic snow ». In : *Journal of Glaciology* 43.143, p. 42–59.

Sturm, M., D. K. Perovich, and J. Holmgren (2002a), Thermal conduc- tivity and heat transfer through the snow on the ice of the Beaufort Sea, J. Geophys. Res., 107(C21), 8043, doi:10.1029/2000JC000409.

Sturm, M., Holmgren, J., and Perovich, D. K. (2002). Winter snow cover on the sea ice of the Arctic Ocean at the Surface Heat Budget of the Arctic Ocean (SHEBA) : Temporal evolution and spatial variability. *Journal of Geophysical Research*, 107(C10) :8047.

Tschudi, M., W. N. Meier, J. S. Stewart, C. Fowler, and J. Maslanik, 2019a: EASE-Grid Sea Ice Age, Version 4. Boulder, Colorado USA. NASA National Snow and Ice Data Center Distributed Active Archive Center. https://doi.org/10.5067/UTAV7490FEPB.

Tschudi, M., W. N. Meier, and J. S. Stewart, 2019b: Quicklook Arctic Weekly EASE-Grid Sea Ice Age, Version 1. Boulder, Colorado USA. NASA National Snow and Ice Data Center Distributed Active Archive Center. https://doi.org/10.5067/2XXGZY3DUGNQ.

Vancoppenolle, M., H. Goosse, A. de Montety, T. Fichefet, B. Tremblay, and J.-L. Tison (2010), Modeling brine and nutrient dynamics in Antarctic sea ice: The case of dissolved silica, J. Geophys. Res., 115, C02005, doi:10.1029/2009JC005369.

Vancoppenolle, M., & Tedesco, L. (2017). Numerical models of sea ice biogeochemistry. In D. N. Thomas (Ed.), *Sea Ice* (pp. 492–515). John Wiley & Sons, Ltd. https://doi.org/10.1002/9781118778371.ch20.

Verin, Gauthier & Domine, Florent & Babin, Marcel & Picard, Ghislain & Arnaud, L.. (2019). Metamorphism of Arctic marine snow during the melt season. Impact on albedo. The Cryosphere Discussions. 1-29. 10.5194/tc-2019-113.

Vihma, T., Pirazzini, R., Fer, I., Renfrew, I. A., Sedlar, J., Tjernström, M., et al. (2014). Advances in understanding and parameterization of small-scale physical processes in the marine Arctic climate system: A review. *Atmospheric Chemistry and Physics*, *14*, 9403–9450. https://doi.org/10.5194/acp-14-9403-2014.

Warren, S. G. (1982). Optical Properties of Snow. *Reviews of Geophysics and Space Physics*,20(1) :67–89.

Wassmann, P., & Reigstad, M. (2011). Future Arctic Ocean Seasonal Ice Zones and Implications for Pelagic-Benthic Coupling. *Oceanography*, *24*(3), 220–231. https://doi.org/10.5670/oceanog.2011.74

Yen, Y. (1981), Review of thermal properties of snow, ice and sea ice, Rep. 81-10, U. S. Army Cold Reg. Res. and Eng. Lab. (CRREL), Hanover, N. H.

Zygmuntowska, M., Rampal, P., Ivanova, N., & Smedsrud, L. H. (2014). Uncertainties in Arctic sea ice thickness and volume: New estimates and implications for trends. The Cryosphere, 8(2), 705–720. https://doi.org/10.5194/tc-8-705-2014